Characterisation and control of electron-lattice coupling in $4d$ and $5d$ quantum materials

Cameron Darling Dashwood

A thesis submitted in partial fulfilment

of the requirements for the degree of

Doctor of Philosophy

of

University College London

Department of Physics and Astronomy

UCL

June 6, 2022

I, Cameron Darling Dashwood, confirm that the work presented in this thesis is my own. Where information has been derived from other sources, I confirm that this has been indicated in the thesis.

Abstract

The burgeoning field of quantum materials concerns systems that do not adhere to the traditional theories of condensed matter physics. A key feature of these materials is a strong coupling between structural, electronic and magnetic degrees of freedom, which is especially prominent in $4d$ and $5d$ transition-metal oxides. The consequences of this coupling are wide, stabilising a range of emergent phases that are sensitive to perturbation. In this thesis, I develop novel techniques based on neutron and x-ray scattering to characterise and control electron-lattice coupling in $4d$ and $5d$ quantum materials.

I begin with $Ca_3Ru_2O_7$, a $4d$ polar metal that hosts a spin-reorientation transition. Using neutron and resonant x-ray scattering, I reveal a new cycloidal magnetic phase, arising from spin-orbit coupling, that rapidly evolves with temperature to mediate the transition. I further show that the cycloid-mediated spin-reorientation can be driven by anisotropic strain, demonstrating the control enabled by coupling to the lattice.

I then turn to resonant inelastic x-ray scattering (RIXS), which has recently received interest as a new probe of electron-phonon coupling (EPC). Using graphite as a model system, I demonstrate the power of RIXS to probe the momentum-dependent EPC for a range of excited electronic states. Our RIXS data reveal some key deficiencies of current theoretical models of phonon excitations in RIXS, and prompt the development of a new Green's-function–based model by our collaborators to address these issues.

Finally, I present a study of the $5d$ material Sr_2IrO_4, a famous $j_{\text{eff}} = 1/2$ spin-orbit Mott insulator. I characterise the phonon spectrum with non-resonant inelastic x-ray scattering, before using RIXS to explore the phonon and magnon excitations. I find a strong EPC similar to that seen in the cuprates, and offer a new interpretation of the magnon dispersion involving coupling to spin-orbit excitons.

Impact Statement

The work presented in this thesis advances our understanding of a range of quantum materials, as well as contributing to the development of new experimental techniques to tune and characterise their properties. These advances are primarily of academic interest to the condensed matter and materials science communities, but also have potential longer-term impacts in the development of new technologies.

The discovery of cycloidal order in $Ca_3Ru_2O_7$ reveals a new mechanism to stabilise modulated magnetism at phase transitions in materials with broken inversion symmetry. The modulations in $Ca_3Ru_2O_7$ are one-dimensional, but higher-dimensional modulations could be realised in other systems. Two-dimensional modulations include structures such as Skyrmions, with their associated topological invariants and potential for spintronic and quantum-computation applications. In this context, the ability to control the modulated structures – as demonstrated here with anisotropic strain – is of particular significance.

The ubiquity and importance of electron-phonon coupling (EPC) in condensed matter systems means that new probes to measure its strength and structure in momentum space are highly sought-after. Resonant inelastic x-ray scattering (RIXS) represents such a probe, and the insights gained from our study of graphite are crucial for a full understanding of phonon excitations in RIXS. As well as being immediately applicable to the other allotropes of carbon, including the celebrated monolayer graphene, our results open a new domain of out-of-equilibrium systems to which RIXS can be brought to bear. This includes photovoltaic materials, whose conversion efficiencies can be strongly affected by EPC, and quantum materials excited with ultrafast laser pulses.

A major focus of RIXS studies of EPC has been the superconducting

cuprates, whose unconventional pairing mechanism remains one of the most pressing unanswered questions in condensed matter physics. One way to elucidate the key ingredients of superconductivity in the cuprates is to study related materials, and in this effort Sr_2IrO_4 has been a significant player. The detailed study of the elementary excitations of Sr_2IrO_4 that I present here reveals many similarities with the cuprates, but also differences arising fundamentally from spin-orbit coupling. This adds to a growing body of research into the ingredients necessary for superconductivity, and those detrimental to it, as well as advancing our understanding of the frontier of spin-orbit coupled correlated materials.

Publications

1. **C. D. Dashwood**, A. Geondzhian, J. G. Vale, A. C. Pakpour-Tabrizi, C. A. Howard, Q. Faure, L. S. I. Veiga, D. Meyers, S. G. Chiuzbăian, A. Nicolaou, N. Jaouen, R. B. Jackman, A. Nag, M. García-Fernández, K.-J. Zhou, A. C. Walters, K. Gilmore, D. F. McMorrow and M. P. M. Dean, *Probing electron-phonon interactions away from the Fermi level with resonant inelastic x-ray scattering*, Phys. Rev. X **11**, 041052 (2021).

2. D. G. Mazzone, D. Meyers, Y. Cao, J. G. Vale, **C. D. Dashwood**, Y. Shi, A. J. A. James, N. J. Robinson, J. Lin, V. Thampy, Y. Tanaka, A. S. Johnson, H. Miao, R. Wang, T. A. Assefa, J. Kim, D. Casa, R. Mankowsky, D. Zhu, R. Alonso-Mori, S. Song, H. Yavas, T. Katayama, M. Yabashi, Y. Kubota, S. Owada, J. Liu, J. Yang, R. M. Konik, I. K. Robinson, J. P. Hill, D. F. McMorrow, M. Först, S. Wall, X. Liu, and M. P. M. Dean, *Laser-induced transient magnons in $Sr_3Ir_2O_7$ throughout the Brillouin zone*, Proc. Natl. Acad. Sci. U.S.A. **118**, e2103696118 (2021).

3. **C. D. Dashwood**, L. S. I. Veiga, Q. Faure, J. G. Vale, D. G. Porter, S. P. Collins, P. Manuel, D. D. Khalyavin, F. Orlandi, R. S. Perry, R. D. Johnson, and D. F. McMorrow, *Spontaneous cycloidal order mediating a spin-reorientation transition in a polar metal*, Phys. Rev. B **102**, 180410 (2020).

4. L. S. I. Veiga, M. Etter, E. Cappelli, H. Jacobsen, J. G. Vale, **C. D. Dashwood**, D. Le, F. Baumberger, D. F. McMorrow, and R. S. Perry, *Correlated electron metal properties of the honeycomb ruthenate Na_2RuO_3*, Phys. Rev. Materials **4**, 094202 (2020).

5. H. Jacobsen, **C. D. Dashwood**, E. Lhotel, D. Khalyavin, P. Manuel,

R. Stewart, D. Prabhakaran, D. F. McMorrow, and A. T. Boothroyd, *Strong quantum fluctuations from competition between magnetic phases in a pyrochlore iridate*, Phys. Rev. B **101**, 104404 (2020).

6. J. G Vale, **C. D. Dashwood**, E. Paris, L. S. I. Veiga, M. Garcia-Fernandez, A. Nag, A. Walters, K.-J. Zhou, I.-M. Pietsch, A. Jesche, P. Gegenwart, R. Coldea, T. Schmitt, and D. F. McMorrow, *High-resolution resonant inelastic x-ray scattering study of the electron-phonon coupling in honeycomb α–Li_2IrO_3*, Phys. Rev. B **100**, 224303 (2019).

7. L. S. I. Veiga, K. Glazyrin, G. Fabbris, **C. D. Dashwood**, J. G. Vale, H. Park, M. Etter, T. Irifune, S. Pascarelli, D. F. McMorrow, T. Takayama, H. Takagi, and D. Haskel, *Pressure-induced structural dimerization in the hyperhoneycomb iridate β–Li_2IrO_3 at low temperatures*, Phys. Rev. B **100**, 064104 (2019).

8. **C. D. Dashwood**, H. Miao, J. G. Vale, D. Ishikawa, D. A. Prishchenko, V. V. Mazurenko, V. G. Mazurenko, R. S. Perry, G. Cao, A. De La Torre, F. Baumberger, A. Q. R. Baron, D. F. McMorrow, and M. P. M. Dean, *Momentum-resolved lattice dynamics of parent and electron-doped Sr_2IrO_4*, Phys. Rev. B **100**, 085131 (2019).

9. D. Pincini, L. S. I. Veiga, **C. D. Dashwood**, F. Forte, M. Cuoco, R. S. Perry, P. Bencok, A. T. Boothroyd, and D. F. McMorrow, *Tuning of the Ru^{4+} ground-state orbital population in the $4d^4$ Mott insulator Ca_2RuO_4 achieved by La doping*, Phys. Rev. B **99**, 075125 (2019).

10. D. Pincini, S. Boseggia, R. Perry, M. J. Gutmann, S. Riccò, L. S. I. Veiga, **C. D. Dashwood**, S. P. Collins, G. Nisbet, A. Bombardi, D. G. Porter, F. Baumberger, A. T. Boothroyd, and D. F. McMorrow, *Persistence of antiferromagnetic order upon La substitution in the $4d^4$ Mott insulator Ca_2RuO_4*, Phys. Rev. B **98**, 014429 (2018).

Acknowledgements

Firstly, I would like to thank Des for his wisdom and guidance over the last four and a half years. I feel incredibly lucky to have had a supervisor who has given me the intellectual freedom to follow my interests (both inside and outside research), backed up by continuous encouragement and a seemingly endless offering of opportunities. There cannot be many PhDs that involve conducting experiments across six different countries, working as part of eight different collaborations, and presenting at five international conferences – and all of that is thanks to Des.

I owe a special thanks to James, Larissa, Davide and Quentin, for teaching me the intricacies of running a scattering experiment and being such wonderful beamtime companions. It has been a joy to get to know you all, and to see the paths that you have all taken after UCL.

None of the work in this thesis would have been possible if not for the high-quality crystals provided by Robin. He was also the first to suggest strain measurements with the Razorbill cells, and has taught me nearly everything that I know about sample preparation.

I would be hard-pressed to imagine a better collaborator than Mark, who has supplied a wealth of research ideas that invariably turn out to be successful. I am very grateful for being welcomed into ongoing projects, and trusted to take the lead on joint ventures.

I have learned an incredible amount from working with Roger since he joined UCL. I am yet to meet anyone else with such perspicacity, deep understanding of symmetry, or love of tackling interesting problems in condensed matter. I come away from every conversation that we have with a new insight, and just wish I'd taken more notes!

I must acknowledge the beamline and instrument staff who have invested so much time, energy and patience into my experiments. Thank you to Marco

at ID20; Alfred at BL43LXU; Peter at I10; Abhishek, Miriam, Andy and Ke-Jin at I21; Pas, Dmitry and Fabio at WISH; and Dan, Gareth and Steve at I16. Dan deserves particular recognition for his support with the strain measurements, which would not have been possible without the vast amount of help (and late-night problem solving) that he provided.

Finally, I extend my gratitude to the whole CDT-ACM. As well as funding, they have given me exposure to a range of different techniques and research areas, and a sense of community. I have appreciated the academic and pastoral support of Neil; the invaluable help with ordering and expenses from Clare, Hafiza and Des; and the friendship of my cohort.

Contents

List of Figures

Chapter 1

Introduction

The physics of quantum materials is governed by a range of interactions whose energy scales depend on the elements that make up the material and their arrangement in the crystalline lattice. The interplay of these interactions generates a plethora of emergent phases, often characterised by coupled degrees of freedom. This chapter introduces the key interactions that act at the single- and multi-ion level in 4*d and* 5*d quantum materials, including crystal fields, Hund's coupling, spin-orbit coupling, and electronic correlations. The* $J_{\mathit{eff}} = 1/2$ *state found in spin-orbit Mott insulators serves as an illustrative example, with the orbital character of the moments resulting in magnetic interactions that are sensitive to the bonding geometry. The chapter concludes with an overview of the experimental x-ray and neutron scattering techniques employed in this thesis.*

1.1 The physics of $4d$ and $5d$ quantum materials

The study of quantum materials containing $4d$ and $5d$ transition-metal ions opened a new paradigm in condensed matter physics, bringing together two threads of research into strongly correlated systems and those with strong spin-orbit coupling (SOC). Strongly correlated systems are exemplified by the $3d$ transition-metal oxides, in which the Hubbard repulsion between electrons occupying the same site tends to localise what would otherwise be itinerant carriers [1]. SOC, a relativistic effect that entangles spin and orbital angular momentum and splits electronic bands, represents only a minimal perturbation

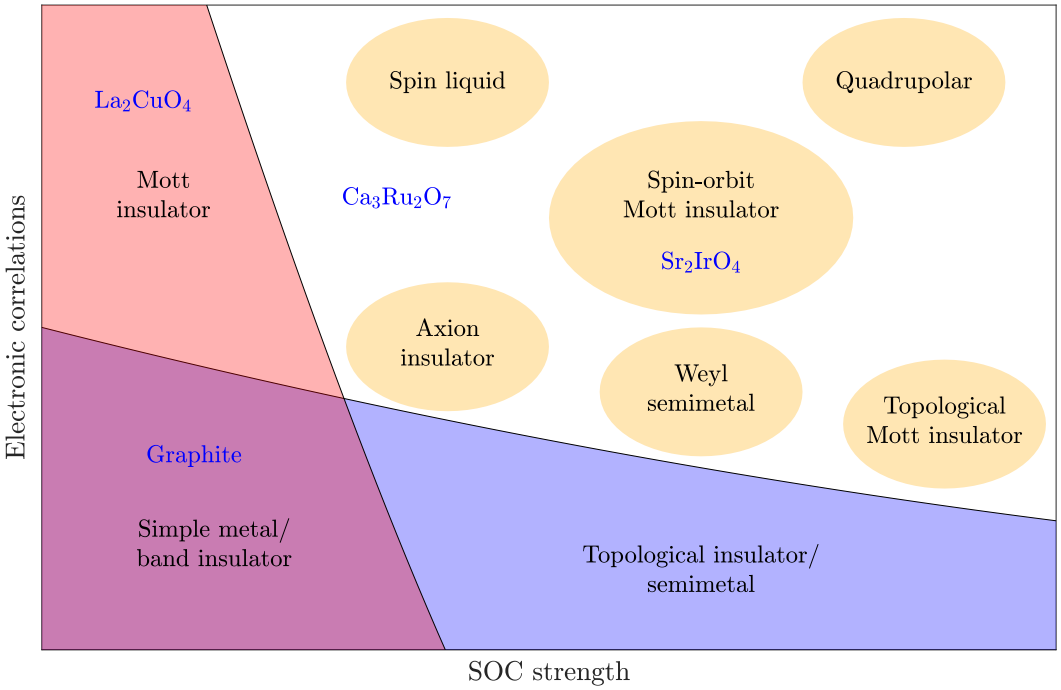

Figure 1.1: Schematic phase diagram of quantum materials as a function of electronic correlations and SOC, with the approximate locations of materials relevant to this thesis indicated. Adapted from Ref. [2].

for the light 3*d* elements. As the atomic number increases, however, its effects quickly become non-negligible.

The interaction between SOC and correlations can be represented in a schematic phase diagram, shown in Fig. 1.1 [2]. The four quadrants represent four limits. In the lower-left corner of weak SOC and weak correlations reside simple metals and insulators that obey conventional band theory (as well as semimetallic graphite used as a case study in Chapter 3). In materials with strong SOC, but still minimal correlations, one finds the topological insulators and semimetals, with their symmetry-protected surface states populated by emergent Dirac and Majorana fermions [3]. Going back to the low-SOC limit, increasing correlations drive a transition from a metallic to a Mott insulating state. One of the most intensively studied families of Mott insulators are the 3*d* cuprates, such as La_2CuO_4, which host antiferromagnetic order that gives way to unconventional superconductivity under chemical doping [1]. The final quadrant, where both correlations and SOC are significant, is populated by a

variety of intriguing phases that depend sensitively on the chemical composition and crystal structure. Just above the topological insulators lie a range of correlated topological phases, for example, including Weyl semimetals [4] and magnetically ordered axion insulators [5].

The $4d$ and $5d$ materials studied in this thesis lie in the central region of intermediate correlations and SOC. Compared to $3d$ materials, the correlations are reduced due to the larger spatial extent of the orbitals. $4d$ materials, such as $Ca_3Ru_2O_7$ studied in Chapter 2, lie on the brink of a Mott transition that depends on the electronic bandwidth [6]. Where local moments form in these materials, SOC acts to generate anisotropic exchange interactions. Moving on to the $5d$ materials, the further reduced correlations may lead one to expect metallic behaviour. Their larger nuclei lead to stronger SOC, however, which lifts orbital degeneracy and produces narrow bands that are more susceptible to localisation. The cooperation of SOC and correlations then gives rise to the so-called "spin-orbit Mott insulators" with entangled $J_{\text{eff}} = 1/2$ pseudospins, including Sr_2IrO_4 studied in Chapter 4 [7].

As hinted at in the above discussion, the two-dimensional phase diagram of Fig. 1.1 is an oversimplification, with a number of other energy scales such as crystal fields and Hund's coupling playing a potentially decisive role in stabilising a particular ground state. In the following sections I give an overview of each of these effects, starting with those that can be understood at the single-ion level, and then treating the interactions of many ions arranged in a crystal lattice. For each, I use simple models to illuminate the physics at play, employing natural units with $\hbar = c = \mu_0 = \epsilon_0 = 1$.

1.1.1 Single-ion physics: crystal fields, Hund's exchange and spin-orbit coupling

The basic building block of the transition-metal oxides studied in this work is a $4d$ or $5d$ ion at the centre of an octahedron of oxygen ions, as depicted in Fig. 1.2(a). In an isolated atom, all five d orbitals are degenerate. Within the oxygen octahedron, however, a cubic crystal field is generated that splits the

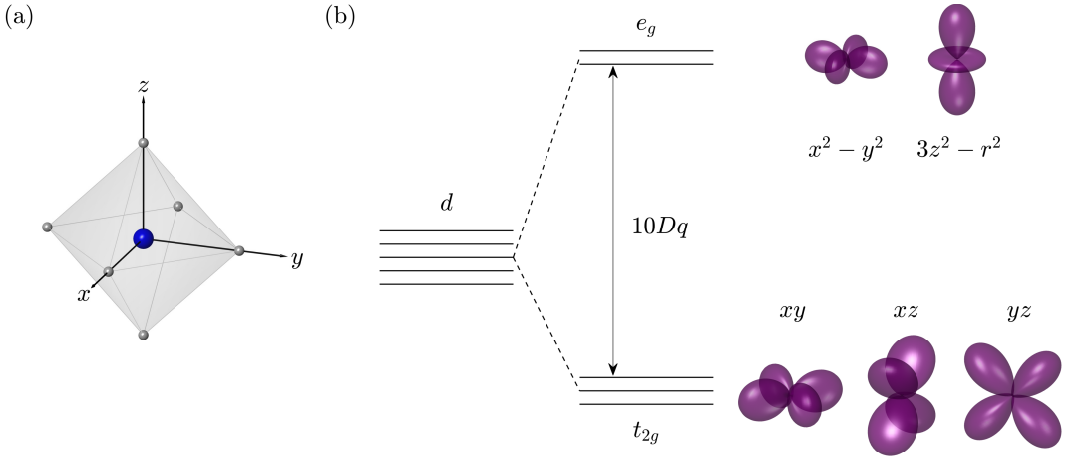

Figure 1.2: (a) Transition-metal ion sitting inside an oxygen octahedron that generates a cubic crystal field. (b) Energy level diagram of the transition-metal d orbitals which are split by the cubic crystal field into an e_g doublet and t_{2g} triplet (not including spin), alongside real-space representations of the angular part of the orbital wavefunctions.

d orbitals into a higher-energy doublet, where the orbital lobes point towards the oxygens, and a lower-energy triplet, where the lobes point between the oxygens. We can calculate an estimate for this splitting in a simple ionic model where the oxygens are treated as point-charges, following Hutchings [8].

Placing the origin at the centre of the octahedron, the electrostatic potential of an electron at $\boldsymbol{r} = (x, y, z)$ due to the six point charges at distance a from the origin is

$$V_{\mathrm{CF}}(\boldsymbol{r}) = \sum_{i,\pm} \frac{Ze^2}{\sqrt{(r_i \pm a)^2 + r_j^2 + r_k^2}} \approx \frac{6Ze^2}{a} + \frac{35Ze^2}{4a^5}\left(\sum_i r_i^4 - \frac{3}{5}r^4\right), \quad (1.1)$$

where in the second step I have Taylor expanded to fourth order in r_i. To find the splitting produced by this potential, we need to express V_{CF} as a matrix in the d-orbital basis, $\{|n, l, m\rangle\}$ with $l = 2$ and $m = -2$ to 2. The orbitals have separable real-space wavefunctions of the form $\langle \boldsymbol{r}|n, 2, m\rangle = R_n^2(r)Y_m^2(\theta, \phi)$, where Y_m^2 are the second-order spherical harmonics. To simplify our calculations it is useful to express V in terms of the fourth-order spherical harmonics,

Y^4_m, as

$$V_{\mathrm{CF}} \approx \frac{6Ze^2}{a} + \frac{7\sqrt{\pi}Ze^2r^4}{3a^5}\left[Y^4_0 + \sqrt{\frac{5}{14}}\left(Y^4_4 + Y^4_{-4}\right)\right]. \tag{1.2}$$

We can now find the matrix elements $\langle n,2,m|V_{\mathrm{CF}}|n,2,m'\rangle$ using the result

$$\int_0^{2\pi}\int_0^{\pi}\left(Y^2_m\right)^* Y^4_n Y^2_{m'}\ \sin\theta\ d\theta\ d\phi = (-1)^m\sqrt{\frac{45}{14\pi}}\begin{pmatrix} 2 & 4 & 2 \\ -m & n & m'\end{pmatrix}, \tag{1.3}$$

where the final bracketed term is a Wigner $3j$-symbol [9]. This gives the matrix

$$V_{\mathrm{CF}} \approx Dq\begin{pmatrix} 1 & 0 & 0 & 0 & 5 \\ 0 & -4 & 0 & 0 & 0 \\ 0 & 0 & 6 & 0 & 0 \\ 0 & 0 & 0 & -4 & 0 \\ 5 & 0 & 0 & 0 & 1\end{pmatrix}, \tag{1.4}$$

where $Dq = \frac{Ze^2\langle r^4\rangle}{6a^5}$ with $\langle r^4\rangle = \int |R_{n,2}|^2\ r^4\ dr$. Diagonalising this matrix results in a doublet of eigenvectors of e_g symmetry with eigenvalue $\langle V_{\mathrm{CF}}\rangle = 6Dq$:

$$\left|3z^2 - r^2\right\rangle = |n,2,0\rangle\,, \tag{1.5}$$

$$\left|x^2 - y^2\right\rangle = \frac{1}{\sqrt{2}}\left(|n,2,-2\rangle + |n,2,2\rangle\right); \tag{1.6}$$

and a triplet of eigenvectors of t_{2g} symmetry with eigenvalue $\langle V_{\mathrm{CF}}\rangle = -4Dq$:

$$|xy\rangle = \frac{i}{\sqrt{2}}\left(|n,2,-2\rangle - |n,2,2\rangle\right), \tag{1.7}$$

$$|xz\rangle = \frac{1}{\sqrt{2}}\left(|n,2,-1\rangle - |n,2,1\rangle\right), \tag{1.8}$$

$$|yz\rangle = \frac{i}{\sqrt{2}}\left(|n,2,-1\rangle + |n,2,1\rangle\right). \tag{1.9}$$

Our simple model therefore predicts a splitting of $10Dq$. A more detailed calculation would include the finite extent of the oxygen wavefunctions, the effects

of neighbouring octahedra, and screening. In real $4d$ systems the splitting is found to be $10Dq \approx 2\,\text{eV}$, while in $5d$ systems it is $\approx 3\,\text{eV}$ [10].

The next-highest energy scale affecting the $4d/5d$ ion is that of Hund's exchange, $J_H \approx 0.6\,\text{eV}$ [10]. This stems from the empirical Hund's rules, the first of which states that the lowest-energy filling of otherwise degenerate orbitals is that which maximises the total spin (subject to Pauli exclusion). Hund's first rule therefore favours singly occupied orbitals, which are less effectively screened from the nucleus and so have an enhanced Coulomb attraction (i.e. lower-energy). For the $4d^4$ and $5d^5$ materials studied here, $J_H << 10Dq$ such that all of the electrons reside in the t_{2g} levels and we can usually neglect the presence of the e_g orbitals. Hund's exchange then maximises the total spin within the t_{2g} triplet. In the case of a half-filled t_{2g} triplet, the effective Hubbard repulsion is increased by Hund's exchange to $U_{\text{eff}} = U + 2J_H$, while for any other filling it is reduced to $U_{\text{eff}} = U - 3J_H$ [11].

Finally at the single-ion level we have SOC, which arises from the relativistic interaction between the angular momentum of an electron and the charge of the nucleus about which it orbits. For a single electron, the SOC Hamiltonian

$$H_{\text{SOC}} = \zeta \boldsymbol{l} \cdot \boldsymbol{s} \tag{1.10}$$

combines the orbital angular momentum, $\boldsymbol{l}$, and spin, $\boldsymbol{s}$, into a total angular momentum $\boldsymbol{j} = \boldsymbol{l} + \boldsymbol{s}$. In multi-electron atoms, the action of SOC depends on its magnitude relative to inter-orbital Coulomb repulsion: when the former dominates, the total angular momentum of each electron is calculated as $\boldsymbol{j}_i = \boldsymbol{l}_i + \boldsymbol{s}_i$ before being summed to give $\boldsymbol{J} = \sum_i \boldsymbol{j}_i$ (jj coupling); when the latter dominates, the total orbital angular momentum, $\boldsymbol{L} = \sum_i \boldsymbol{l}_i$, and spin, $\boldsymbol{S} = \sum_i \boldsymbol{s}_i$, are calculated before being coupled as $\boldsymbol{J} = \boldsymbol{L} + \boldsymbol{S}$ (LS coupling). The materials studied in this thesis are technically intermediate between these limits, but the LS coupling scheme serves as a reasonable approximation. The

SOC Hamiltonian then becomes

$$H_{\mathrm{SOC}} = \lambda \boldsymbol{L} \cdot \boldsymbol{S}, \tag{1.11}$$

where $\lambda = \pm\zeta/(2S)$ with the + (−) sign for less (more) than half-filled shells (leading to Hund's third rule). The coupling constant scales as the fourth power of the atomic number, increasing from $\lambda \approx 0.2\,\mathrm{eV}$ in $4d$ materials to $\lambda \approx 0.5\,\mathrm{eV}$ in $5d$ materials [10]. In both cases $\lambda < J_H \ll 10Dq$ such that we can treat SOC as a perturbation to the t_{2g} levels.

To demonstrate the effects of SOC on the t_{2g} orbitals, I use the example of the $J_{\mathrm{eff}} = 1/2$ state realised in Sr_2IrO_4. I first project the orbital angular momentum operator $\boldsymbol{L}$ onto the t_{2g} manifold. The matrix representations of L_x, L_y and L_z in the t_{2g} basis, $\{|xy\rangle, |xz\rangle, |yz\rangle\}$, are given by

$$L_x = \begin{pmatrix} 0 & i & 0 \\ -i & 0 & 0 \\ 0 & 0 & 0 \end{pmatrix}, \qquad L_y = \begin{pmatrix} 0 & 0 & -i \\ 0 & 0 & 0 \\ i & 0 & 0 \end{pmatrix}, \qquad L_z = \begin{pmatrix} 0 & 0 & 0 \\ 0 & 0 & i \\ 0 & -i & 0 \end{pmatrix}, \tag{1.12}$$

which are equivalent to those for an orbital angular momentum of $L_{\mathrm{eff}} = -1$ [12]. The matrix elements for the neglected e_g manifold are all zero. The SOC eigenstates can then be found by expressing H_{SOC} as a matrix in the $t_{2g} \otimes spin$ basis $\{|xy,+\rangle, |xy,-\rangle, |xz,+\rangle, |xz,-\rangle, |yz,+\rangle, |yz,-\rangle\}$. Using the above expressions for L_x, L_y and L_z, we find

$$\begin{aligned} H_{\mathrm{SOC}} &= \lambda \left(L_x \otimes S_x + L_y \otimes S_y + L_z \otimes S_z\right) \\ &= \frac{\lambda}{2} \begin{pmatrix} 0 & 0 & 0 & i & 0 & -1 \\ 0 & 0 & i & 0 & 1 & 0 \\ 0 & -i & 0 & 0 & i & 0 \\ -i & 0 & 0 & 0 & 0 & -i \\ 0 & 1 & -i & 0 & 0 & 0 \\ -1 & 0 & 0 & i & 0 & 0 \end{pmatrix}, \end{aligned} \tag{1.13}$$

where $S_i = \sigma_i/2$ with $\{\sigma_i\}$ the Pauli spin matrices. The Hamiltonian in Eq. (1.13) has a $J_{\text{eff}} = 3/2$ quartet of eigenvectors $|J_{\text{eff}}, m_J\rangle$ with eigenvalue $\langle H_{\text{SOC}}\rangle = -\lambda/2$:

$$\left|\frac{3}{2}, \pm\frac{3}{2}\right\rangle = \frac{1}{\sqrt{6}}\left(\mp 2\,|xy, \pm\rangle + |yz, \mp\rangle \pm i\,|xz, \mp\rangle\right), \tag{1.14}$$

$$\left|\frac{3}{2}, \pm\frac{1}{2}\right\rangle = \frac{1}{\sqrt{2}}\left(|yz, \pm\rangle \pm i\,|xz, \pm\rangle\right); \tag{1.15}$$

and a $J_{\text{eff}} = 1/2$ Kramers doublet of eigenvectors with eigenvalue $\langle H_{\text{SOC}}\rangle = \lambda$:

$$\left|\frac{1}{2}, \pm\frac{1}{2}\right\rangle = \frac{1}{\sqrt{3}}\left(\pm\,|xy, \pm\rangle + |yz, \mp\rangle \pm i\,|xz, \mp\rangle\right). \tag{1.16}$$

SOC therefore splits the t_{2g} levels by an energy $3\lambda/2$, as depicted in Fig. 1.3. Four of the five $5d$ electrons in Sr_2IrO_4 fill the lower energy $J_{\text{eff}} = 3/2$ states, leaving the $J_{\text{eff}} = 1/2$ doublet half-filled. The low-energy dynamics can therefore be accounted for with a single $J_{\text{eff}} = 1/2$ hole of pseudospin 1/2. Note that in the real material the oxygen octahedra are slightly distorted, causing an effective mixing of the $J_{\text{eff}} = 1/2$ and $J_{\text{eff}} = 3/2$ states.

Having built the basic structural unit that makes up the $4d$ and $5d$ materials under study, I now consider the interactions between the units when assembled into a crystalline lattice.

1.1.2 Multi-ion physics: electronic correlations, Mott transitions and magnetic interactions

The essential physics of correlated electron systems is captured by the Hubbard Hamiltonian, which contains just two terms [13]

$$H = \sum_{\langle i,j\rangle,\sigma} t_{ij}^{\sigma} c_{i\sigma}^{\dagger} c_{j\sigma} + U \sum_i n_{i+} n_{i-}, \tag{1.17}$$

where $c_{i\sigma}^{\dagger}$ ($c_{i\sigma}$) creates (annihilates) an electron of spin σ at site i, t_{ij}^{σ} is the spin-dependent hopping integral between adjacent sites $\langle i, j\rangle$, U is the strength of the local Coulomb interaction between two electrons on the same site, and

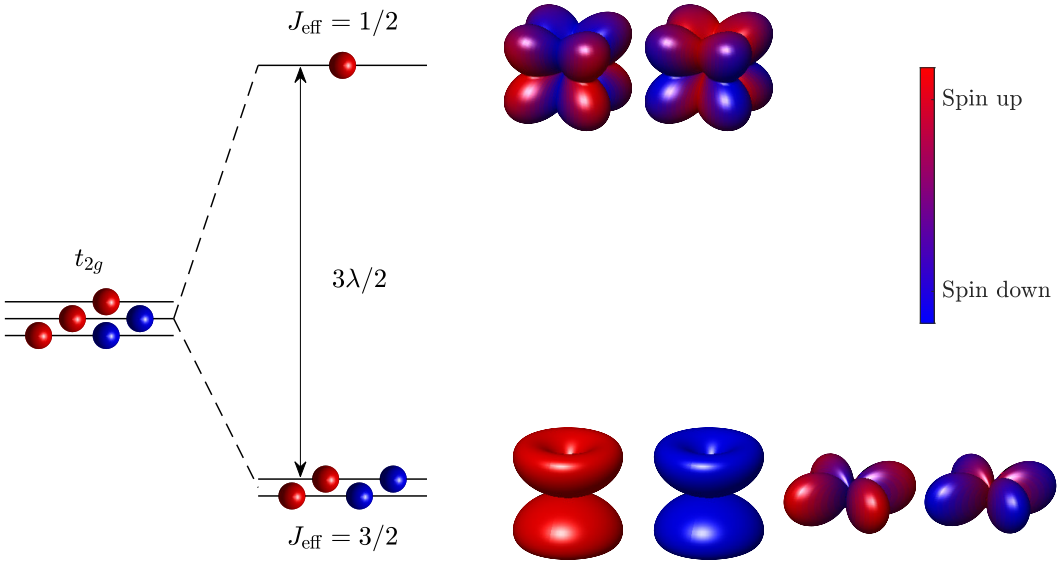

Figure 1.3: Energy level diagram of the crystal-field t_{2g} levels split by SOC into a $J_{\text{eff}} = 3/2$ quartet and $J_{\text{eff}} = 1/2$ doublet, alongside real-space representations of the angular part of the wavefunctions with colours indicating the spin. In an Ir^{4+} ion there are five d electrons, four of which fill the $J_{\text{eff}} = 3/2$ levels leaving the $J_{\text{eff}} = 1/2$ states half filled.

$n_{i\sigma} = c^{\dagger}_{i\sigma}c_{i\sigma}$ is the number of electrons at site i. The two terms in Eq. (1.17) are in direct competition: the first term, which represents a tight binding model, promotes itinerancy and the formation of energy bands; the second term, meanwhile, introduces correlations that want to localise the electrons.

With one electron per site ($n = 1$), the Hubbard Hamiltonian famously describes a Mott-Hubbard metal-insulator transition with increasing U. For $U \ll t$, a single half-filled band at the Fermi level leads to a metallic state. As the correlations are increased above a critical value $U/t \sim 1$, the band splits into a filled lower Hubbard band and empty upper Hubbard band separated by an energy gap, forming a Mott insulating state [1]. In the strongly correlated limit $U \gg t$, the electrons are fully localised on the lattice sites and can give rise to local magnetic moments. By treating the hopping as a small perturbation in this state, the charge degrees of freedom can be projected out and the Hubbard Hamiltonian reduced to an effective spin Hamiltonian

$$H = \sum_{\langle i,j \rangle} \frac{4t_{ij}^2}{U} \boldsymbol{S}_i \cdot \boldsymbol{S}_j, \tag{1.18}$$

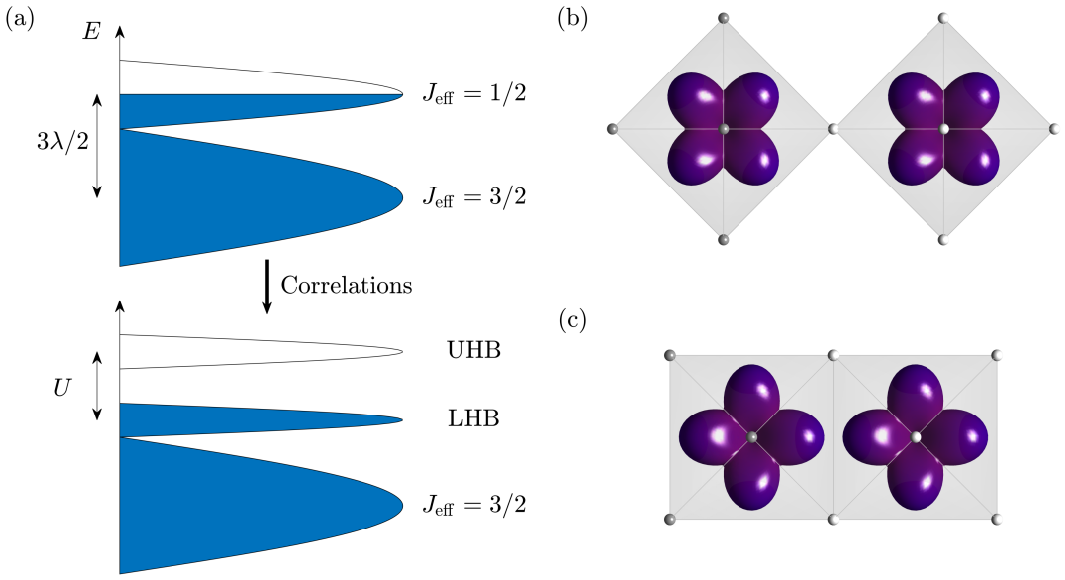

Figure 1.4: (a) Energy band diagrams for a d^5 spin-orbit Mott insulator, with a half-filled $J_{\text{eff}} = 1/2$ band split by correlations into a filled lower Hubbard band (LHB) and empty upper Hubbard band (UHB). (b) Corner-sharing octahedra forming a 180° superexchange pathway. (c) Edge-sharing octahedra forming a 90° superexchange pathway.

with $\boldsymbol{S}_i$ the spin on site i. This particular form of spin Hamiltonian is known as the Heisenberg Hamiltonian, with the isotropic exchange parameter $J = 4t^2/U$ arising from the double hopping process $i \to j \to i$ involved in superexchange [14]. In this case $J > 0$, resulting in antiferromagnetic order with antiparallel spins on neighbouring sites.

The Hubbard repulsion in $4d$ materials is roughly $U \approx 3\,\text{eV}$, while for $5d$ materials $U \approx 1\,\text{eV}$ [10]. Whereas the Hamiltonian in Eq. (1.17) describes only a single electronic band, real materials often have a number of active bands near the Fermi level. Combined with the variations in hopping given by the range of possible crystal structures, this results in a diverse collection of ground states. For Sr_2IrO_4, however, we have seen that the single-ion physics can be reduced to that of a single hole in a $J_{\text{eff}} = 1/2$ doublet. The half-filled, single-band Hubbard model can therefore be directly applied to Sr_2IrO_4, with $c^\dagger_{i\sigma}$ ($c_{i\sigma}$) now creating (annihilating) a $J_{\text{eff}} = 1/2$ hole of pseudospin $\sigma = \pm$ at site i. The impact of correlations on the electronic bands of Sr_2IrO_4 is illustrated in Fig. 1.4(a). While the full t_{2g} bandwidth is too large to be

split by the moderate U, the SOC-split $J_{\text{eff}} = 1/2$ band is narrow enough for correlations to open a charge gap. The integral role of SOC in driving the Mott insulating ground state is the reason that Sr_2IrO_4 is known as a "spin-orbit Mott insulator".

From the above discussion of the formation of local magnetic moments in Mott insulators, a natural question is how the effective spin Hamiltonian is altered by the orbital character of the $J_{\text{eff}} = 1/2$ pseudospins. Pioneering work by Jackeli and Khaliullin [12] showed that the answer depends profoundly on the bonding geometry. For superexchange mediated by an intermediate oxygen ion, there are two limiting geometries. The first is a 180° bond corresponding to corner-sharing octahedra, as depicted in Fig. 1.4(b). In this case the spin Hamiltonian has only a small modification to the Heisenberg interaction

$$H = \sum_{\langle i,j \rangle} J \boldsymbol{S}_i \cdot \boldsymbol{S}_j + \Gamma(\boldsymbol{S}_i \cdot \boldsymbol{r}_{ij})(\boldsymbol{r}_{ij} \cdot \boldsymbol{S}_j), \tag{1.19}$$

where $\boldsymbol{S}_i$ is now a pseudospin operator, and $\boldsymbol{r}_{ij}$ is the unit vector between sites i and j. The anisotropic second term is a pseudodipolar interaction that results from Hund's coupling, with $\Gamma/J \sim J_H/(2U) \ll 1$. Sr_2IrO_4 is close to this limit, with small staggered rotations of the octahedra about the out-of-plane direction that the spins follow rigidly. The effective magnetic Hamiltonian for Sr_2IrO_4 will be investigated in Chapter 4.

The other geometry is a 90° bond corresponding to edge-sharing octahedra, as depicted in Fig. 1.4(c). There are now two equivalent exchange paths via the upper or lower oxygen, across which the Heisenberg interaction destructively interferes. The pseudodipolar interaction is left as the dominant term, which can be recast as

$$H = \sum_{\langle i,j \rangle} K^\gamma S_i^\gamma S_j^\gamma \tag{1.20}$$

for a bond lying perpendicular to the γ direction. On a honeycomb lattice, this

Hamiltonian is recognisable as the exactly solvable Kitaev model [15], whose ground state is a quantum spin liquid with fractional Majorana excitations. A range of $4d$ and $5d$ materials, including $RuCl_3$ [16] and $(Li/Na)_2IrO_3$ [17, 18] have been proposed as realisations of the Kitaev model, although in most cases other subdominant exchange interactions drive magnetic ordering at low temperature and obscure the spin liquid state.

1.2 Neutron and x-ray scattering

The main experimental techniques used throughout this thesis are neutron and x-ray scattering. In both techniques, a beam of probe particles (either neutrons or photons, with wavelengths comparable to the interatomic distances) is incident on a sample and any changes to their momentum, energy or polarisation due to interactions with the sample are measured. The ground state of the sample can be probed through elastic scattering, in which the incident and outgoing particles have the same energy, while dynamics can be probed by transferring energy to the sample in inelastic scattering. Neutron and x-ray scattering each have their own strengths and weaknesses, and in many ways are complementary. Thermal neutrons are a well-established probe of order and excitations in condensed matter, with a lack of electric charge allowing them to penetrate deep into the bulk of a sample, and their intrinsic magnetic moment giving sensitivity to the magnetic structure. With a relatively low flux, however, neutron scattering requires single-crystal samples of a size that is often unobtainable, especially if they contain highly neutron-absorbing elements such as Ir. Third-generation synchrotron sources, meanwhile, provide highly collimated, high-fluence beams of variable polarisation that are tuneable across the x-ray spectrum. These allow high-resolution studies of small samples, especially when utilising the resonant scattering enhancement obtained by tuning the incident x-rays to a particular absorption edge. While providing a wealth of information, the complexity of the resonant process can make it difficult to interpret experimental data (as highlighted in Chapter 3).

The quantity measured in both neutron and x-ray scattering is the differential cross section $\frac{d^2\sigma}{d\Omega d\omega}$, which corresponds to the number of particles with energies in interval $d\omega$ scattered into a solid angle $d\Omega$ per second. The value of the cross section depends on the details of the probe and scatterer, as expounded in the following sections. Much can be understood at a general level, however, by considering the scattering of nondescript particles from an abstract crystalline lattice and applying energy and momentum conservation. Starting with elastic scattering, the incoming and outgoing wavevectors of the particles must have equal magnitude $|\boldsymbol{k}_i| = |\boldsymbol{k}_f| = 2\pi/\lambda$ where λ is their de Broglie wavelength. The momentum transfer to the sample is $\boldsymbol{q} = \boldsymbol{k}_i - \boldsymbol{k}_f$, with a magnitude $|\boldsymbol{q}| = 2k \sin\Theta$ where 2Θ is the scattering angle between $\boldsymbol{k}_i$ and $\boldsymbol{k}_f$. The Laue condition tells us that constructive interference of the scattered particles will occur when the momentum transfer is equal to a reciprocal lattice vector, $\boldsymbol{G}_{hkl}$, of magnitude $|\boldsymbol{G}_{hkl}| = 2\pi/d_{hkl}$. Here, d_{hkl} is the spacing between lattice planes normal to $\boldsymbol{G}_{hkl}$ with Miller indices (h, k, l). Equating $|\boldsymbol{q}| = |\boldsymbol{G}_{hkl}|$ then gives us Bragg's law

$$\lambda = 2d_{hkl} \sin\Theta. \tag{1.21}$$

Equation (1.21) describes a series of "Bragg peaks" at specific scattering angles that depend on the lattice constants of the sample via d_{hkl}. The symmetry of the lattice leads to selection rules for the allowed peaks, with systematic absences for certain combinations of h, k and l.

For inelastic scattering, the difference in energy between the incident and outgoing particle is equal to the energy of the excitation that is created. Mapping this energy as a function of momentum transfer then gives the dispersion relation for that excitation.

In the following sections, I evaluate the differential cross section for the cases of neutron scattering (both from the arrangement of nuclei and magnetic moments in a crystal) following Squires [19], non-resonant x-ray scattering following Baron [20], and resonant x-ray scattering following Altarelli [21].

1.2.1 Neutron scattering

We can describe the neutron scattering process as a transition between two quantum states driven by an interaction Hamiltonian, H'. We denote the initial combined state $|i;\boldsymbol{k}_i\rangle$, with the incident neutron in state $|\boldsymbol{k}_i\rangle$ and the scatterer in state $|i\rangle$, and the final combined state $|f;\boldsymbol{k}_f\rangle$ similarly. The differential cross section, which is just the rate of such transitions, is then given by Fermi's Golden Rule as

$$\frac{d^2\sigma}{d\Omega d\omega} = \frac{2\pi}{\Phi d\Omega} |\langle f;\boldsymbol{k}_f|H'|i;\boldsymbol{k}_i\rangle|^2 \rho(\omega_f)\delta(\omega_i - \omega_f - E_i + E_f), \tag{1.22}$$

where $\langle f;\boldsymbol{k}_f|H'|i;\boldsymbol{k}_i\rangle$ is the matrix element representing the transition probability, $\rho(\omega_f)$ is the density of final states, Φ is the incident neutron flux, and ω and E are the energies of the neutrons and scatterer respectively. For a beam of neutrons in volume V moving with speeds $v_i = d\omega_i/dk = k_i/m_n$, the incident flux is $\Phi = v_i/V = k_i/(Vm_n)$. We can calculate the density of final states by considering the number of neutrons in a corresponding volume of reciprocal space, $\rho d\omega = Vk^2 dk d\Omega/(2\pi)^3$, which gives $\rho(\omega_f) = Vm_n k_f d\Omega/(2\pi)^3$. Plugging these into Eq. (1.22), we get

$$\frac{d^2\sigma}{d\Omega d\omega} = \frac{k_f}{k_i}\left(\frac{m_n}{2\pi}\right)^2 |\langle f;\boldsymbol{k}_f|H'|i;\boldsymbol{k}_i\rangle|^2 \delta(\omega_i - \omega_f - E_i + E_f), \tag{1.23}$$

where the wavefunctions have been normalised by $V^{-1/2}$.

We will first evaluate Eq. (1.23) for nuclear scattering from a crystal with lattice sites $\{\boldsymbol{R}_j\}$. Due to the negligible size of a nucleus, the interaction can be approximated by the Fermi pseudopotential

$$H' = \frac{2\pi}{m_n}\sum_j b_j \delta(\boldsymbol{r} - \boldsymbol{R}_j), \tag{1.24}$$

where the scattering length, b_j, is a constant for a particular spin state of a given isotope. It is easier to work in reciprocal space, where the matrix element

takes on a simple form

$$\langle f; \boldsymbol{k}_f | H' | i; \boldsymbol{k}_i \rangle = \frac{2\pi}{m_n} \sum_j b_j \langle f | e^{i\boldsymbol{q}\cdot\boldsymbol{R}_j} | i \rangle . \tag{1.25}$$

In this thesis, we are only concerned with elastic neutron scattering in which no energy is lost by the neutrons ($k_f = k_i$) and the crystal returns to its original state ($|f\rangle = |i\rangle$). We can then integrate over the neutron energy to get the single-differential cross section

$$\frac{d\sigma}{d\Omega} = \sum_{j,k} b_j b_k e^{i\boldsymbol{q}\cdot(\boldsymbol{R}_j - \boldsymbol{R}_k)}. \tag{1.26}$$

For a crystal with many nuclei, the cross section is equivalent to that averaged over all distributions of scattering lengths among the nuclei. This allows us to separate out two contributions for $j \neq k$ and $j = k$ respectively

$$\frac{d\sigma}{d\Omega} = \langle b \rangle^2 \sum_{j,k} e^{i\boldsymbol{q}\cdot(\boldsymbol{R}_j - \boldsymbol{R}_k)} + (\langle b^2 \rangle - \langle b \rangle^2). \tag{1.27}$$

The first term is called the coherent cross section, and contains the average of the scattering lengths in the crystal, $\langle b \rangle$. The second term is called the incoherent cross section, and contributes an isotropic background proportional to the variance of the scattering lengths. In most crystals there are multiple atoms in each unit cell such that we must partition the sum in the coherent differential cross section to one over lattice sites, $\boldsymbol{R}_j$, and another over the atomic basis, $\boldsymbol{r}_\alpha$, giving

$$\begin{aligned} \frac{d\sigma}{d\Omega} &= \sum_{j,k} e^{i\boldsymbol{q}\cdot(\boldsymbol{R}_j - \boldsymbol{R}_k)} \sum_{\alpha,\beta} b_\alpha b_\beta e^{i\boldsymbol{q}\cdot(\boldsymbol{r}_\alpha - \boldsymbol{r}_\beta)} \\ &= \frac{N(2\pi)^3}{V} \sum_{\boldsymbol{G}_{hkl}} |F(\boldsymbol{G}_{hkl})|^2 \delta(\boldsymbol{q} - \boldsymbol{G}_{hkl}), \end{aligned} \tag{1.28}$$

where in the second step we take the Fourier transform $\sum_j e^{i\boldsymbol{q}\cdot\boldsymbol{R}_j} = N(2\pi)^3/V \sum_{\boldsymbol{G}_{hkl}} \delta(\boldsymbol{q} - \boldsymbol{G}_{hkl})$ with N the number of lattice sites. Equation

1.28 contains the nuclear structure factor, $F(\boldsymbol{G}_{hkl}) = \sum_\alpha b_\alpha e^{i\boldsymbol{G}_{hkl}\cdot\boldsymbol{r}_\alpha}$, whose squared modulus gives the intensity of the Bragg peak at (h, k, l). Finally, I note that a more complex analysis that accounts for the thermal motion of the nuclei gives an additional Debye-Waller factor, $e^{-2q^2\langle u^2\rangle/3}$, where $\langle u^2\rangle$ is the mean squared displacements of the nuclei.

As well as the nuclei in a crystal, neutrons can also scatter from magnetic fields due to their intrinsic moment, $\boldsymbol{\mu}_n = -\gamma_n\mu_N\boldsymbol{\sigma}$, where γ_n is the neutron gyromagnetic ratio, μ_N is the nuclear magneton, and $\boldsymbol{\sigma}$ is the vector of Pauli spin matrices. The interaction Hamiltonian is now

$$H' = -\boldsymbol{\mu}_n \cdot \boldsymbol{B}(\boldsymbol{r}) = -\frac{\gamma_n\mu_N\mu_B}{2\pi}\sum_j \boldsymbol{\sigma}\cdot\left[\nabla\times\left(\frac{\boldsymbol{s}_j\times\hat{\boldsymbol{r}}_j}{r_j^2}\right) + \frac{\boldsymbol{l}_j\times\hat{\boldsymbol{r}}_j}{r_j^2}\right], \quad (1.29)$$

which depends on both the spins $\boldsymbol{s}_j$ and orbital angular momenta $\boldsymbol{l}_j$ of the scatterer. Putting this into Eq. (1.23), transforming to reciprocal space and integrating over the outgoing energy gives the single-differential magnetic cross section [19]

$$\frac{d\sigma}{d\Omega} = \frac{N(2\pi)^3}{V}\left(\frac{\gamma_n r_0}{2\mu_B}\right)^2 e^{-2q^2\langle u^2\rangle/3}|\boldsymbol{M}_\perp(\boldsymbol{q})|^2, \quad (1.30)$$

where $r_0 = e^2/(4\pi m_e)$ is the radius of an electron with charge e and mass m_e, $\boldsymbol{M}(\boldsymbol{q})$ is the Fourier transform of the total (spin and orbital) magnetisation operator, and subscript $\perp$ indicates that only the component of the magnetisation perpendicular to $\boldsymbol{q}$ contributes to the scattering.

The magnetic structure of a crystal is characterised by a propagation vector, $\boldsymbol{k}$, and the moment at each site can be represented by a sum over Fourier components, $\boldsymbol{S}_{\boldsymbol{k},\alpha}$, as

$$\boldsymbol{m}_{j,\alpha} = \sum_{\pm\boldsymbol{k}} \boldsymbol{S}_{\boldsymbol{k},\alpha} e^{-2\pi i\boldsymbol{k}\cdot\boldsymbol{r}_j}. \quad (1.31)$$

This allows the magnetisation operator to be expressed as

$$\boldsymbol{M}(\boldsymbol{q}) = \frac{g}{2}\sum_{\pm\boldsymbol{k},\alpha} F_\alpha(\boldsymbol{q})\boldsymbol{S}_{\boldsymbol{k},\alpha} e^{-2\pi i\boldsymbol{q}\cdot\boldsymbol{r}_\alpha}\delta(\boldsymbol{q}-\boldsymbol{G}_{hkl}-\boldsymbol{k}), \quad (1.32)$$

where g is the Landé factor and $F_\alpha(\boldsymbol{q})$ is the magnetic form factor for the atom located at $\boldsymbol{r}_\alpha$. Much like for elastic nuclear scattering, Eq. (1.30) describes a series of peaks at reciprocal positions $\boldsymbol{G}_{hkl} \pm \boldsymbol{k}$ with systematic absences based on the symmetries of the magnetic structure.

The neutron scattering measurements presented in Chapter 2 were conducted at the WISH instrument of the ISIS Neutron and Muon Source [22]. ISIS is a spallation source that produces intense neutron pulses at a rate of 10 Hz by bombarding a tantalum target with protons accelerated in a synchrotron. Those neutrons directed to WISH are then thermalised by a solid methane moderator to reduce their energies, and a specific range of wavelengths between 1.5–15 eV is selected using rotating choppers. WISH uses the time-of-flight of the neutrons to differentiate their wavelengths, allowing multiple peaks at different d spacing to be measured at a single scattering angle. Combined with a large bank of ^{3}He detectors covering scattering angles from 10° to 170°, this enables measurements over a d-spacing range of 0.7–50 Å. Further details of the experimental setups used at WISH are given in Sec. 2.2.1 and 2.3.1.

1.2.2 Non-resonant x-ray scattering

X-ray scattering involves the interaction of the incident electromagnetic field with the charges and spins of the electrons in the sample (the interactions with nuclei are around two orders of magnitude weaker and can be neglected for our purposes). For non-resonant scattering, where the incident x-ray energy is far from any absorption edges of the sample, we can again use Fermi's Golden Rule to first order to calculate the differential cross section. Unlike neutrons, however, x-ray photons are massless and have a fixed speed $c = 1$ (in natural units). The incident flux therefore becomes $\Phi = 1/V$ and the density of final states $\rho(\omega_f) = Vk_f^2 d\Omega/(2\pi)^3$, giving a differential cross section

$$\frac{d^2\sigma}{d\Omega d\omega} = \left(\frac{Vk_f}{2\pi}\right)^2 |\langle f; \boldsymbol{k}_f | H' | i; \boldsymbol{k}_i \rangle|^2 \delta(\omega_i - \omega_f - E_i + E_f). \tag{1.33}$$

The electromagnetic field of the x-rays is described by the vector potential, $\boldsymbol{A}(\boldsymbol{r},t)$, which can be written in second-quantised form as a sum of plane waves

$$\boldsymbol{A}(\boldsymbol{r},t)=\sum_{\boldsymbol{k},\boldsymbol{\varepsilon}}\sqrt{\frac{2\pi}{V\omega_{\boldsymbol{k}}}}\left(\boldsymbol{\varepsilon}a_{\boldsymbol{k},\boldsymbol{\varepsilon}}e^{i(\boldsymbol{k}\cdot\boldsymbol{r}-\omega_{\boldsymbol{k}}t)}+\boldsymbol{\varepsilon}^{*}a^{\dagger}_{\boldsymbol{k},\boldsymbol{\varepsilon}}e^{-i(\boldsymbol{k}\cdot\boldsymbol{r}-\omega_{\boldsymbol{k}}t)}\right), \tag{1.34}$$

where $a^{\dagger}_{\boldsymbol{k},\boldsymbol{\varepsilon}}$ ($a_{\boldsymbol{k},\boldsymbol{\varepsilon}}$) creates (annihilates) a photon of wavevector $\boldsymbol{k}$, energy $\omega_{\boldsymbol{k}}$ and polarisation $\boldsymbol{\varepsilon}$. The full Hamiltonian for the light-matter system can then be written as

$$\begin{aligned}H=\sum_{j}\frac{|\boldsymbol{p}_j-e\boldsymbol{A}|^2}{2m_e}+\phi(\boldsymbol{r}_j)-\frac{e}{m_e}\boldsymbol{s}_j\cdot\boldsymbol{B}-\frac{e}{2m_e^2}\boldsymbol{s}_j\cdot\boldsymbol{E}\times(\boldsymbol{p}_j-e\boldsymbol{A})\\+\sum_{\boldsymbol{k},\boldsymbol{\varepsilon}}\omega_{\boldsymbol{k}}\left(a^{\dagger}_{\boldsymbol{k},\boldsymbol{\varepsilon}}a_{\boldsymbol{k},\boldsymbol{\varepsilon}}+\frac{1}{2}\right),\end{aligned} \tag{1.35}$$

where $\boldsymbol{p}_j$ is the momentum and $\boldsymbol{s}_j$ is the spin of the j^{th} electron, $\phi(\boldsymbol{r})$ is the Coulomb potential of the electrons, $\boldsymbol{B}=\nabla\times\boldsymbol{A}$ is the magnetic field of the x-rays, and $\boldsymbol{E}=-\nabla\phi-\frac{\partial\boldsymbol{A}}{\partial t}$ is their electric field. In the first line of Eq. (1.35), the first term represents the kinetic energy of the electrons, the second their Coulomb potential, the third the Zeeman coupling between their spins and the magnetic field, and the fourth spin-orbit coupling. The interaction Hamiltonian is then given by the terms in H that couple the electrons (through $\boldsymbol{p}_j$ or $\boldsymbol{s}_j$) to the x-rays (through $\boldsymbol{A}$, $\boldsymbol{B}$ or $\boldsymbol{E}$).

The initial and final states in the scattering process both contain a single photon, so the terms in Eq. (1.35) that will give a non-zero first-order matrix element, $\langle f;\boldsymbol{k}_f|H'|i;\boldsymbol{k}_i\rangle$, are those that are quadratic in $\boldsymbol{A}$ (i.e. proportional to $a^{\dagger}a$ or $aa^{\dagger}$)

$$H'=\sum_{j}\frac{e^2}{2m_e}|\boldsymbol{A}|^2-\frac{e^2}{2m_e^2}\boldsymbol{s}_j\cdot\frac{\partial\boldsymbol{A}}{\partial t}\times\boldsymbol{A}. \tag{1.36}$$

The first of these terms gives rise to charge (Thomson) scattering, while the second gives rise to magnetic scattering through its dependence on $\boldsymbol{s}_j$. We see that the non-resonant magnetic cross section is smaller than the charge cross section by a factor $(\omega_{\boldsymbol{k}}/m_e)^2$, which ranges from 10^{-7} to 10^{-3} for the

x-ray energies used here (note that there are additional, smaller contributions to non-resonant magnetic scattering from the second-order terms treated in Sec. 1.2.3). I will explain in the next section how magnetic scattering can be enhanced by tuning the incident x-rays to an absorption edge of the sample. For now though, we complete our calculation for charge scattering

$$\sum_j \langle f; \boldsymbol{k}_f || \boldsymbol{A}|^2 | i; \boldsymbol{k}_i \rangle = \frac{4\pi}{V\sqrt{\omega_i \omega_f}} \left(\boldsymbol{\varepsilon}_i \cdot \boldsymbol{\varepsilon}_f^*\right) \sum_j \langle f | e^{i(\boldsymbol{q}\cdot\boldsymbol{r}_j - (\omega_i - \omega_f)t)} | i \rangle \,. \tag{1.37}$$

For elastic scattering with $\omega_i = \omega_f$, integrating over the energy gives a single-differential cross section

$$\begin{aligned} \frac{d\sigma}{d\Omega} &= r_0^2 \left|\boldsymbol{\varepsilon}_i \cdot \boldsymbol{\varepsilon}_f^*\right|^2 \left| \sum_j e^{i\boldsymbol{q}\cdot\boldsymbol{r}_j} \right|^2 \\ &= \frac{N r_0^2 (2\pi)^3}{V} \left|\boldsymbol{\varepsilon}_i \cdot \boldsymbol{\varepsilon}_f^*\right|^2 \sum_{\boldsymbol{G}_{hkl}} |F(\boldsymbol{G}_{hkl})|^2 \delta(\boldsymbol{q} - \boldsymbol{G}_{hkl}), \end{aligned} \tag{1.38}$$

where in the second step we have split the sum over electron positions, $\boldsymbol{r}_j$, into one over lattice sites, $\boldsymbol{R}_j$, and another over the atomic basis, $\boldsymbol{r}_\alpha$, and Fourier transformed the exponential in the former into a δ-function over reciprocal lattice points, $\boldsymbol{G}_{hkl}$. Note the similarity of this expression with the coherent nuclear neutron cross section in Eq. (1.28), with the Bragg peak intensity now given by the x-ray structure factor, $F(\boldsymbol{G}_{hkl}) = \sum_\alpha f_\alpha(\boldsymbol{G}_{hkl}) e^{i\boldsymbol{G}_{hkl}\cdot\boldsymbol{r}_\alpha}$, in which the form factor, f_α, is the Fourier transform of the local charge density.

A derivation of the non-resonant inelastic x-ray scattering (IXS) cross section is more involved, and depends on the type of excitation under investigation. The IXS measurements in this thesis are focussed on phonons, so we will limit our discussion to the phonon cross section here. The derivation begins with the introduction a time-dependence to the atomic positions in Eq. (1.37). Oscillations around the equilibrium positions, $\boldsymbol{r}_i$, can be expanded as a series of harmonic modes, each representing a different phonon. The dominant inelastic channel is that involving single-phonon processes, with

a differential cross section [20]

$$\frac{d^2\sigma}{d\Omega d\omega} = \frac{k_f}{k_i} r_0^2 \left|\boldsymbol{\varepsilon}_i \cdot \boldsymbol{\varepsilon}_f^*\right|^2 S(\boldsymbol{q},\omega). \tag{1.39}$$

In order to make contact with the analysis in Chapter 4, we have introduced here the dynamic structure factor

$$S(\boldsymbol{q},\omega) = N \sum_{\tilde{\boldsymbol{q}},j} |F_j(\boldsymbol{q})|^2 \delta(\boldsymbol{q}-\tilde{\boldsymbol{q}})[\langle n_{\tilde{\boldsymbol{q}},j}+1\rangle \delta(\omega-\omega_{\tilde{\boldsymbol{q}},j}) + \langle n_{\tilde{\boldsymbol{q}},j}\rangle \delta(\omega+\omega_{\tilde{\boldsymbol{q}},j})], \tag{1.40}$$

where $n_{\tilde{\boldsymbol{q}},j}$ is the number of phonons at reduced momentum $\tilde{\boldsymbol{q}}$ in the first Brillouin zone, with mode index j and energy $\omega_{\tilde{\boldsymbol{q}},j}$. The term with occupation factor $\langle n_{\tilde{\boldsymbol{q}},j}+1\rangle = \left(1-e^{-\omega_{\tilde{\boldsymbol{q}},j}/T}\right)^{-1}$ arises from the creation of a phonon, and the term with occupation factor $\langle n_{\tilde{\boldsymbol{q}},j}\rangle = \left(e^{\omega_{\tilde{\boldsymbol{q}},j}/T}-1\right)^{-1}$ arises from the annihilation of a phonon. The structure factor now depends on the Debye-Waller factor, atomic masses m_α, and phonon polarisation vector $\boldsymbol{e}_{\boldsymbol{q},j}$ as

$$F_j(\boldsymbol{q}) = \sum_\alpha \frac{f_\alpha(\boldsymbol{q})}{\sqrt{2m_\alpha \omega_{\boldsymbol{q},j}}} e^{-2q^2\langle u^2\rangle/3} \left(\boldsymbol{q}\cdot\boldsymbol{e}_{\boldsymbol{q},j}\right) e^{i\boldsymbol{q}\cdot\boldsymbol{r}_\alpha}. \tag{1.41}$$

The IXS measurements presented in Chapter 4 were conducted at beamline BL43LXU of the SPring-8 synchrotron [23]. BL43LXU uses a series of three insertion devices to produce a high flux of x-rays with energies tuneable from 14.4 to 25.7 keV. The bandwidth of the incident beam is reduced to the meV level by a backscattering Si monochromator, with the incident energy and flux, as well as the energy resolution, dependent on the chosen reflection. A series of mirrors focus the beam to a spot of 50 µm diameter on the sample. The scattered beam is energy-analysed by an array of backscattering analysers, each consisting of a diced grid of Si crystals mounted on a spherical substrate to increase the angular acceptance and therefore count rate. A 4×6 array of analysers, each with their own detector, allows the simultaneous measurement of multiple momentum transfers. Further details of the experimental setup used at BL43LXU are given in Sec. 4.2.1.

1.2.3 Resonant x-ray scattering

While non-resonant charge scattering could be sufficiently described by Fermi's Golden Rule to first-order, when the incident x-rays are tuned near an absorption edge of the scatterer the second-order term becomes significant. The second-order differential cross section for resonant scattering is given by

$$\frac{d^2\sigma}{d\Omega d\omega} = \left(\frac{Vk_f}{2\pi}\right)^2 \left|\sum_n \frac{\langle f;\boldsymbol{k}_f|V|n\rangle\,\langle n|V|i;\boldsymbol{k}_i\rangle}{\omega_i + E_i - E_n}\right|^2 \delta(\omega_i - \omega_f - E_i + E_f), \quad (1.42)$$

where the sum runs over all possible intermediate states, $|n\rangle$, of the scatterer. Going back to our expression for the interaction Hamiltonian in Eq. (1.35), the leading order contributions are now those that are linear in $\boldsymbol{A}$, namely

$$H' = \sum_j \frac{e}{m_e}\boldsymbol{p}_j \cdot \boldsymbol{A} - \frac{e}{m_e}\boldsymbol{s}_j \cdot \nabla \times \boldsymbol{A} + \frac{e}{2m_e^2}\boldsymbol{s}_j \cdot \frac{\partial \boldsymbol{A}}{\partial t} \times \boldsymbol{p}_j, \quad (1.43)$$

where we have chosen the Coulomb gauge, $\nabla \cdot \boldsymbol{A} = 0$, so that $\boldsymbol{A} \cdot \boldsymbol{p}_j = \boldsymbol{p}_j \cdot \boldsymbol{A}$. The third term here actually contributes to *non-resonant* magnetic scattering, and along with the second term can be shown to give a negligible matrix element near resonance [21]. Going forward we will therefore retain only the first term. In order to prevent an unphysical divergence of the cross section on resonance ($\omega_i = E_n - E_i$) we introduce a finite lifetime of $1/\Gamma_n$ for the intermediate states. Expanding out the vector potential then gives the so-called Kramers-Heisenberg resonant cross section

$$\frac{d^2\sigma}{d\Omega d\omega} = \frac{\omega_f}{\omega_i} r_0^2 \left|\sum_{n,j,k} \frac{\langle f|\left(\boldsymbol{\varepsilon}_f^* \cdot \boldsymbol{p}_j\right) e^{-i\boldsymbol{k}_f\cdot\boldsymbol{r}_j}|n\rangle\,\langle n|\left(\boldsymbol{\varepsilon}_i \cdot \boldsymbol{p}_k\right) e^{i\boldsymbol{k}_i\cdot\boldsymbol{r}_k}|i\rangle}{\omega_i + E_i - E_n + i\Gamma_n}\right|^2 \times \delta(\omega_i - \omega_f - E_i + E_f). \quad (1.44)$$

Inside the core region of the excited atom we usually have $\boldsymbol{k}\cdot\boldsymbol{r}_j \ll 1$ such that we can take the dipole approximation, $e^{i\boldsymbol{k}\cdot\boldsymbol{r}_j} \approx 1$. This simplifies the matrix

elements

$$\begin{aligned}\sum_j \langle n|\left(\boldsymbol{\varepsilon}\cdot\boldsymbol{p}_j\right)e^{i\boldsymbol{k}\cdot\boldsymbol{r}_j}|i\rangle &\approx \sum_j \boldsymbol{\varepsilon}\cdot\langle n|\boldsymbol{p}_j|i\rangle \\ &= im_e\sum_j \boldsymbol{\varepsilon}\cdot\langle n|[H_0,\boldsymbol{r}_j]|i\rangle \\ &= im_e(E_n-E_i)\sum_j \boldsymbol{\varepsilon}\cdot\langle n|\boldsymbol{r}_j|i\rangle \\ &= im_e\omega_i\langle n|\sum_j \boldsymbol{\varepsilon}\cdot\boldsymbol{r}_j|i\rangle\,,\end{aligned} \tag{1.45}$$

where in the second step we have used $\boldsymbol{p}_j = m_e\frac{d\boldsymbol{r}_j}{dt} = im_e[H_0,\boldsymbol{r}_j]$ with H_0 the Hamiltonian of the scatterer [i.e. the terms in Eq. (1.35) that do not depend on the vector potential]. We can then recognise the dipole operator $\mathcal{D} = \sum_j \boldsymbol{\varepsilon}\cdot\boldsymbol{r}_j$, with which the Kramers-Heisenberg cross section can be written

$$\frac{d^2\sigma}{d\Omega d\omega} = \omega_f^3\omega_i m_e^4 r_0^2\left|\sum_n \frac{\langle f|\mathcal{D}^\dagger|n\rangle\langle n|\mathcal{D}|i\rangle}{\omega_i+E_i-E_n+i\Gamma_n}\right|^2\delta(\omega_i-\omega_f-E_i+E_f). \tag{1.46}$$

The Kramers-Heisenberg cross section describes a two-step process. First, the incident photon excites a core-level electron into an empty orbital, leaving a core hole in the intermediate state. Each absorption edge corresponds to a different pair of core and excited orbitals of a specific element (for example, the O K edge used in Chapter 4 involves a $1s \rightarrow 2p$ excitation, while the Ir L edges involve $2p \rightarrow 5d$ excitations), endowing resonant scattering with element and orbital selectivity. Following the initial excitation, there are multiple possibilities for the second step. The simplest occurs in resonant elastic x-ray scattering (REXS), where the same electron relaxes to fill the core hole, emitting a photon of the same energy ($\omega_f = \omega_i$) and returning the scatterer to its initial state ($|f\rangle = |i\rangle$). Resonant inelastic x-ray scattering (RIXS) instead involves the emission of a photon of reduced energy ($\omega_f < \omega_I$) due to the creation of an excitation in the final state ($|f\rangle \neq |i\rangle$). This can be an electronic excitation, such as that illustrated in Fig. 1.5, where the core hole is filled by an electron from a different orbital than that which the initial electron was

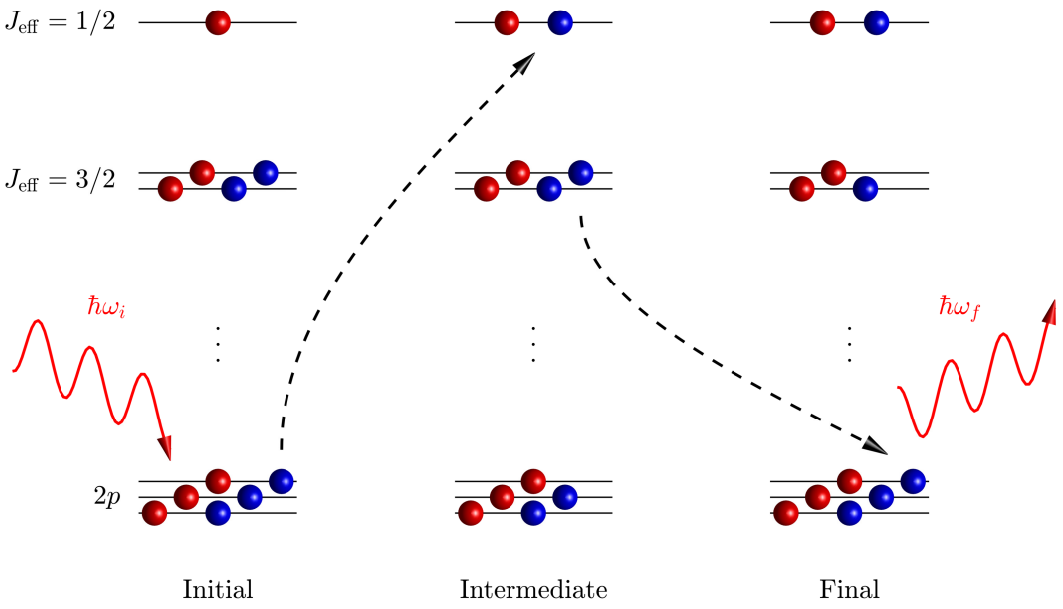

Figure 1.5: Illustration of the two-step RIXS process at the Ir L edge of Sr_2IrO_4, involving the creation of an electronic excitation. An incident photon of frequency ω_i excites an electron from a $2p$ core level ($2p_{\frac{1}{2}}$ for the L_2 edge and $2p_{\frac{3}{2}}$ for the L_3 edge) to the half-filled $J_{\text{eff}} = 1/2$ level. Another electron then decays from the $J_{\text{eff}} = 3/2$ level to fill the core hole, emitting a photon of frequency ω_f. The net effect is a promotion of an electron from the $J_{\text{eff}} = 3/2$ to $1/2$ levels.

excited into. Other possibilities involve the creation of a magnetic excitation through a SOC-induced spin flip, or the creation of phonons due to the altered charge density in the intermediate state.

The variety of processes captured by the Kramers-Heisenberg cross section make its evaluation highly complex in general. In Chapter 3, I give a window into this complexity for the case of phonon excitations in RIXS. Often, however, a calculation of the full cross section is not needed. Much can be understood about a RIXS spectrum from the energies of the excitations, and how they vary with momentum transfer, without worrying about their intensities. Similarly, one is usually more interested in the angular and polarisation dependence of the REXS cross section, rather than its absolute magnitude. Hill and McMorrow derived a general expression for the REXS dipole single-

differential cross section [24]

$$\frac{d\sigma}{d\Omega} \propto \left| \sum_j (\boldsymbol{\varepsilon}_f \cdot \boldsymbol{\varepsilon}_i) F_0 - i\hat{\boldsymbol{z}}_j \cdot (\boldsymbol{\varepsilon}_f \times \boldsymbol{\varepsilon}_i) F_1 + (\boldsymbol{\varepsilon}_f \cdot \hat{\boldsymbol{z}}_j)(\boldsymbol{\varepsilon}_i \cdot \hat{\boldsymbol{z}}_j) F_2 \right|^2 , \qquad (1.47)$$

where the strength of the resonance is determined by the factors F_i (for which a full evaluation of the Kramers-Heisenberg equation is required) and $\hat{\boldsymbol{z}}_j$ are the directions of the magnetic moments for each site j. The first term in Eq. (1.47) has no dependence on $\hat{\boldsymbol{z}}_j$ and contributes to the charge Bragg peaks, with the same polarisation dependence as non-resonant Thomson scattering. The second term is linear in $\hat{\boldsymbol{z}}_j$ and gives rise to resonant magnetic scattering, in which the polarisation of the scattered x-rays is rotated compared to the incident beam. The third term is quadratic in $\hat{\boldsymbol{z}}_j$ and produces satellite peaks in incommensurate magnets. Equation (1.47) shows that the directions of the moments can be determined by varying the projections of the incident and scattered polarisations onto them, as is done in Chapter 2. One point that requires clarification is the origin of the $\hat{\boldsymbol{z}}_j$ in Eq. (1.47) when the dipole operators in the Kramers-Heisenberg cross section have no dependence on spin or orbital angular momentum. The sensitivity to magnetism arises from the combination of spin conservation in x-ray absorption and the Pauli exclusion principle, which result in core electrons in the minority spin state being preferentially excited in the first step of the RIXS process.

The REXS measurements presented in Chapter 2 were conducted at beamline I16 of the Diamond Light Source [25]. A 2 m undulator provides x-rays with energies continuously tuneable between 2.7 and 25 keV, encompassing the K edges of elements from Cl to Pd, the L edges of all common elements above Mo, and the M edges of all common elements above Hf. The bandwidth of the incident beam is reduced to ∼1.5 eV by a channel-cut Si(111) monochromator, and focussed to a size of 20×200 µm at the sample. The sample stage and detectors sit on a 6-circle Kappa diffractometer, which allows for independent rotation of the scattering angle, 2Θ, rocking angle, θ, azimuthal angle,

Ψ, and rotation around the incident beam, χ, over wide ranges (with some of these made up of coupled rotations of multiple physical motors). A benefit of the Kappa diffractometer is the large space for different sample environments, including the closed-cycle cryostat with base temperature 6 K. The detector arm houses a number of detectors, including a Pilatus 100K area detector that allows a full 3D reciprocal space map to be reconstructed from a single rocking scan, and various point detectors that can be used with analyser crystals to measure different polarisation components of the scattered beam. Further details of the experimental setup used at I16 are given in Sec. 2.2.1.

The RIXS measurements presented in Chapters 3 and 4 were conducted at beamline I21 of the Diamond Light Source [26]. I21 uses a 5 m helical undulator to produce x-rays with either linear horizontal or vertical polarisation and energies from 250 to 1500 eV, encompassing the K edge of elements from C to Mg, the L edges of elements from Cl to Se, and the M edges of elements from Br to Tm. Crystals cannot be used as monochromators at these soft x-ray energies, so instead divergent variable-line-spacing gratings are used. A choice of three different gratings allows the energy resolution to be balanced against flux. Mirrors are used to focus the beam to 2.5×40 µm at the sample. To minimise absorption of the soft x-rays, all of the optics are kept in ultra-high vacuum. This includes the sample chamber, which contains a sample manipulator with x–y–z translations and θ–Ψ–χ rotations, cooled with liquid He to a base temperature of 10 K. Collection mirrors placed close to the sample capture as many scattered photons as possible, increasing the throughput at the expense of momentum resolution. The scattered photons are then energy-analysed by a choice of two spherical variable-line-spacing gratings, each optimised for different incident energy ranges, before being detected by a 2D charge coupled device at the end of a 15 m detector arm. While the detector arm can rotate through 150° on air bearings, for the measurements described in this thesis we used a fixed scattering angle. Further details of the experimental setup used at I21 are given in Sec. 3.3.1 and 4.3.1.

Chapter 2

Magneto-elastic coupling in a $4d$ polar metal

The 4d ruthenate $Ca_3Ru_2O_7$ hosts a variety of intriguing features, from correlated itinerant electrons in a polar lattice, to spin-orbit-coupled antiferromagnetism that undergoes a temperature-driven spin-reorientation transition (SRT). In this chapter, I describe a series of neutron and resonant x-ray experiments that uncover previously unknown incommensurate order at the SRT, and identify it as a magnetic cycloid that evolves with temperature to mediate the reorientation of the spins. Measurements under applied magnetic field offer a new interpretation of the so-called "metamagnetic texture" in $Ca_3Ru_2O_7$, unifying it with incommensurate order observed under chemical doping. Finally, I show how the coupled degrees of freedom inherent to 4d oxides render the SRT sensitive to uniaxial pressure, shedding light on the microscopic mechanism behind it.

2.1 Introduction

$4d$ oxides occupy an interesting position among quantum materials, where an intermediate SOC strength is of similar magnitude to other energy scales such as electronic correlations, crystal fields, and Hund's coupling. The subtle interplay between these interactions generates myriad ground states, as exemplified by the layered perovskite ruthenates of the Ruddlesden-Popper series $A_{n+1}Ru_nO_{3n+1}$. Of the monolayer ($n = 1$) variants, Sr_2RuO_4 is a Fermi liquid that found fame as the first non-cuprate perovskite to display unconventional

superconductivity [27]. Ca_2RuO_4, by contrast, is a fragile antiferromagnetic Mott insulator [28] that can be driven through an insulator-metal transition by temperature [28], doping [29], hydrostatic pressure [30], and anisotropic strain [31]. The bilayer ($n = 2$) variants are similarly interesting. $Sr_3Ru_2O_7$, for instance, is a strange metal [32] that shows metamagnetic quantum criticality under applied magnetic field [33].

In this chapter, I will focus on $Ca_3Ru_2O_7$ – an antiferromagnetic metal and the only member of the Ruddlesden-Popper ruthenates to host polar lattice distortions [34, 35, 36]. After surveying the pertinent properties of $Ca_3Ru_2O_7$, I will describe the results of neutron and x-ray scattering studies of the magnetic structure around the intriguing SRT. These reveal an incommensurate magnetic cycloid that exists over a small temperature window, and whose envelope evolves to mediate the transition between collinear phases. Symmetry analysis shows that the cycloid arises from a uniform Dzyaloshinskii-Moriya interaction (DMI) allowed by the polar structure of $Ca_3Ru_2O_7$, which competes with easy-axis anisotropies. The discovery of cycloidal order at zero field in the parent compound has important implications for incommensurate structures previously seen under doping and applied magnetic field. The final part of the chapter reports neutron and x-ray measurements of the magnetic order under anisotropic strain, which guides the formation of a theoretical model to understand the SRT.

2.1.1 Polar distortions and the Dzyaloshinskii-Moriya interaction

Polar distortions of the ions in a crystal break the inversion symmetry of the lattice, and allow the formation of anisotropic interactions between magnetic moments. The most important of these interactions is the DMI, which originates from SOC [37] and takes the form $\boldsymbol{D}_{ij} \cdot (\boldsymbol{S}_i \times \boldsymbol{S}_j)$. For superexchange between two magnetic ions with spins $\boldsymbol{S}_{i,j}$ and displacement vectors $\boldsymbol{r}_{i,j}$ to the shared ligand, the DMI vector $\boldsymbol{D}_{ij}$ is directed along $\boldsymbol{r}_i \times \boldsymbol{r}_j$. A staggered DMI can exist for locally non-centrosymmetric exchange pathways

in crystals with global inversion symmetry, where it can compete with symmetric Heisenberg exchange to produce a canting of the moments away from their (anti)ferromagnetic arrangement. Indeed, the DMI was first introduced by Dzyaloshinskii to explain the weak ferromagnetism seen in α-Fe_2O_3 due to spin canting [38]. In globally non-centrosymmetric materials, a uniform DMI is allowed, which can compete with Heisenberg exchange to give rise to complex helical and spiral magnetic orderings.

In insulators, polar distortions can also generate an electric polarisation that is switchable by external electric fields – a property termed ferroelectricity in analogy with ferromagnetism. Magnetoelectric multiferroics combine both ferroelectricity and (anti)ferromagnetism, allowing electric control of magnetic degrees of freedom and *vice versa* [39, 40]. Generally, centrosymmetry-breaking structural transitions occur at high temperature ($\sim$1000 K) due to the large energies needed to deform the lattice, while magnetic order sets in at lower temperatures dependent on the exchange couplings. $BiFeO_3$ is the paradigmatic example of such a type-I multiferroic [41], with a ferroelectric transition at $T_C = 1100$ K and a Néel transition at $T_N = 643$ K [42]. In type-II (or magnetically-driven) multiferroics, by contrast, the electric polarisation is directly induced by a magnetic ordering which beaks inversion symmetry, via the "inverse Dzyaloshinskii-Moriya effect". In this case the magnetic and ferroelectric transitions occur at the same temperature, and the electric and magnetic degrees of freedom are strongly coupled [43]. In frustrated magnets such as $TbMnO_3$, for instance, competing magnetic interactions generate a spiral magnetic order that breaks inversion symmetry and induces ferroelectricity at 28 K [44].

The multiferroics discussed above are all insulating, and it was long thought that any polar distortions in a metal would be screened by the mobile conduction electrons. Following a theoretical prediction by Anderson and Blount [45], however, a number of polar metals have been discovered, including $LiOsO_3$ [46] and epitaxially-stabilised $NdNiO_3$ [47]. A key feature of polar

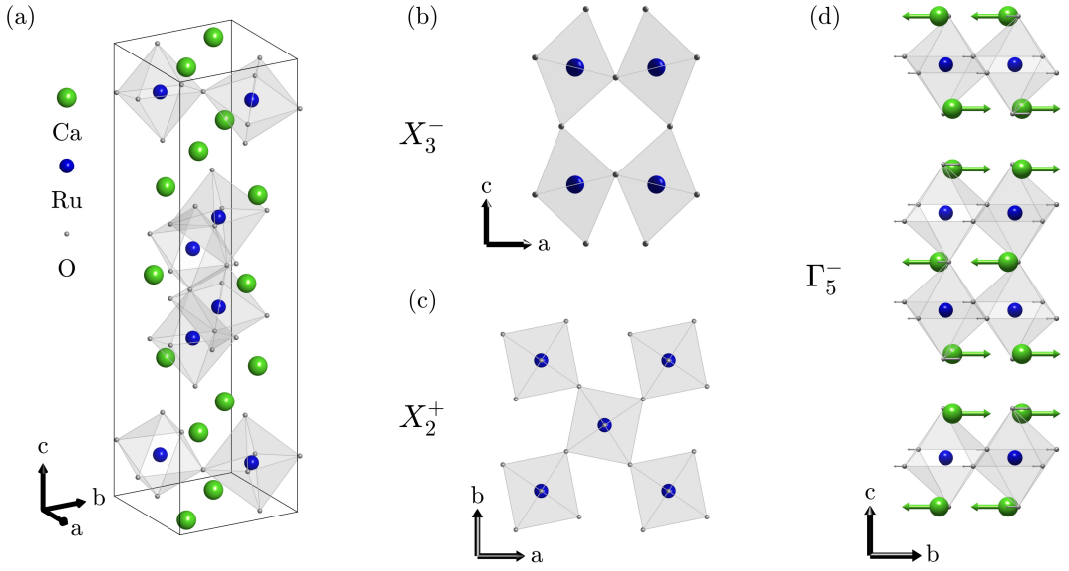

Figure 2.1: (a) Crystal structure of $Ca_3Ru_2O_7$, showing bilayers of RuO_6 octahedra separated by Ca ions. (b) Cartoon of the X_3^- mode which alternately tilts the octahedra around the ***b*** axis (Ca ions not shown for clarity). (c) Cartoon of the X_2^+ mode which rotates the octahedra around the ***c*** axis (Ca ions not shown for clarity). (c) Cartoon of the Γ_5^- mode involving polar displacements of the Ca and O ions along the ***b*** axis (displacement vectors have been magnified for clarity).

metals is that the electronic states near the Fermi level do not derive from the ions that undergo polar displacements.

The bilayer ruthenate $Ca_3Ru_2O_7$ is a particularly rare example of a material that combines metallicity, a polar crystal structure and long-range magnetic order [34]. $Ca_3Ru_2O_7$ crystallises in the orthorhombic structure shown in Fig. 2.1(a), with polar space group $Bb2_1m$ (36) [35]. The structure consists of bilayers of corner-sharing RuO_6 octahedra separated by sheets of Ca ions. Due to the large size of Ca relative to Ru, the perovskite layers are distorted by both tilts and rotations of the octahedra [of pattern $(a-, a-, c+)$ in Glazer notation]. We can analyse these distortions by considering the symmetry-adapted modes of a high-symmetry parent structure with space group $I4/mmm$ [48]. Tilts of the octahedra around the crystallographic ***b*** axis, shown in Fig. 2.1(b), transform according to the X_3^- irreducible representation (irrep), while rotations around the ***c*** axis, shown in Fig. 2.1(c), transform according to the X_2^+ irrep. Neither of these modes are stable on their own, but a combination of

both lowers the energy of the lattice and breaks inversion symmetry. This then allows polar displacements of the Ca and O ions, shown in Fig. 2.1(d), which transform according to the Γ_5^- irrep.

Despite being metallic, $Ca_3Ru_2O_7$ displays analogous properties to the insulating ferroelectrics described above. Instead of a net electric polarisation that can be switched with applied electric field, it hosts polar domains that can be switched with applied anisotropic strain [48]. The combination of broken inversion symmetry and the sizeable SOC of the Ru ions also generates a uniform DMI, which, as I will show later in the chapter, leads to rich magnetic behaviour.

2.1.2 Spin-reorientation transition

An interesting feature of α-Fe_2O_3 studied by Dzyaloshinskii is a sudden loss of its weak ferromagnetic moment on cooling below the Morin transition [49]. In one of the first neutron scattering experiments on an antiferromagnetic material, Shull *et al.* showed that above $T_M = 250\,\mathrm{K}$, the spins are oriented in the basal plane where they can be canted by the DMI [50]. Below T_M, however, they reorient along the $\boldsymbol{c}$ axis, where, by symmetry, the DMI is zero and no canting can occur.

A similar, thermally-driven SRT occurs in $Ca_3Ru_2O_7$. Just below the Néel temperature, $T_N \approx 56\,\mathrm{K}$, the magnetic structure consists of collinear moments pointing along $\boldsymbol{a}$, aligned ferromagnetically within each bilayer and antiferromagnetically between the bilayers [35]. This has been labelled the $\mathrm{AFM_a}$ phase, and is depicted in Fig. 2.2(d). On further cooling through $T_S \approx 48\,\mathrm{K}$, anomalies are visible in both the resistivity [Fig. 2.2(b)] [51] and magnetisation [Fig. 2.2(c)] [52]. Using REXS, Bohnenbuck *et al.* showed that at T_S, the moments globally rotate to point along the $\boldsymbol{b}$ axis [53], producing the $\mathrm{AFM_b}$ phase shown in Fig. 2.2(a).

The sharp increase in resistivity at T_S gives an indication of the coupling between the magnetism and fermiology at the SRT. The jump in resistivity is caused by a gapping of large parts of the Fermi surface [54, 55, 56], leaving

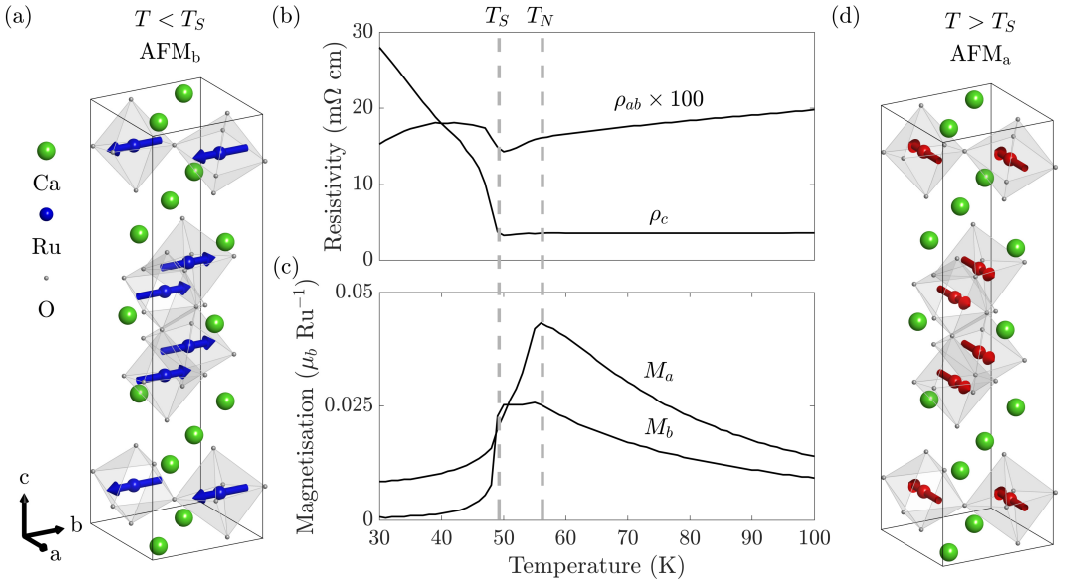

Figure 2.2: (a) Magnetic structure of $Ca_3Ru_2O_7$ below T_S with collinear spins pointing along the $\boldsymbol{b}$ axis. (b) Temperature dependence of the in-plane and out-of-plane resistivity, ρ_{ab} and ρ_c respectively, from Ref. [51]. (c) Temperature dependence of the magnetisation along the $\boldsymbol{a}$ and $\boldsymbol{b}$ axes, M_a and M_b respectively, with an applied field of 0.5 T, from Ref. [52]. (d) Magnetic structure of $Ca_3Ru_2O_7$ for $T_S < T < T_N$ with spins pointing along the $\boldsymbol{a}$ axis.

very small electron and hole pockets at the Brillouin zone boundaries. Simultaneously, the unit cell is found to contract along the c axis while expanding along the a and b axes [35], although there is no change in the crystal symmetry. This electron-lattice coupling will be employed later to drive the SRT with anisotropic strain.

2.2 Cycloidal order mediating the spin-reorientation transition

In this section, I report the formation of incommensurate order around the SRT in $Ca_3Ru_2O_7$, driven by competing magnetic interactions in the presence of structurally-broken inversion symmetry. Exploiting the complementarity of neutron and resonant x-ray scattering, I show this order to be a magnetic cycloid that evolves continuously between the collinear end states over a remarkably small temperature range to mediate the SRT. Symmetry analysis

shows that the cycloid is stabilised by a uniform DMI activated by the polar lattice distortions, which competes with easy-axis anisotropies. I go on to investigate the response of the cycloid to applied magnetic field, under which higher harmonic modulations of the fundamental order appear to be generated. This necessitates a reinterpretation of an incommensurate structure previously observed under field [57], unifying it with the magnetic response to doping [58, 59, 60].

The work presented in this section has been published as C. D. Dashwood *et al.*, Phys. Rev. B **102**, 180410 (2020) [61]. The $Ca_3Ru_2O_7$ single crystals were grown by Robin Perry, and characterised by me and Robin, with assistance from Daniel Nye and Gavin Stenning. The neutron measurements were performed by me, Larissa Veiga, Quentin Faure, Robin Perry and Roger Johnson, with Pascal Manuel, Dmitry Khalyavin and Fabio Orlandi as local contacts. The REXS measurements were performed by me, Larissa Veiga, Quentin Faure, Robin Perry and Roger Johnson, with Dan Porter as local contact. Data analysis was performed by me and Roger Johnson, and overseen by Des McMorrow. The symmetry analysis was performed by Roger Johnson.

2.2.1 Experimental details

Single crystals of $Ca_3Ru_2O_7$ were grown using the floating zone method in a Crystal System Corporation FZ-T-10000-H-VI-VPO-I-HR-PC mirror furnace. Their stoichiometry was confirmed with an Oxford Instruments energy-dispersive x-ray spectrometer on a JEOL JEM-2100 electron microscope, yielding a Ca:Ru ratio of 3:1.97±0.06. The crystalline quality and phase-purity were checked using a Rigaku XtaLAB Synergy-S single crystal x-ray diffractometer. The bulk electronic behaviour was confirmed with standard four-probe resistivity measurements using a Quantum Design PPMS [see Fig. 2.3(b)]. Twin domains were identified with polarised light microscopy, and single-domain pieces were cut from larger crystals using a wire saw. Measurements were performed on multiple crystals from different growth batches with consistent results. The neutron and x-ray data presented below are all from the same

crystal, which was aligned by Laue diffraction.

Neutron scattering measurements were performed at the WISH instrument of the ISIS Neutron and Muon Source. The sample was mounted on the end of an aluminium pin with aluminium tape. For the maps shown in Fig. 2.3(a), the sample was mounted in a cryostat such that the $\boldsymbol{a}$ axis lies along the vertical ^{3}He detector banks. For the data in Figs. 2.3(c) and 2.7, the sample was mounted in a 10 T cryomagnet with the $\boldsymbol{b}$ axis vertical, along the field direction. In both cases, the sample was rotated around the vertical axis such that the peak being measured was located close to forward transmission scattering, where the flux at the relevant d spacing (around 19.5 Å) is highest. Data analysis was performed with the MANTID software package [62]. All data are normalised to the cumulative current and a beam monitor. The intensities were obtained by diffraction-focussing a small area on the detector around the peak, and then integrating the resulting time-of-flight spectra.

REXS measurements were performed at beamline I16 of the Diamond Light Source. The horizontally (σ) polarised incident beam was tuned to the Ru L_2 edge (2.967 keV). The scattered intensity was measured using an in-vacuum Pilatus 100K area detector in ultrahigh gain mode. An extended in-vacuum beam pipe was used to reduce air absorption of the scattered photons. The diffractometer was operated in fixed-azimuth mode with a vertical reflection scattering geometry, as shown in Fig. 2.4(a). The sample was mounted to a copper holder with GE varnish to ensure good thermal contact and no thermally-induced strain, and was cooled with an Advanced Research System closed-cycle cryocooler. Data analysis was carried out using the PY16 program written by Dan Porter [63]. All data are normalised to the ring current and corrected for self-absorption (this has minimal effect on the azimuthal dependences as the beam-footprint is nearly constant so close to the specular condition). Peak intensities are obtained by summing over a region of interest on the area detector, and then fitting the resulting rocking curves with pseudo-Voigt profiles plus a constant background. This provides full three-dimensional

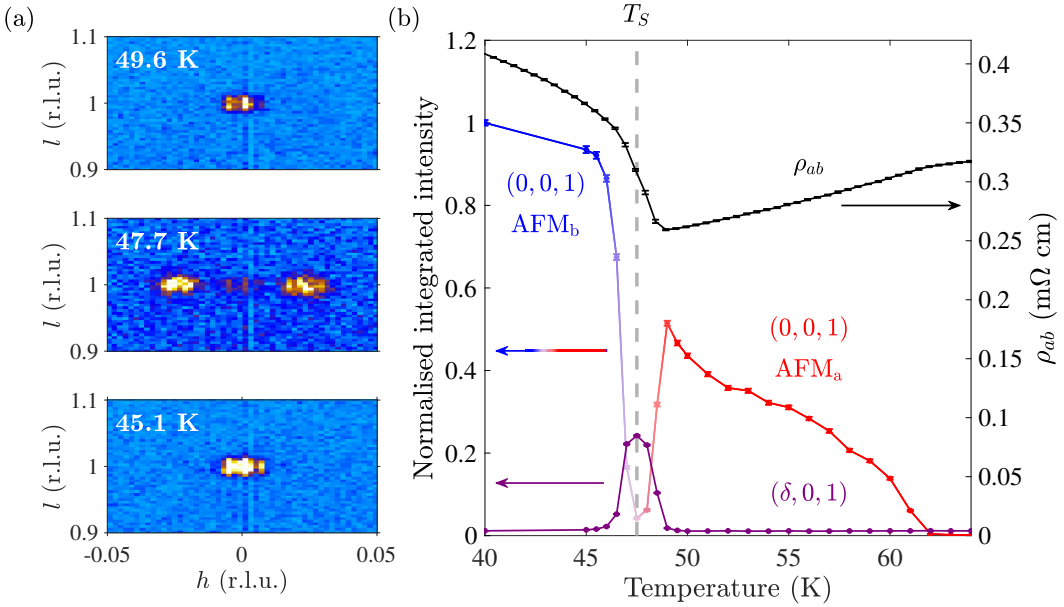

Figure 2.3: (a) Reciprocal space maps showing incommensurate satellite peaks $(\pm\delta, 0, 1)$ around the $(0, 0, 1)$ magnetic peak over a narrow temperature range around $T_S \approx 48\,\mathrm{K}$. (b) Integrated intensity of the $(0, 0, 1)$ (blue to red, with blue representing the $\mathrm{AFM_b}$ and red the $\mathrm{AFM_a}$ phase) and $(+\delta, 0, 1)$ (purple) peaks as a function of temperature, plotted alongside the in-plane resistivity ρ_{ab} (black).

integration of the peaks with negligible background contribution.

2.2.2 Incommensurate order at the spin-reorientation transition

We will first examine the results of the neutron scattering experiments. The $\mathrm{AFM_a}$ and $\mathrm{AFM_b}$ structures both have propagation vector $(0, 0, 1)$, so produce peaks at the structurally-forbidden $\boldsymbol{q} = (0, 0, 2n + 1)$ positions with $n \in \mathbb{Z}$. Figure 2.3(a) shows reciprocal-space maps at temperatures around T_S. Well above and below T_S (top and bottom panels) a single peak can be seen at $(0, 0, 1)$, confirming the presence of the $\mathrm{AFM_a}$ and $\mathrm{AFM_b}$ structures at these temperatures. As unpolarised neutron scattering is sensitive to the component of the moment perpendicular to $\boldsymbol{q}$ (see Sec. 1.2.1), we are measuring the full moment in both phases. The lower intensity in the top panel is therefore indicative of a smaller moment in the $\mathrm{AFM_a}$ phase, consistent with previous reports [64]. Strikingly, close to T_S (middle panel), the central peak is strongly

suppressed and satellites can be seen at incommensurate positions $(\pm\delta, 0, 1)$ with $\delta \approx 0.023$ reciprocal lattice units (r.l.u.). Satellite peaks closely spaced around a commensurate position are indicative of a long-range modulation of the nuclear and/or magnetic structure, such as charge/spin density wave phases [65, 33] or spiral magnetic structures [66, 67]. The comparable width of the satellites to the commensurate peak indicates a similarly long correlation length to the AFM_a and AFM_b structures.

Figure 2.3(b) shows the integrated intensity of the $(0, 0, 1)$ and $(\delta, 0, 1)$ peaks as a function of temperature. On cooling below T_N, the $(0, 0, 1)$ peak follows a power-law dependence into the AFM_a phase. Around 50 K there appears to be a second upturn, before the intensity rapidly falls and the $(\delta, 0, 1)$ peak appears. The satellite peaks survive for less than 3 K before the $(0, 0, 1)$ peak recovers and reaches its highest intensity in the AFM_b phase. The clear transfer of intensity been the commensurate and satellite peaks suggests a common magnetic origin.

Plotted alongside the peak intensities in Fig. 2.3(b) is the in-plane resistivity, ρ_{ab}. We already know that SRT coincides with an uptick in ρ_{ab}, but we can also see from Fig. 2.3(b) that the boundaries of the incommensurate region correspond to changes of slope in ρ_{ab}. This reveals an intimate connection between the electronic and magnetic behaviour at T_S, which will be explored in Sec. 2.3.4.

2.2.3 An evolving magnetic cycloid revealed by resonant elastic x-ray scattering

Having established the existence of a bulk incommensurate phase in the vicinity of the SRT, we now turn to resonant x-ray scattering to unravel its nature. In contrast to neutron scattering, resonant x-ray scattering in the $\sigma - \pi'$ polarisation channel is sensitive to the component of the moment parallel to $\boldsymbol{k_f}$ (see Sec. 1.2.3). More information about the magnetic structure can therefore be obtained by rotating the sample through an azimuthal angle Ψ in order to vary the component projected along $\boldsymbol{k_f}$. Azimuthal dependences of the magnetic

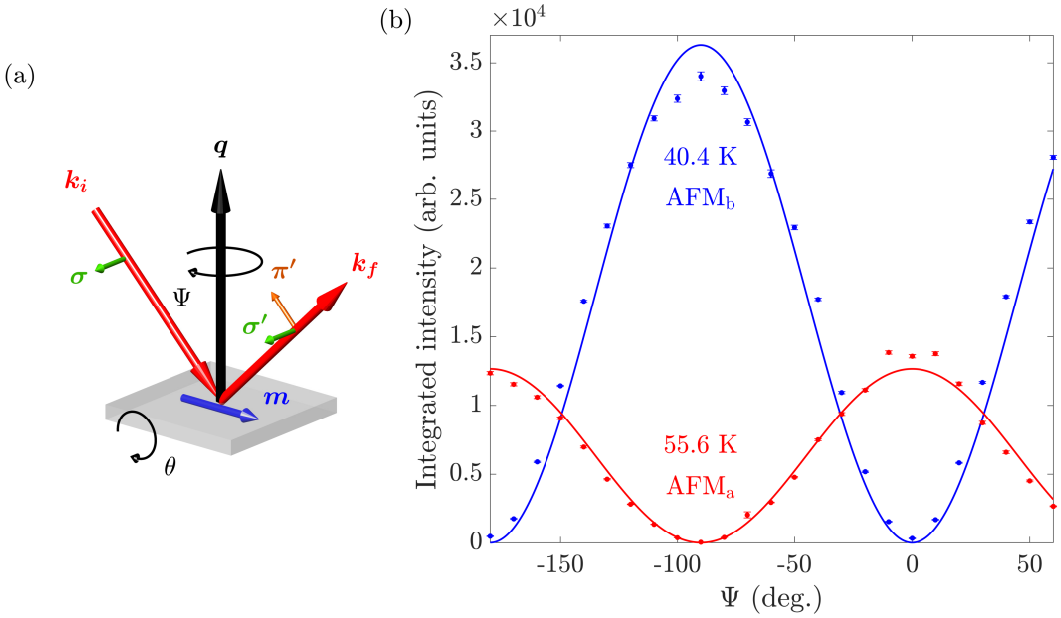

Figure 2.4: (a) Experimental REXS geometry, showing incident x-rays with wavevector $\boldsymbol{k_i}$ (red arrow) scattering from a magnetic moment $\boldsymbol{m}$ (blue arrow) to wavevector $\boldsymbol{k_f}$. The incident x-rays are polarised horizontally, normal to the scattering plane (σ polarised, green arrow) and the scattered x-rays are polarised either in the scattering plane (π', orange) or normal it (σ', green). The azimuth Ψ is varied by rotating the sample around the scattering vector $\boldsymbol{q} = \boldsymbol{k_f} - \boldsymbol{k_i}$ (black arrow). (b) Azimuthal scans of the $(0, 0, 5)$ peak above (55.6 K, red) and below (40.4 K, blue) T_S, evidencing the SRT.

$(0, 0, 5)$ peak at two temperatures are shown in Fig. 2.4(b). For basal-plane collinear structures, calculation of the resonant cross section gives an intensity $\propto \cos^2(\Psi + \phi)$ [solid lines in Fig. 2.4(b)] where ϕ is the rotation of the moments away from the $\boldsymbol{a}$ axis [53]. At 55.6 K it can be seen that $\phi = 0°$, while at 40.4 K $\phi = 90°$. This 90° degree shift of the azimuthal dependences is clear evidence of the spin reorientation from $\boldsymbol{a}$ to $\boldsymbol{b}$.

The upper and lower panels in Fig. 2.5(a) show h scans through $(0, 0, 5)$ as a function of temperature for two azimuths, sensitive to the $\boldsymbol{b}$ ($\Psi = -90°$) and $\boldsymbol{a}$ ($\Psi = -180°$) components of the moments respectively. Again, the spin reorientation is identified by the transfer of commensurate intensity between the azimuths. The satellite peaks that we saw with neutron scattering are also visible around the SRT, and intriguingly have subtle temperature dependences to their wavevectors and intensities. We now analyse these satellites in more

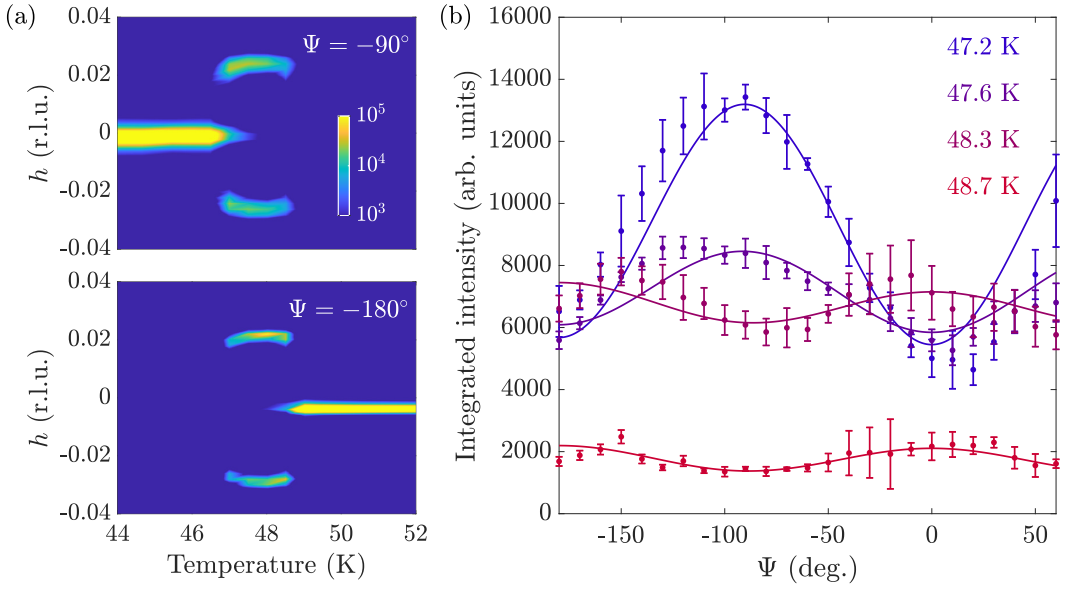

Figure 2.5: (a) h scans through $(0, 0, 5)$ as a function of temperature at $\Psi = -90°$ (top panel, sensitive to the component of the moment along $\boldsymbol{b}$) and $\Psi = -180°$ (lower panel, sensitive to the component along $\boldsymbol{a}$). The intensity is plotted on a log scale. (b) Azimuthal dependences of the $(-\delta, 0, 5)$ satellite at select temperatures. The solid lines are fits to the cycloidal model described in the text.

detail.

In order to determine the structure of the incommensurate phase we performed a detailed investigation of the azimuthal dependence of the satellites. Representative dependences are shown in Fig. 2.5(b). All of the dependences are sinusoidal, but show dramatic changes in peak-to-peak amplitude and phase, evidencing a remarkable evolution of the structure over a small temperature window. Unlike in the commensurate phases where the intensity goes to zero when $\boldsymbol{k_f}$ is perpendicular to $\boldsymbol{m}$, here we see a finite intensity at all Ψ. This is an indication of a non-collinear rotating structure, with a component of the moment always parallel to $\boldsymbol{k_f}$. We calculated the cross section for all possible modulated states using the MAGNETIX package [68] and found that an incommensurate cycloid (ICC) with moments rotating in the $\boldsymbol{a} - \boldsymbol{b}$ plane, maintaining the ferromagnetic coupling within bilayers and antiferromagnetic coupling between bilayers, is uniquely consistent with our data.

To understand the temperature evolution of the ICC structure, we devel-

oped a model in which the cycloid is decomposed into two spin-density wave components, $\pi/2$ out of phase, that in the commensurate limits are equivalent to the AFM_a and AFM_b structures. The only free parameters are the amplitudes of these components, M_a and M_b, which describe the elongation of the envelope of the cycloid along $\boldsymbol{a}$ and $\boldsymbol{b}$ respectively. We fit the azimuthal dependences using MagnetiX [solid lines in Fig. 2.5(b)] and found that this simple model provides a remarkably accurate description of the data at all temperatures. The fits can be intuitively understood by neglecting the small h component of the wavevector, which simplifies the dependence to $\propto (M_a \cos\Psi)^2 + (M_b \sin\Psi)^2$. It can then be seen that the peak-to-peak amplitude of the oscillations, $|M_a^2 - M_b^2|$, is directly related to the eccentricity of the cycloid, while the phase depends on whether M_a or M_b is larger.

The fitted amplitudes, including those obtained from fits to the commensurate dependences in Fig. 2.4(b), are shown in Fig. 2.6(a) (normalised by the overall moment size for clarity). In the commensurate phases only one of the components is present, as expected. In the ICC phase, by contrast, both amplitudes are finite and vary with temperature, crossing near the centre of the phase. This describes the magnetic structure shown schematically in Fig. 2.6(b). Above 50 K, the system is in the AFM_a phase with moments collinear along $\boldsymbol{a}$. On cooling into the ICC phase, the cycloid develops with its envelope elongated along $\boldsymbol{a}$. With decreasing temperature the envelope becomes circular, before becoming elongated along $\boldsymbol{b}$. Finally the cycloid collapses and all the moments point along $\boldsymbol{b}$ in the AFM_b phase. Our x-ray data therefore reveals a complex and evolving cycloidal magnetic structure that mediates the SRT.

2.2.4 Symmetry analysis of the cycloidal order

A theoretical justification of our cycloidal model can be provided by a symmetry analysis of terms in the free energy. Here, I will outline the details of such an analysis developed by Roger Johnson. Further details can be found in Ref. [61].

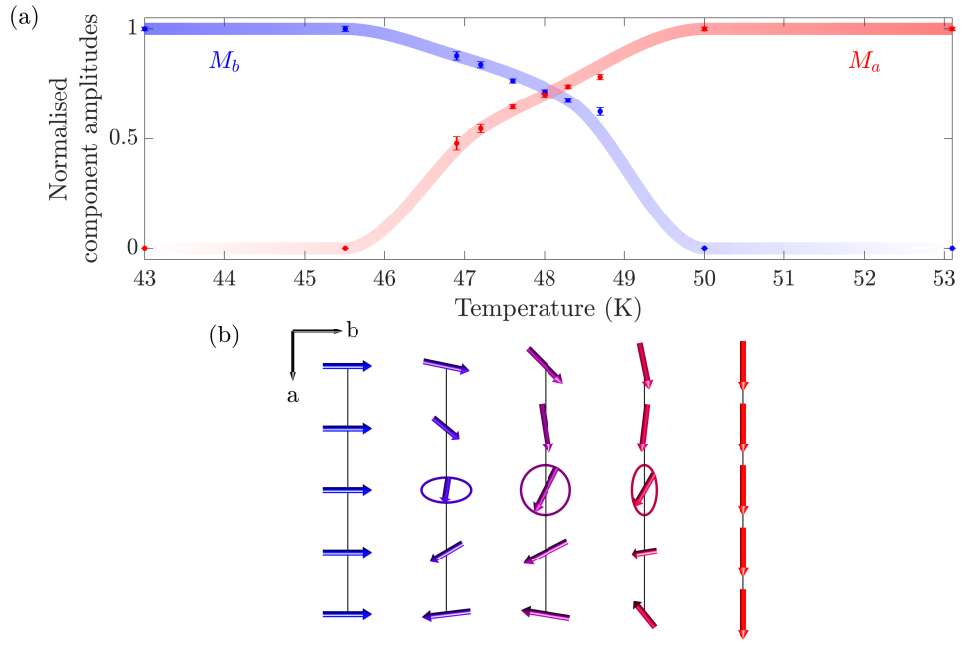

Figure 2.6: (a) Amplitudes of the cycloid components extracted from fits like those in Fig. 2.5(b), normalised by $\sqrt{M_a^2 + M_b^2}$ to remove the effect of the increasing moment size on cooling. Solid lines are guides to the eye. (b) Schematic of the evolution of the magnetic structure with temperature, with the lengths of the arrows indicating the changing of the cycloidal envelope from elongated along $\boldsymbol{b}$, to circular, to elongated along $\boldsymbol{a}$. The changing moment size and period of the cycloid are neglected for clarity.

The AFM_a and AFM_b structures both have a Y-point propagation vector $(0, 0, 1)$. The full Y-point magnetic representation for the Ru Wyckoff site $8b$ decomposes into four one-dimensional irreps: mY_1, mY_2, mY_3, and mY_4. Symmetry-adapted modes of mY_4 correspond to the AFM_a magnetic structure, and symmetry-adapted modes of mY_2 correspond to AFM_b. The AFM_a and AFM_b phases can each be associated with a one-dimensional order parameter, say μ and ρ, that transform by mY_4 and mY_2 respectively. These order parameters can be combined into a Lifshitz-type free energy term, of the form $\mu(\partial\rho/\partial y) - \rho(\partial\mu/\partial y)$, that is allowed by the non-centrosymmetric symmetry of $Ca_3Ru_2O_7$. It is well known that the presence of Lifshitz invariants in the free energy implies an instability of the system towards long-range modulated states [69], such as the cycloidal magnetic structure in polar $BiFeO_3$ [67, 70]. The free energy term specified above promotes a cycloid propagating along $\boldsymbol{a}$.

The observed propagation vector of the cycloid, $(\delta, 0, 1)$, is equivalent to $(\delta - 1, 0, 0)$ located on the Δ-line of symmetry. The reducible Δ-line magnetic representation for the Ru Wyckoff site decomposes into two two-dimensional irreps, $\mathrm{m}\Delta_1$, and $\mathrm{m}\Delta_2$. The compatibility relationships, $\mathrm{m}\Delta_1 = \mathrm{mY}_1 \oplus \mathrm{mY}_3$ and $\mathrm{m}\Delta_2 = \mathrm{mY}_2 \oplus \mathrm{mY}_4$, indicate that the modulated states that transform by the $\mathrm{m}\Delta_2$ irrep decompose into mY_2 and mY_4 order parameters in the commensurate limit. Hence, the magnetic cycloid stabilised by the Lifshitz invariant, which is expected to be a small perturbation of the commensurate magnetic structures associated with the mY_2 and mY_4 irreps, transforms according to the $\mathrm{m}\Delta_2$ irrep.

This symmetry analysis gives us an intuitive understanding of the cycloid-mediated SRT. Lifshitz invariants are known to originate from the SOC-generated DMI (see Sec. 2.1.1). In $Ca_3Ru_2O_7$, the uniform DMI competes with the easy-axis anisotropies (see Sec. 2.3.4) to select the ground state of the system. Away from T_S, the easy-axis anisotropies dominate and preclude the formation of a modulated state, leading to the $\mathrm{AFM_b}$ or $\mathrm{AFM_a}$ phases. As the easy axis gradually changes from $\boldsymbol{b}$ to $\boldsymbol{a}$ in the vicinity of the SRT, however, we expect minimal or easy-plane anisotropy, allowing the uniform DMI to dominate and stabilise the ICC phase. This general mechanism should be at play whenever magnetic anisotropies compete in a system with broken inversion symmetry.

2.2.5 Tuning the cycloidal texture with magnetic field

Given that the structure of the cycloid is dependent on competing magnetic anisotropies, it is natural to wonder how it might respond to an applied magnetic field. To investigate this, we performed further neutron scattering measurements on $Ca_3Ru_2O_7$ with a magnetic field applied along the $\boldsymbol{b}$ axis. The resulting temperature–field phase diagram is shown in Fig. 2.7(a). The most striking feature is a large expansion of the temperature range over which the ICC phase is stable under field, increasing from $\sim$3 K at zero field to $>$10 K at a field of 5 T.

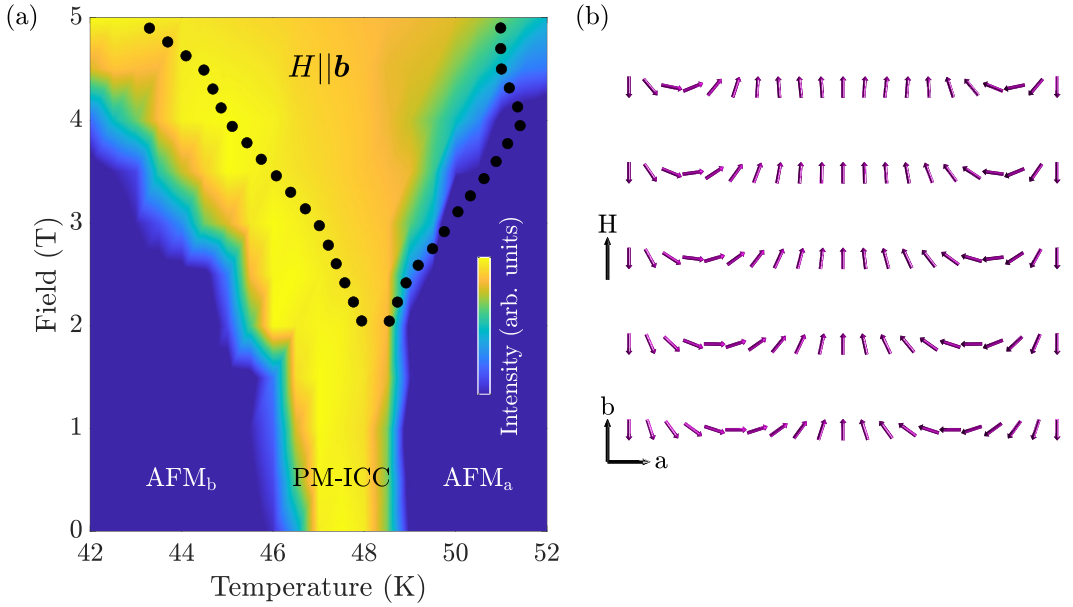

Figure 2.7: (a) Magnetic phase diagram of $Ca_3Ru_2O_7$ for a field along the $\boldsymbol{b}$ axis from neutron scattering, constructed from temperature sweeps at fixed field. The colour scale is the integrated intensity of the $(\delta, 0, 1)$ peak, with the AFM_b, AFM_a and phase-modulated incommensurate cycloid (PM-ICC) phases marked. The black dotted line encloses the region over which peaks at $(\Delta, 0, 0) \approx (2\delta, 0, 0)$ were seen in a previous SANS measurement [57]. (b) Cartoon of the PM-ICC structure with increasing field for each row up, depicted with a circular envelope for clarity.

It is interesting to note that the boundary of the ICC phase overlaps with that of a so-called "metamagnetic texture" recently reported by Sokolov *et al.* on the basis of small-angle neutron scattering (SANS) measurements [57]. Sokolov *et al.* saw incommensurate peaks at $(\pm\Delta, 0, 0)$ in fields above 2 T, whose appearance coincides with sudden "metamagnetic" jumps in the magnetisation. Without being able to solve the magnetic structure, they proposed a complex texture that modulates between ferromagnetic and antiferromagnetic alignments of the spins in adjacent bilayers. Such a structure was motivated by Lifshitz-type invariants similar to those that stabilise our cycloid, but as they did not see the incommensurate phase at zero field Sokolov *et al.* were forced to consider high-order invariants that couple the ground-state antiferromagnetic order parameter to a field-polarised ferromagnetic order parameter.

Our discovery of the ICC phase at zero field permits a simpler expla-

nation in terms of a coupling between the AFM_a and AFM_b order parameters. The connection between the magnetic satellites that we observe and those measured by Sokolov *et al.* can be seen by doubling our wavevector, $2 \times (\delta, 0, 1) = (2\delta, 0, 2)$, and then projecting back into the first Brillouin zone through subtraction of a lattice vector, $(2\delta, 0, 2) - (0, 0, 2) = (2\delta, 0, 0)$. The wavevectors of the satellite peaks are field and temperature dependent, but comparing the value from our data at 2 T and 47 K, $\delta \approx 0.023$, with the SANS data at at the same field and temperature, $\Delta \approx 0.045$, we can see the correspondence $2\delta \approx \Delta$. It is then apparent that the peaks observed by Sokolov *et al.* are in fact second harmonics of our satellites. While we could not directly observe the second harmonic satellites in our experiment due to the low flux of long-wavelength neutrons at such high d spacing, their appearance under magnetic fields is naturally explained by a phase modulation of the cycloid. This corresponds to the spins bunching along the field direction in order to reduce their Zeeman energy, as shown schematically in Fig. 2.7(b). In this scenario, a net magnetisation develops as higher harmonics are generated continuously from the zero-field cycloid, in the absence of any metamagnetic transition. Such behaviour is reminiscent of the highly robust, tuneable soliton lattices seen in chiral helimagnets under field [71].

This phase modulation is also fully consistent with a symmetry analysis of terms in the free energy. In zero field we have a fundamental propagation vector $\pm\boldsymbol{k}_1$ and can write a complex order parameter (η_1, η_1^*), where η_1 and η_1^* correspond to $+\boldsymbol{k}_1$ and $-\boldsymbol{k}_1$ respectively, and their appropriate linear combination gives the real values of the magnetic moments. We now consider the effect of applying a magnetic field, H, along the $\boldsymbol{b}$ direction. H, and the Γ-point magnetisation it creates, transform by the $m\Gamma_2$ irrep. This field will couple to additional magnetic order parameters, with the lowest-order linear invariant being $H(\eta_2^*\eta_1^2 + \eta_2\eta_1^{*2})$. Here, (η_2, η_2^*) is a second-harmonic cycloidal component with propagation vector $\boldsymbol{k}_2 = 2\boldsymbol{k}_1$ that transforms as $m\Delta_2$. Therefore, whenever H is finite, the energy of the system will be lowered through the

creation of a second harmonic modulation of the cycloid. More generally, this invariant can be written to higher orders as $H(\eta_n^*\eta_1^n + \eta_n\eta_1^{*n})$, where (η_n, η_n^*) is the order parameter of the n^{th} harmonic for even n. Similarly, odd harmonics will be generated by quadratic invariants $H^2(\eta_n^*\eta_1^n + \eta_n\eta_1^{*n})$ with n odd. This infinite series of even and odd harmonics combine to form the phase-modulated ICC (PM-ICC) depicted in Fig. 2.7(b).

As well as providing a more natural explanation of the magnetic behaviour under field, our results also offer a new understanding of incommensurate peaks previously reported in $Ca_3Ru_2O_7$ doped with Ti [72], Fe [58] and Mn [59] on the Ru site (but again, offered without proper structural solutions). Here, a disrupted magnetic anisotropy from the introduction of dopants should allow an easier turning of the moments away from their easy axis by the DMI, stabilising ICC structures with shorter repeat distances and over larger temperature ranges. Our analysis therefore unifies previously disparate magnetic behaviours of $Ca_3Ru_2O_7$, attributing them to a common origin and revealing a highly rich phase diagram.

2.3 Tuning the spin-reorientation transition with strain

We saw in Sec. 2.2.2 how the transitions into and out of the ICC phase coincide with changes in slope of the in-plane resistivity, caused by a reconstruction of the Fermi surface. These are not the only degrees of freedom involved in the transitions, however, with jumps also seen in the lattice parameters. Figure 2.8 shows the temperature dependence of the lattice parameters determined by REXS, alongside the intensities of the commensurate and satellite magnetic peaks from neutron scattering. On cooling from the AFM_a phase, discontinuities can be seen at the transitions into the ICC phase and then into the AFM_b phase, with the c lattice parameter decreasing as a and b increase. While previous uniaxial pressure experiments have produced conflicting results [73, 74], hydrostatic pressure has been shown to sharply reduce both T_N and T_S [75, 76].

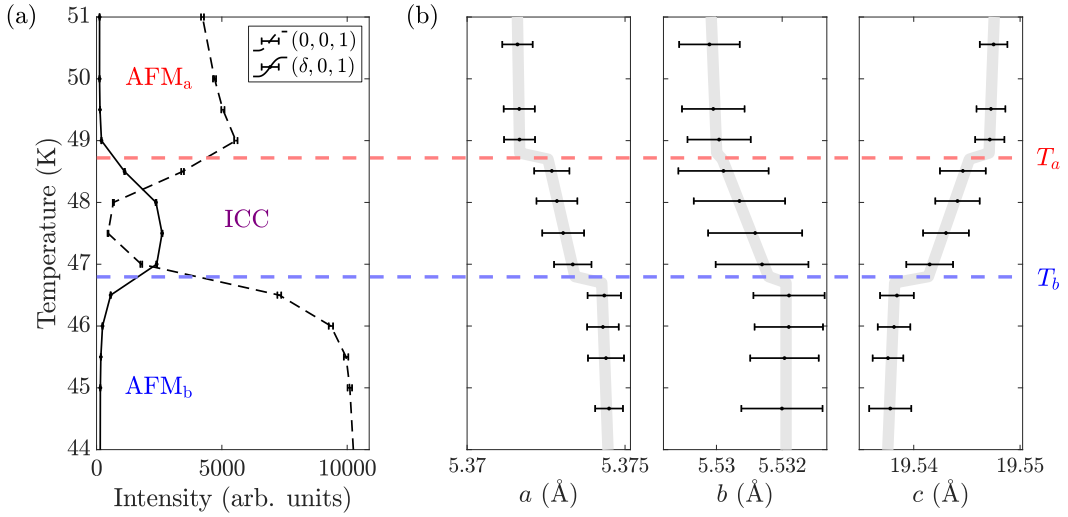

Figure 2.8: (a) Integrated intensity of the commensurate $(0, 0, 1)$ (dashed line) and satellite $(\delta, 0, 1)$ (solid line) peaks as a function of temperature. (b) Lattice parameters of $Ca_3Ru_2O_7$ as a function of temperature. The temperature of the $AFM_a \rightarrow ICC$ transition is labelled T_a, and of the $ICC \rightarrow AFM_b$ transition T_b.

A recent report of changes to the lattice parameters on application of a magnetic field [76] further demonstrates the intricate coupling between the crystal and magnetic structures in $Ca_3Ru_2O_7$. This raises the intriguing possibility of controlling the magnetism by tuning the lattice.

In this section, I show how such control is possible by the application of anisotropic strain. I will first describe the construction of new setups to allow *in situ* strain-tuning during neutron scattering, REXS and resistivity measurements. These enable an unprecedented insight into the response of the crystalline lattice to strain, including a quantification of the Poisson ratios and subtle effects like sample bending. I will then show how anisotropic strain can drive the $AFM_a \rightarrow ICC$ and $ICC \rightarrow AFM_b$ transitions at fixed temperature, confirming a key role for the lattice in these transitions. Detailed REXS measurements show that the transition temperatures vary linearly with strain, and resistivity measurements show that the Fermi surface changes are locked to the magnetic and structural transitions. Finally, I describe a theoretical model motivated by our strain experiments that attributes the SRT to changes in the tilts and rotations of the RuO_6 octahedra.

The design and construction of the strain setups involved extensive collaboration with scientists and engineers from Razorbill Instruments, who provided the strain cells, the Diamond Light Source and the ISIS Neutron and Muon Source. Sample preparation was performed by me and Robin Perry. The neutron scattering measurements under strain were performed by me, Larissa Veiga, Quentin Faure, Robin Perry and Roger Johnson, with Pascal Manuel, Dmitry Khalyavin and Fabio Orlandi as local contacts, and technical support from Jacob Simms, Katherine Mordecai, Jon Bones and David Keymer. The REXS measurements under strain were performed by me, Larissa Veiga, Quentin Faure, Robin Perry and Roger Johnson, with Dan Porter as local contact, and technical support from Mike Matthews. The resistivity measurements under strain were performed by me, with technical support from Richard Thorogate. Data analysis was performed by me, with support from Dan Porter and overseen by Des McMorrow. The theoretical model of the strain-driven SRT was developed by Adam Walker, Michal Kwasigroch, Frank Krüger and Andrew Green.

2.3.1 Experimental details

A central activity in quantum materials research is to modify the properties of a material and access new phases using various stimuli. Popular tuning parameters include temperature, chemical doping, applied electric and magnetic fields, and hydrostatic pressure. Recently, anisotropic strain has received increasing interest as a new tuning parameter, propelled in large part by advances in the design of strain cells by Razorbill Instruments [77, 78]. These use a series of piezoelectric stacks to move two bridges of the titanium cell, each of which is attached to one end of a long, bar-shaped sample. This allows continuously tuneable tensile and compressive strains to be applied down to cryogenic temperatures, with the thermal expansion of the stacks compensated by their arrangement. A clever arrangement of flexures ensures that the stress on the sample is uniaxial, and the cells contain a capacitive displacement sensor to allow the applied strain to be tracked in real time. Razorbill cells

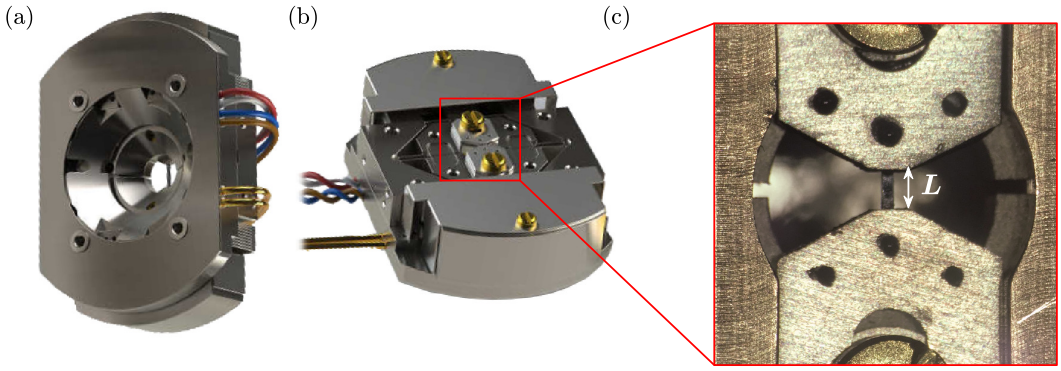

Figure 2.9: (a) Image of the back of the Razorbill CS200T strain cell used for neutron scattering, showing the 90° access cone to allow transmission measurements. (b) Image of the front of the CS200T cell, showing the sample plates screwed to the two bridges (in red box). Images in (a) and (b) are from Razorbill Instruments [77]. (c) Close-up of a bar-shaped $Ca_3Ru_2O_7$ sample mounted across a distance L between the sample plates.

have enabled groundbreaking experiments in a number of materials, first of all in Sr_2RuO_4, which showed rapid increases in its superconducting transition temperature under both tensile and compressive strain [79, 80]. Razorbill cells have also been used to modify charge order in the superconducting cuprates [81, 82], and, as the conjugate field to nematicity, anisotropic strain has found a key application in the iron-based superconductors [83, 84, 85, 86].

For our neutron scattering measurements at the WISH instrument of the ISIS Neutron and Muon Source, we employed the Razorbill CS200T cell shown in Fig. 2.9. This cell incorporates a large access cone [see Fig. 2.9(a)] to allow scattering in a transmission geometry. Each end of the $Ca_3Ru_2O_7$ sample is glued with Stycast 2850FT epoxy to titanium sample plates, which are screwed to each of the bridges of the cell as shown in Fig. 2.9(b). The sample spans a distance $L \approx 1\,\text{mm}$ between the plates [Fig. 2.9(c)] with its centre sitting at the apex of the access cone. When a voltage is applied to the piezoelectric stacks they expand or contract, changing the distance between the bridges by ΔL and applying a strain $\Delta L/L$ (of maximum magnitude around 0.5%) to the sample. The CS200T cell was mounted on a custom cryostat stick with feedthroughs for the cables to power the cell and measure the capacitance of

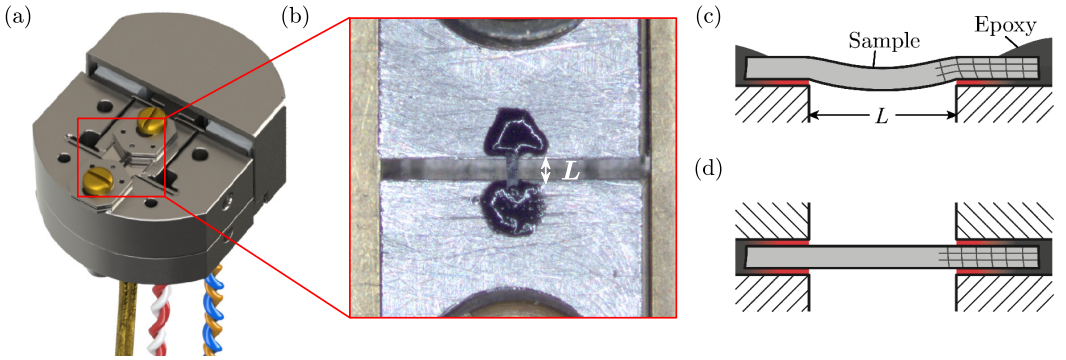

Figure 2.10: (a) Image of the Razorbill CS100 strain cell used for REXS, from Razorbill Instruments [77]. (b) Close-up of a $Ca_3Ru_2O_7$ sample mounted across a distance L between the sample plates. (c) Schematic diagram of the mounting on a CS100 cell, with the sample attached only to plates below. This asymmetric mounting causes the sample to bend under strain. (d) Symmetric mounting with sample plates both above and below the sample, as used in transmission measurements (see Fig. 2.9). Diagrams in (c) and (d) are adapted from Ref. [78].

the displacement sensor. Voltage was applied to the cell with an RP100 power supply from Razorbill Instruments, and the capacitance was measured with a Keysight E4980AL LCR meter, both of which were integrated into the instrument control software to allow automated control and data acquisition. A temperature sensor was thermally contacted with the body of the cell, giving accurate readings of the sample temperature, and cadmium shielding was used to reduce background scattering from the cell while still allowing maximum beam access to the sample. The scattering geometry and data analysis procedures were the same as those detailed in Sec. 2.2.1.

For the REXS measurements at beamline I16 of the Diamond Light Source, size limitations of the closed-cycle cryostat and the reflection scattering geometry required use of the smaller CS100 cell, shown in Fig. 2.10(a). The principles of operation of this cell are identical to the CS200T above, with the sample mounted between two plates that are attached to each bridge of the cell. The maximum displacement of the CS100 is $\Delta L_{\text{max}} \approx \pm 3\,\mu\text{m}$, compared to $\pm 11\,\mu\text{m}$ for the CS200T, but the increased flux and REXS cross section compared to neutron scattering allows smaller samples with $L \approx 300\,\mu\text{m}$ to

be used, giving higher maximum applied strains $|\Delta L/L|_{\max} \approx 1\%$. A custom mount was designed to hold the cell in the cryostat, with feedthroughs added for the power and capacitance cables. As at WISH, the RP100 power supply and E4980AL LCR meter were interfaced with the beamline software to allow remote control and scripting of the measurements. A Cernox temperature sensor was thermally contacted with the body of the cell. All other beamline parameters and data analysis procedures were the same as those detailed in Sec. 2.2.1.

A requirement of the reflection geometry used at I16 is a large sphere of access for the incident and scattered beams. In the neutron scattering setup, sample plates were placed below and above the sample, both anchored to the cell with a screw and separated by a spacer. As shown in Fig. 2.10(d), this results in stress being transmitted via the epoxy to both the top and bottom surfaces of the sample equally, ensuring homogenous strain. The top sample plates block beam access, however, and so were not used in the REXS setup. This leaves the sample attached to the cell only via its lower surface, as shown in Figs. 2.10(b) and (c). The asymmetric mounting causes the sample to bend under stress (downwards for tensile stress, and upwards for compressive stress) and a strain gradient to form through the sample. The strain gradient is reduced by having a high ratio of sample length to thickness, $L/t \gg 1$, which is natural for the easily-cleaved $Ca_3Ru_2O_7$ samples (note, however, that we must keep $L/t < \pi/\sqrt{3\Delta L/L} \approx 18$ to prevent the sample buckling under strain [78]). The magnitude and consequences of the bending will be investigated in Sec. 2.3.2.

To correlate the changes in crystal and magnetic structures with the transport properties, we also performed four-probe resistivity measurements under strain in a Quantum Design PPMS. For this we used the same CS100 cell as the REXS measurements, with the addition of a wiring platform to allow electrical contacts to be made to the sample [see Fig. 2.11(a)]. Four 25 µm-diameter gold wires were contacted along the length of the sample with Dupont 6838

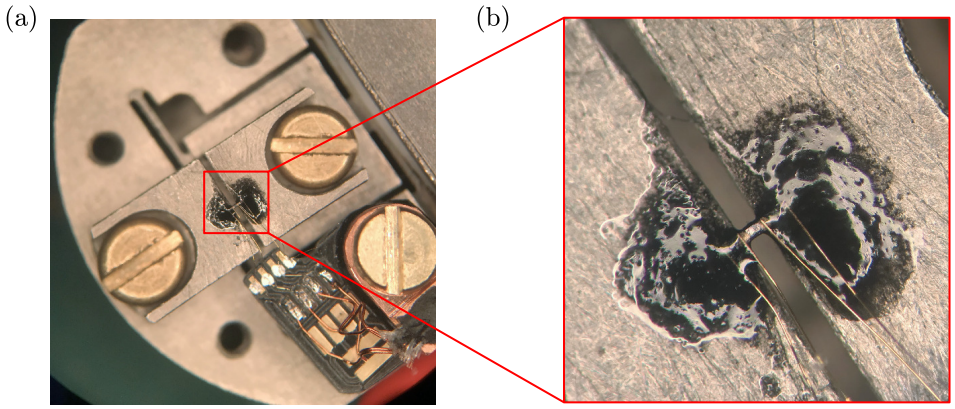

Figure 2.11: (a) Image of the CS100 cell set up for resistivity measurements, with the wiring platform visible on the bottom right. (b) Close-up of a $Ca_3Ru_2O_7$ sample mounted on the cell, with gold wires contacted to the top surface in a standard four-probe configuration.

silver paint, and cured at 900 °C for 5 min. This results in mechanically robust contacts that can survive the repeated deformation caused by the applied strain, and it was checked that the brief exposure to high temperature does not change the transport properties of the sample. The other ends of the wires were connected with silver epoxy to pads on the wiring platform, which was in turn connected to a standard PPMS puck. The sample was mounted using only lower sample plates to reproduce the conditions of the REXS measurements, and 10 µm nylon threads were placed in the epoxy below the sample to prevent electrical contact with the titanium cell (which is grounded during the measurement). The sample was positioned such that the current contacts at the ends of the sample are in the unstrained region covered by epoxy, while the voltage contacts sit in the strained region suspended between the sample plates [see Fig. 2.11(b)]. The contacts are only on the top surface of the sample, so the current will spread downwards over a length scale $t\sqrt{\rho_c/\rho_{ab}} \sim 100\,\mu\text{m}$ [84]. As this is of the same magnitude as the length between the voltage contacts, there will be a significant contribution to the measured resistivity from ρ_c. Thankfully, ρ_{ab} and ρ_c follow the same trend in the region of interest above 45 K, so this does not affect the determination of the transition temperatures that we are interested in. The CS100 was mounted on a

custom PPMS probe supplied by Razorbill Instruments, with feedthroughs for the power and capacitance cables. No temperature sensor was mounted on the cell, but through comparison with the neutron and REXS data a constant 2 K offset was found between the cryostat and sample temperatures, which has been corrected throughout. A custom LabView program was written to interface with the power supply, LCR meter and the PPMS MultiVu software, and allow scripting and automatic logging of measurements.

$Ca_3Ru_2O_7$ crystals from the same batches as in Sec. 2.2.1 were used for the strain measurements. These were aligned with Laue diffraction, and cut into bars using a Logitech wire saw with 100 µm tungsten wire and a 1 µm diamond slurry for the abrasive. Samples were cut with the long axis, along which stress is applied, along both the $\boldsymbol{a}$ and $\boldsymbol{b}$ directions. The samples were found to naturally cleave during cutting, producing long, thin bars with clean $(0, 0, 1)$ faces for scattering. The dimensions of the sample used for neutron scattering were $L \times w \times t \approx 1 \times 0.3 \times 0.05$ mm (where L is the strained distance between the sample plates), for REXS with stress along $\boldsymbol{a}$ were $0.3 \times 0.1 \times 0.04$ mm, for REXS with stress along $\boldsymbol{b}$ were $0.2 \times 0.1 \times 0.03$ mm, and for resistivity measurements were $0.3 \times 0.1 \times 0.03$ mm.

2.3.2 Response of the lattice to uniaxial stress

The capacitive displacement sensors built into the strain cells allow real-time determination of the applied strain $\Delta L/L$. This is not an accurate measure of the *true* strain in the sample, however, for two main reasons. The first issue is that the epoxy connecting the sample to the cell will deform and take up some of the strain, which is then not transmitted to the sample. In most studies to date, deformation of the epoxy is accounted for by scaling the applied strain by a universal factor (usually between 0.7–0.8) calculated using finite element analysis [79, 80, 83, 85, 86]. In the RIXS studies on cuprates, the position of a single Bragg peak was tracked and the linear dependence at low strain used to calculate a universal scale factor, even though the dependence deviated from linear at high strain [81, 82]. The second issue is that the thermal contraction

of the sample and titanium cell are unlikely to match, resulting in a thermally-induced strain that is not detected by the capacitor, effectively shifting the zero point. Estimation of the zero point then requires calculation of the differential thermal contraction, or the identification of some feature in the data that occurs at zero strain. These issues are compounded by varying responses of the capacitor and epoxy with temperature, and the various complicated ways that strain can be accommodated by the sample (domain formation, buckling, breaking, etc.).

Our REXS measurements avoid these issues by directly measuring the response of the crystalline lattice to the applied stress. Note the use of the word *stress* here. Although we measure the strain on the lattice, the Razorbill cells actually apply a uniaxial stress (or pressure) to the samples, which results in strains along all three crystallographic axes. To formalise this, we can introduce the stress and strain tensors, σ_{ij} and ε_{ij} respectively, whose diagonal terms correspond to the stress/strain along the principle axes, while the off-diagonal terms give shear stresses/strains. In the elastic limit (i.e. no permanent plastic deformation), applying a stress to a body results in a strain

$$\varepsilon_{ij} = S_{ijkl}\sigma_{kl} \tag{2.1}$$

(summing over repeated indices), where $\boldsymbol{S}$ is the fourth-order compliance tensor. As the stress and strain tensors are symmetric, the compliance tensor satisfies $S_{ijkl} = S_{jikl}$, $S_{ijkl} = S_{ijlk}$ and $S_{ijkl} = S_{klij}$, such that we can introduce the reduced notation

$$ij \rightarrow \begin{cases} i & \text{for } i = j \\ 9 - (i + j) & \text{for } i \neq j \end{cases} \tag{2.2}$$

and the same for kl, allowing the compliance tensor can be expressed as a 6×6 matrix. The crystal symmetry of $Ca_3Ru_2O_7$ then restricts $\boldsymbol{S}$ to the symmetric

form

$$\boldsymbol{S} = \begin{pmatrix} S_{11} & S_{12} & S_{13} & 0 & 0 & 0 \\ S_{12} & S_{22} & S_{23} & 0 & 0 & 0 \\ S_{13} & S_{23} & S_{33} & 0 & 0 & 0 \\ 0 & 0 & 0 & S_{44} & 0 & 0 \\ 0 & 0 & 0 & 0 & S_{55} & 0 \\ 0 & 0 & 0 & 0 & 0 & S_{66} \end{pmatrix}, \tag{2.3}$$

with nine independent elements. We apply uniaxial stresses, σ_{ii}, in our experiments, so are only interested in the upper-left 3×3 block of $\boldsymbol{S}$. The stress–strain relationship can then be written

$$\begin{pmatrix} \varepsilon_{aa} \\ \varepsilon_{bb} \\ \varepsilon_{cc} \end{pmatrix} = \begin{pmatrix} \frac{1}{E_a} & -\frac{\nu_{ba}}{E_b} & -\frac{\nu_{ca}}{E_c} \\ -\frac{\nu_{ab}}{E_a} & \frac{1}{E_b} & -\frac{\nu_{cb}}{E_c} \\ -\frac{\nu_{ac}}{E_a} & -\frac{\nu_{bc}}{E_b} & \frac{1}{E_c} \end{pmatrix} \begin{pmatrix} \sigma_{aa} \\ \sigma_{bb} \\ \sigma_{cc} \end{pmatrix}, \tag{2.4}$$

where E_i are the Young's moduli, ν_{ij} are the Poisson ratios, and the requirement that $\boldsymbol{S}$ is symmetric leads to the relations $\nu_{ij}/E_i = \nu_{ji}/E_j$. We can therefore see that the uniaxial stresses applied by the Razorbill cells will result in strains along all three crystallographic axes, related by the Poisson ratios. Our REXS measurements give us access to all of these strains.

Having laid out the formalism, we will now determine the relationship between the applied strain as measured by the capacitative displacement sensor in the cell, $\Delta L/L$, and the true strain. Figure 2.12(a) shows representative 2θ scans of a structural Bragg peak as a function of applied strain, in this case for stress applied along $\boldsymbol{b}$. Changes to the lattice parameters result in shifts of the peak through Bragg's law

$$\sin\theta = \frac{\lambda}{2}\sqrt{\frac{h^2}{a^2} + \frac{k^2}{b^2} + \frac{l^2}{c^2}}. \tag{2.5}$$

Therefore, by measuring three peaks with different h, k and l components [in this case the $(0, 0, 6)$, $(1, 0, 7)$ and $(1, 1, 5)$ peaks], the lattice parameters

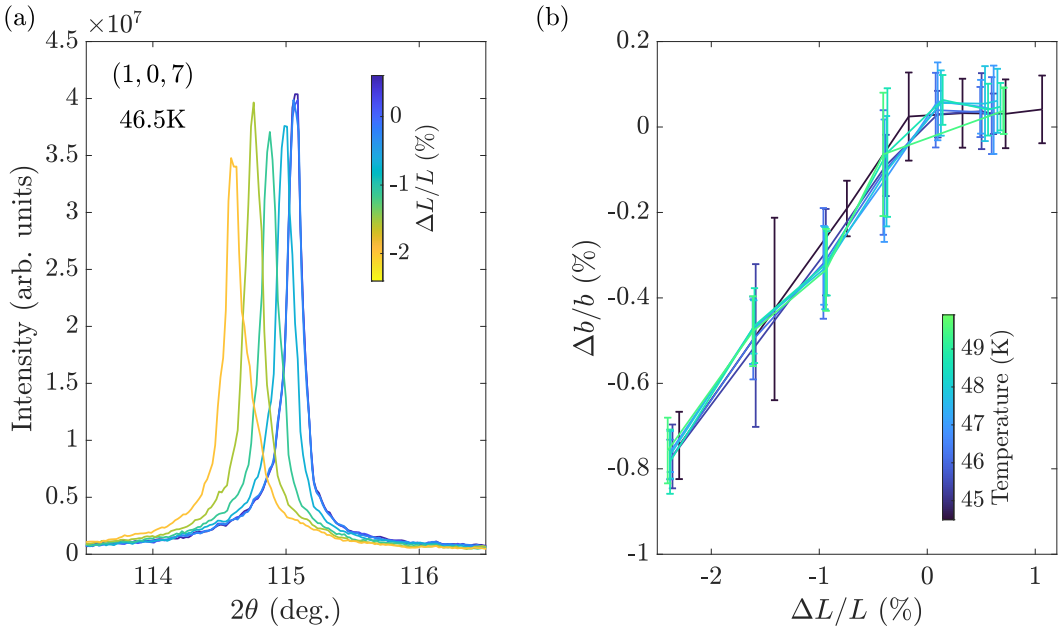

Figure 2.12: (a) 2θ scans of the $(1, 0, 7)$ structural Bragg peak, showing a shift with applied strain, $\Delta L/L$, along the $\boldsymbol{b}$ direction. (b) True strain along the b axis as a function of applied strain, for a range of temperatures through the ICC phase. Note that for this sample no tensile (positive) strain could be applied.

can be determined and compared to their zero-strain values to calculate the true strain. An example of the true strain, $\Delta b/b$, as a function of applied strain is shown in Fig. 2.12(b) for temperatures around the ICC phase. Under compression the dependence is linear and insensitive to temperature, with the true strain around 40% of the applied strain. Note that this is considerably lower than the estimates obtained with finite element analysis, and indicates a large deformation of the epoxy. Under tensile stress, by contrast, there appears to be no response from the lattice. Possible reasons for this will be discussed at the end of this section. These results highlight the danger in relying on the capacitive displacement sensor to determine the true strain, as has been done in most studies to date [79, 80, 81, 83, 82, 85, 86].

As noted above, our measurements allow us to determine the lattice strains along all three crystallographic directions. Figure 2.13(a) and (b) show the strains induced along the $\boldsymbol{a}$ and $\boldsymbol{c}$ directions due to stress applied along $\boldsymbol{b}$. It can be seen that the compressive strain along $\boldsymbol{b}$ is accompanied by tensile

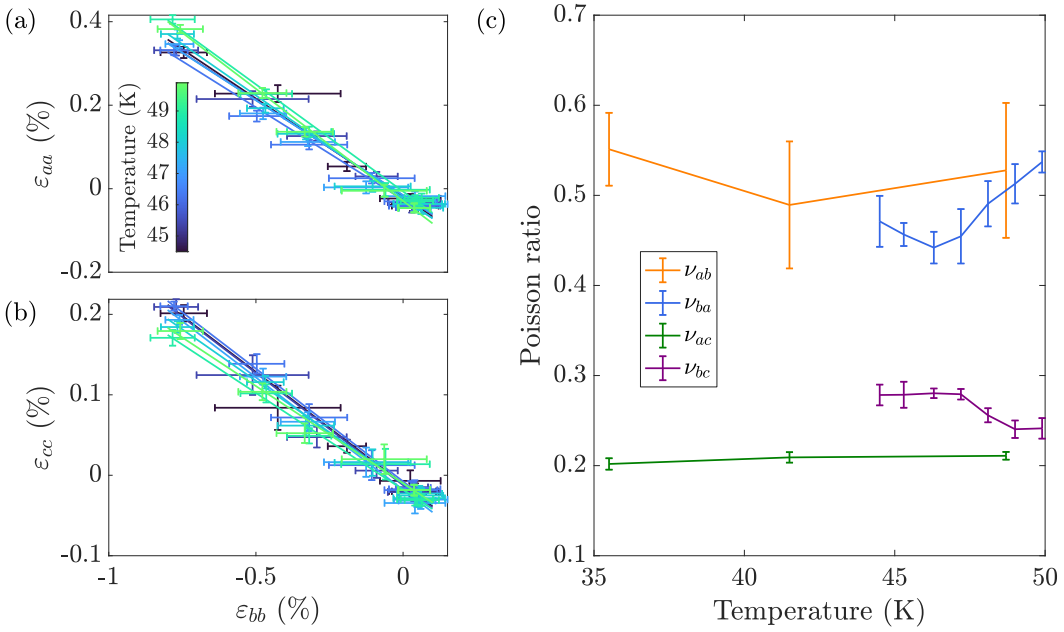

Figure 2.13: (a) Induced strain along $\boldsymbol{a}$, $\varepsilon_{aa} = \Delta a/a$, as a function of strain along $\boldsymbol{b}$, $\varepsilon_{bb} = \Delta b/b$, at a range of temperatures. Linear fits are shown as solid lines. (b) Induced strain along $\boldsymbol{c}$, $\varepsilon_{cc} = \Delta c/c$, as a function of strain along $\boldsymbol{b}$, with linear fits shown as solid lines. (c) Temperature dependence of the Poisson ratios, calculated from the slope of linear fits like those in (a) and (b).

strains along $\boldsymbol{a}$ and $\boldsymbol{c}$, with linear dependences at all measured temperatures. From Eq. (2.4), we find that the ratio of these strains is equal to the Poisson ratio, $\varepsilon_{jj}/\varepsilon_{ii} = -\nu_{ij}$. We can therefore determine the Poisson ratios from the slope of linear fits such as those shown in Fig. 2.13(a) and (b). The results are plotted as a function of temperature in Fig. 2.13(c). We find that $\nu_{ab} \approx \nu_{ba} \approx 0.5$ and $\nu_{ac} \approx \nu_{bc} \approx 0.2$ as expected for a layered material like $Ca_3Ru_2O_7$, with some evidence of ν_{ba} decreasing and ν_{bc} increasing on cooling through the cycloidal phase. We cannot determine ν_{ca} or ν_{cb} as we do not apply stress along $\boldsymbol{c}$, but from Eq. (2.4) we can see that $E_a \approx E_b$, giving $\nu_{ca} \approx \nu_{cb} \approx \nu_{ac}E_c/E_a$.

I have shown how tracking the 2θ positions of the structural Bragg peaks gives us information on the average changes in unit cell dimension though the probed region of the sample. We can further use the large Pilatus 100K area detector at I16 to efficiently map the peaks in full 3D reciprocal space, giving

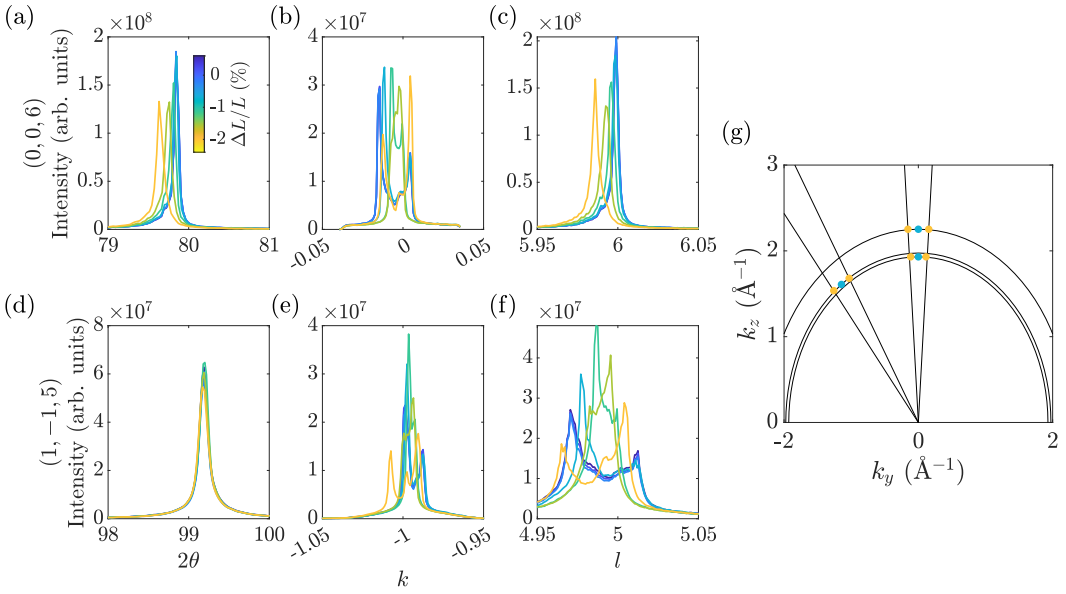

Figure 2.14: (a) 2θ, (b) k and (c) l scans of the $(0, 0, 6)$ structural Bragg peak at a range of applied strains along $\boldsymbol{b}$. Splitting can be seen along k for positive and negative applied strains. (d) 2θ, (e) k and (f) l scans of the $(1, -1, 5)$ structural Bragg peak at a range of applied strains along $\boldsymbol{b}$. Splitting can be seen along k and l for positive and negative applied strains. (c) Projected $k - l$ reciprocal space map in inverse Angstroms, showing the position of the split peaks at zero (blue) and maximum compressive (yellow) applied strain. The splitting of the $(0, 0, 5)$ magnetic peak is shown alongside the $(0, 0, 6)$ and $(1, -1, 5)$. The black lines depict the arcs and radial lines on which the split peaks lie.

unprecedented insight into stress-induced variations of the lattice through this region. Figure 2.14(a)–(f) shows 2θ, k and l cuts through two peaks at a range of applied strains along the $\boldsymbol{b}$ direction. Alongside the shifting of the peaks, a splitting can be seen along k for the $(0, 0, 6)$ peak, and along k and l for the $(1, -1, 5)$ peak, with a distribution of intensity between the extremal split components. The positions of the main components, converted into reciprocal Ångströms, are plotted in Fig. 2.14(g) for zero and maximum compressive strain. Under compression, the split peaks lie on arcs in reciprocal space and are separated by approximately the same angle. The splitting can therefore be naturally explained by a bending of the sample under stress, as predicted would occur in Sec. 2.3.1 due to the asymmetric mounting. Despite the bending, the peaks do not broaden in 2θ beyond our angular resolution, showing that the

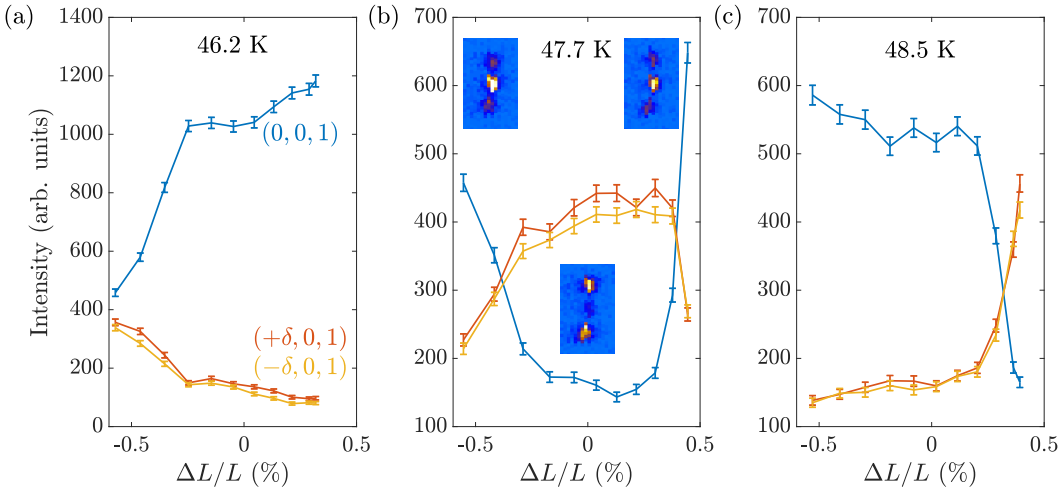

Figure 2.15: Integrated intensities of the $(0, 0, 1)$ (blue) and $(\pm\delta, 0, 1)$ (orange/yellow) peaks as a function of applied strain along $\boldsymbol{a}$, at (a) 46.2 K, (b) 47.7 K and (c) 48.5 K. The insets in (b) show detector images at zero and the maximal applied strains.

magnitude of the strain remains fairly homogeneous through the probed region. Interestingly, the peak splitting is symmetric for both tensile and compressive applied strain. This shows that our inability to transmit tensile strain to the sample is not due to it fully fracturing, but must be due to some other more complex mechanism of strain relaxation. Note that we do not see bending or an inability to transmit tensile strain in the neutron measurements at WISH, due to the symmetric mounting enabled by the transmission scattering geometry.

2.3.3 Driving the cycloid-mediated spin-reorientation transition with strain

Now that we have comprehensively characterised the response of the lattice to applied uniaxial stress, we are in a position to investigate how the magnetic structure changes. As a bulk probe of magnetic order, we first look to the neutron scattering measurements.

Figure 2.15 shows the integrated intensities of the commensurate $(0, 0, 1)$ and satellite $(\delta, 0, 1)$ magnetic peaks as a function of applied strain along $\boldsymbol{a}$, for three temperatures in the vicinity of the ICC phase. Starting with Fig. 2.15(b), taken in the centre of the ICC phase at 47.7 K, we can see a symmetric suppres-

sion of the satellite peaks, and a simultaneous enhancement of the commensurate peak, under both compressive and tensile strain. The commensurate intensity is lower under compression, suggesting that we are entering the AFM_a phase, while the higher commensurate intensity under tension is suggestive of the AFM_b phase. This is supported by the strain dependences taken at temperatures just above and below the ICC phase. At 46.2 K [Fig. 2.15(a)], where we are in the AFM_b phase at zero strain, the system is driven towards the ICC phase by compression, and at 48.5 K [Fig. 2.15(c)], where we are in the AFM_a phase at zero strain, the system is driven towards the ICC phase by tension. The transitions between the phases occur over a finite width of $\sim 0.3\%$ as the large neutron beam illuminates the entire un-masked region of the sample, including the areas towards the edges with significant strain gradients. Our neutron data conclusively show that transitions between the ICC and commensurate magnetic phases can be driven by strain at fixed temperature.

While our neutron setup has the benefit of being able to transmit both compressive and tensile strain to the sample, the scattering geometry blocks access to any structural Bragg peaks with a finite component along the stress direction, thereby precluding determination of the true strain. Further, the requirement of a large sample limits the maximum strains that we can achieve. The opposite is true for REXS, which we showed in the previous section can provide detailed information on the lattice for compressively strained samples an order of magnitude smaller than those required for neutron scattering. Figure 2.16 shows temperature–strain phase diagrams based on the REXS intensity of the $(-\delta, 0, 5)$ peak, for stress along both in-plane directions. Alongside the true strain along the direction of applied stress, the horizontal axes below the plots show the approximate strains along the orthogonal lattice directions determined from the temperature-averaged Poisson ratios in Fig. 2.13(c). For stress along $\boldsymbol{b}$ [Fig. 2.16(a)], both T_a and T_b vary linearly with strain at a rate of $\sim 7\,K/(\%\varepsilon_{bb})$. The data quality is worse for stress along $\boldsymbol{a}$, under which the structural Bragg peaks broadened considerably, most likely due to defects

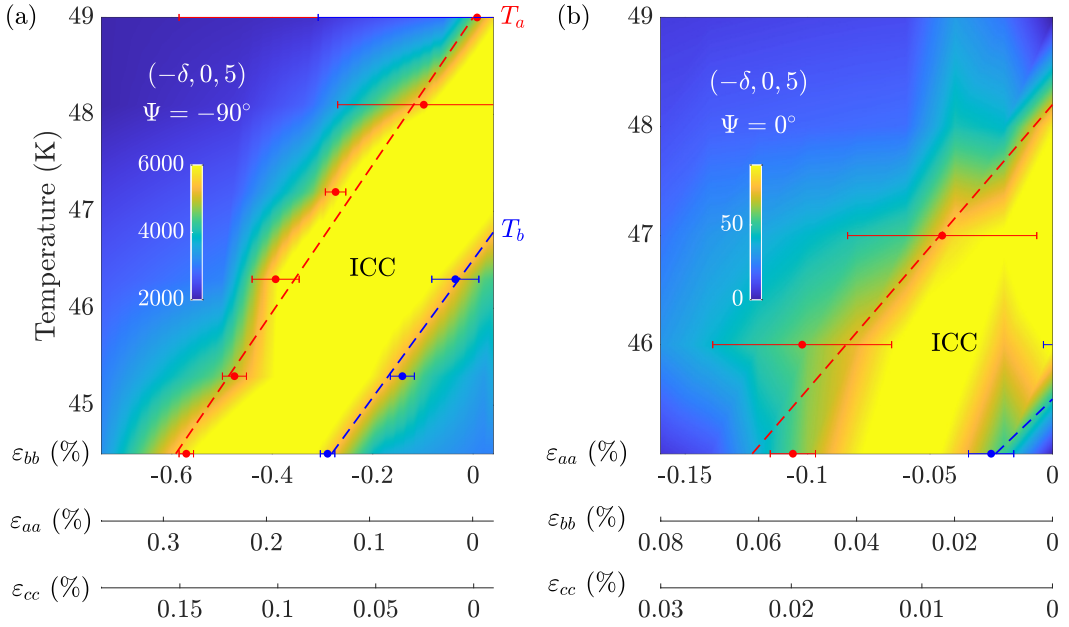

Figure 2.16: Phase diagrams for stress applied along the (a) ***b*** and (b) ***a*** directions, constructed from strain sweeps at fixed temperature. The colour scale is the integrated intensity of the $(-\delta, 0, 5)$ peak at azimuths of (a) $-90°$ and (b) $0°$, with separate horizontal axes for the strains along each axis. The points with error bars are fits to the ICC phase boundaries defined by the positions of half-maximum intensity, and the dashed red (blue) lines are linear fits through these points marking the strain dependence of T_a (T_b).

in the sample. Despite this, an approximately linear dependence of the transition temperatures on strain can still be seen, with a rate of $\sim 20\,K/(\%\varepsilon_{aa})$. Although we could not access the positive sides of the phase diagrams in our REXS experiments, from our neutron results we infer that T_a and T_b will continue to follow the same dependences under tension.

An interesting feature of the phase diagrams in Fig. 2.16 is that the transition temperatures move in the same direction for compressive strain along ***b*** (together with tensile strain along ***a***) and compressive strain along ***a*** (together with tensile strain along ***b***). The same movement of the phase boundaries for opposite in-plane deformations of the lattice suggests that the c-axis strain has a dominant role in driving the transitions. This conclusion is supported by the temperature dependence of the lattice parameters at zero strain [see Fig. 2.8(b)]. Above T_N, the a and c lattice parameters follow the same trend,

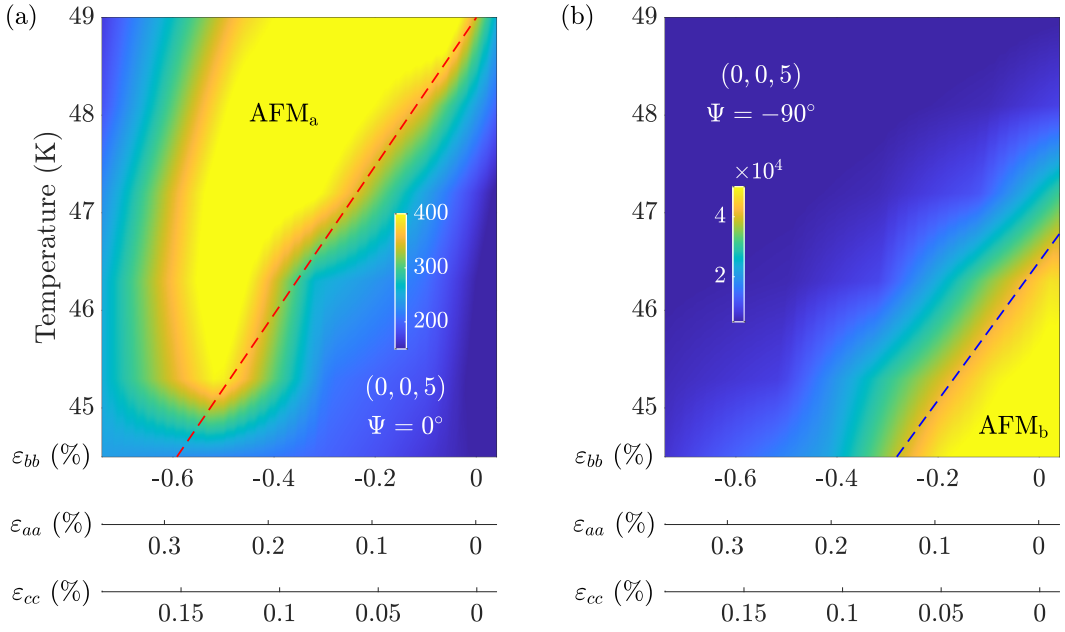

Figure 2.17: Phase diagrams for stress applied along $\boldsymbol{b}$, constructed from strain sweeps at fixed temperature. The colour scale is the integrated intensity of the $(0, 0, 5)$ peak at azimuths (a) $\Psi = 0°$ (sensitive to the AFM_a phase) and (b) $\Psi = -90°$ (sensitive to AFM_b). The dashed lines are the phase boundaries from Fig. 2.16(a).

opposite to that of b [35]. On cooling through the ICC phase, however, the c parameter shrinks while a and b increase, suggesting that the former is most strongly coupled to the transition, while the latter two respond mostly via the Poisson ratios.

To confirm that the phase boundaries in Fig. 2.16 do indicate transitions into the collinear phases, and not just a destruction of long-range magnetic order, we measured the commensurate $(0, 0, 5)$ peak alongside the $(-\delta, 0, 5)$ satellite for the sample stressed along $\boldsymbol{b}$. The intensities at two different azimuths are plotted in Fig. 2.17 as functions of temperature and strain. At an azimuth of $\Psi = 0°$ we are sensitive to the component of the moment along $\boldsymbol{a}$, and we can see that the AFM_a phase is established above the boundary where the ICC phase vanishes. Unexpectedly, the intensity is suppressed above $\varepsilon_{bb} \approx 0.6\%$ at all temperatures. The reason for this is unclear, but it may be connected to the bending of the sample at high strain (see Sec. 2.3.2), which could disrupt the long-range order of the already-weak AFM_a phase. Note

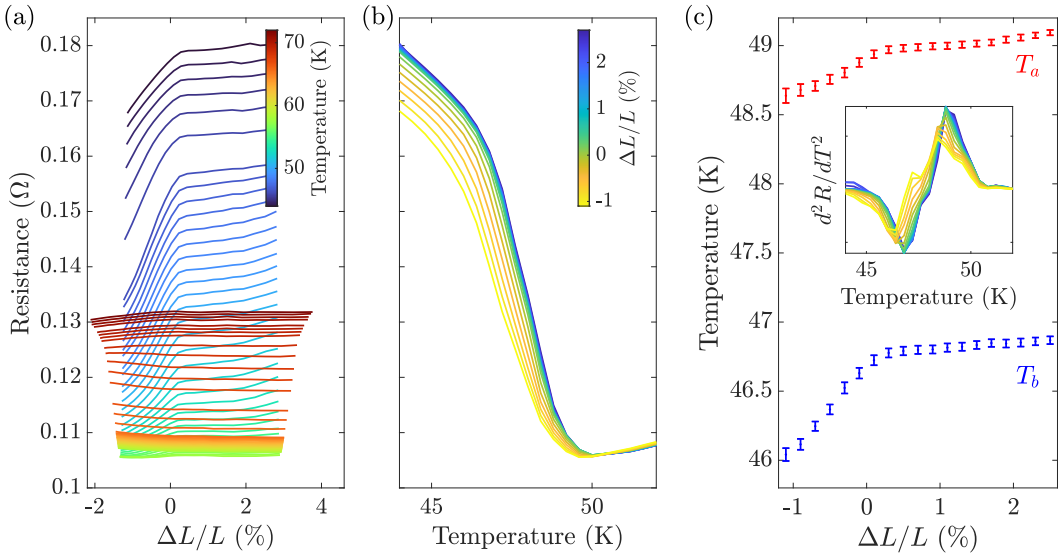

Figure 2.18: (a) Resistance as a function of applied strain along $\boldsymbol{a}$ at a range of temperatures through the AFM_a, AFM_b and ICC phases. (b) The same data as in (a) but plotted as a function of temperature for a range of applied strains. (c) Transition temperatures T_a and T_b as a function of applied strain, determined from the maxima and minima of d^2R/dT^2 respectively (see inset).

that there is no evidence of a similar suppression in our neutron results [see Fig. 2.15(c)] where the bending does not occur. At an azimuth of $\Psi = -90°$ we are sensitive to the component of the moment along $\boldsymbol{b}$, and we see the AFM_b phase appearing below the ICC phase boundary as expected.

Finally, we come to our transport measurements, taken under stress along $\boldsymbol{a}$. Figure 2.18(a) shows strain dependences of the in-plane resistance at a range of temperatures from the paramagnetic to the AFM_b phases. As we have no access to the true strain in the transport measurements, we have to rely on the capacitive displacement sensor. At the lowest temperatures where the resistance is highest, we see a clear decrease in resistance under compressive strain. There is little response to tensile strain, which is expected as we mount the sample asymmetrically to match the REXS measurements. On warming through T_b, the slope under compression decreases and the resistance appears to increase under high tensile strain $\Delta L/L > 2\%$. This again suggests that the sample is not broken, but finds some other mechanism to internally relieve tensile strain. On further warming above T_a, the resistance instead

begins to increase with compressive applied strain, before again falling under compression above T_N. The same data are plotted in Fig. 2.18(b) as a function of temperature in the vicinity of the ICC phase, showing the resistance curve shifting down in temperature under compression. At zero strain, the boundaries of the ICC phase coincide with changes of slope of the resistance [see Fig. 2.3]. To see if this correspondence is maintained under strain, we plot the maxima and minima of d^2R/dT^2 as a function of applied strain in Fig. 2.18(c). We again find linear dependences, although here we resolve a slightly different gradient for T_a and T_b. Given the uncertainties in converting applied strain to true strain, these results support the notion that the electronic and magnetic transitions are locked together.

2.3.4 Theory of the spin-reorientation transition

The coupled SRT in $Ca_3Ru_2O_7$ has received theoretical attention from multiple angles. Early work focussed on the Fermi surface gapping, and speculated that this might be due to the formation of charge- or spin-density waves driven by nesting [54, 51]. No direct experimental evidence for density waves could be found, however, and attention instead turned to the role of the magnetic structure.

Based on ARPES measurements and DFT calculations, Marković *et al.* proposed that the gapping was due to band hybridisation controlled by the moment direction [56]. Their DFT calculations showed a charge gap opening near the Brillouin zone centre when the magnetic moments are rotated away from the $\boldsymbol{a}$ direction. They attributed this to a Rashba-like SOC of the form $\boldsymbol{p} \cdot \boldsymbol{S} \times \boldsymbol{E}$, where $\boldsymbol{p}$ is the electron momentum, $\boldsymbol{S}$ is the magnetic moment, and $\boldsymbol{E}$ is a local electric field along $\boldsymbol{a}$ that arises from the breaking of inversion symmetry by the octahedral tilting. When $\boldsymbol{S}$ is along $\boldsymbol{a}$ we have $\boldsymbol{S} \times \boldsymbol{E} = \boldsymbol{0}$ such that there is no hybridisation, while for $\boldsymbol{S}$ along $\boldsymbol{b}$ a finite SOC can open the gap. They then argued that the spin reorientation with temperature occurs due to the changing thermal population of electronic states around the Fermi level: for $T > T_S$ the Fermi function is broad enough that there is no

energy gain from opening a gap, while for $T < T_S$ the electronic states above the hybridisation gap are not occupied and there is a finite energy gain from reorienting the spins to open the gap. The magnetic anisotropy in this model is therefore determined by the energy gained from hybridisation of the electronic bands, leading the authors to coin the term "magnetoelectric anisotropy".

While it provides a conceptually simple mechanism for the concomitant SRT and Fermi surface gapping, there are a number of issues with this model. Firstly, it is motivated by DFT calculations in the local spin-density approximation, whose validity for a correlated material like $Ca_3Ru_2O_7$ is questionable (the DFT band structure has to be renormalised by a factor of seven to match the ARPES data, for example). Secondly, it is not obvious from the above arguments why the moment reorients along $\boldsymbol{b}$ as opposed to $\boldsymbol{c}$. In fact, for a moment along $\boldsymbol{b}$ we have $(\boldsymbol{S} \times \boldsymbol{E}) \parallel \boldsymbol{c}$, such that the Rashba-like term is only non-zero for electrons with out-of-plane momenta. This is difficult to reconcile with the strongly 2D nature the electronic properties of $Ca_3Ru_2O_7$. Finally, and most importantly, this model is at odds with our strain measurements. Our ability to drive the SRT and Fermi-surface reconstruction with strain at fixed temperature contradicts the thermal-population argument, and reveals a central role for the lattice degrees of freedom that are neglected by Marković *et al.*

To explain our strain results, our collaborators developed an alternative model in which strain couples directly to the electronic system via the nearest-neighbour hopping. The first step in the argument is to assume that the RuO_6 octahedra stay rigid, and the dominant response to applied strain is a change in the octahedral rotations and tilts. Considering rotations and tilts separately (valid for small angles), the hopping can be calculated by expanding each orbital in a basis of orbitals quantised along the undistorted bond. The hopping matrix element is then expressed as a linear combination of Slater-Koster integrals for these undistorted bonds, with coefficients that depend on the rotation and tilt angles. Such an expansion is represented graphically

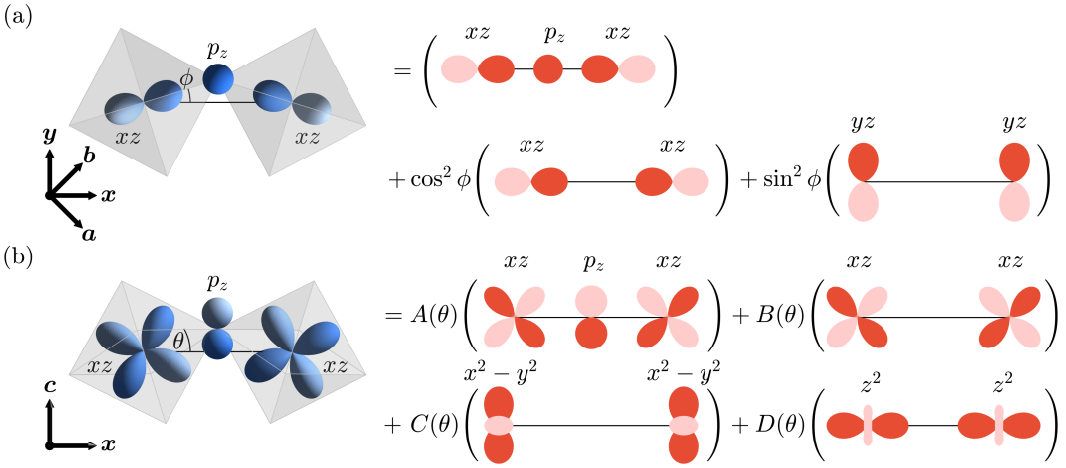

Figure 2.19: The effect of octahedral (a) rotation and (b) tilt on the hopping between nearest-neighbour xz orbitals (blue). In both cases, the hopping matrix element can be expanded in a basis of un-rotated orbitals (red) with coefficients that depend on the rotation angle θ and tilt angle ϕ. The coefficients in (b) are $A(\theta) = \frac{1}{4}[\cos(2\sqrt{2}\theta) + 4\cos(\sqrt{2}\theta) - 1]$, $B(\theta) = \cos^3(\sqrt{2}\theta)$, $C(\theta) = \frac{3}{4}\sin^2(\sqrt{2}\theta)$ and $D(\theta) = \frac{1}{4}\sin^2(\sqrt{2}\theta)\cos(2\sqrt{2}\theta)$.

for the case of hopping between xz orbitals in Fig. 2.19. With increasing rotation, indirect hopping via the O p_z orbital [first term in the expansion in Fig. 2.19(a)] is found not to change, while the direct π overlap (second term) is reduced and a weaker δ overlap (third term) develops. The overall hopping is therefore reduced with increasing rotation angle. The dependence on tilt is more complicated, but using expected values for the Slater-Koster integrals [87], and considering also the variation in Ru–Ru separation, gives that the hopping should increase with increasing tilt angle.

The variation in hopping with octahedral rotations and tilts motivates a model in which a strain field couples to an electronic Hubbard Hamiltonian. In the spirit of creating a minimal model to understand the essential physics at play, only two electronic bands in a perovskite monolayer are considered [55]. I note that the reduction to a monolayer means that the model cannot reproduce the cycloidal phase, as multiple bilayers are needed to break inversion symmetry and generate a uniform DMI. The model Hamiltonian is

$$H = H_t + H_U + H_\lambda. \tag{2.6}$$

Here, H_t is based on the tight-binding Hamiltonian of Ref. [55] that was derived from ARPES data. The nearest-neighbour hopping in H_t is modified by the strain field, ε, as $t = t_0 + \nu\varepsilon$, where the constant $\nu > 0$ results in stronger hopping for positive (tensile) strain. The scalar strain field represents the net effect of all lattice strains that couple to the hopping. The on-site intra-orbital Hubbard interaction is given by

$$H_U = U \sum_{j,\tau,\alpha} n_{j\tau\alpha\uparrow} n_{j\tau\alpha\downarrow}, \tag{2.7}$$

where the lattice site is labelled j, the Ru orbital is labelled $\alpha \in \{xz, yz\}$, and $\tau \in \{A, B\}$ is a sublattice index. Finally, H_λ is an on-site spin orbit coupling term that couples electrons of opposite spins in different orbitals

$$H_\lambda = -\frac{i\lambda}{2} \sum_{j,\tau} \left(\boldsymbol{c}^\dagger_{j\tau,xz} \sigma_z^\tau \boldsymbol{c}_{j\tau,yz} + h.c. \right), \tag{2.8}$$

where $\boldsymbol{c}^\dagger_{j\tau\alpha} = (c^\dagger_{j\tau\alpha\uparrow}, c^\dagger_{j\tau\alpha\downarrow})$. The octahedral tilting enters by rotating the spin quantisation axes on the sublattice sites by $\pm\theta$ about the b-axis, as $\sigma_z^{A(B)} = \cos(\theta)\sigma_z \pm \sin(\theta)(\sigma_x - \sigma_y)/\sqrt{2}$. The spin and charge fields are then decoupled in a mean-field approximation, yielding a free energy

$$F = -T \sum_{n,k} \ln\left(1 + e^{-(\epsilon_{nk} - \mu)/T}\right) + U \sum_{\tau,\alpha} \left(\boldsymbol{M}^2_{\tau\alpha} - \rho^2_{\tau\alpha} \right) + \frac{1}{2}\kappa \left(\varepsilon - \varepsilon_{\text{app}}\right)^2, \tag{2.9}$$

where ϵ_{nk} are the eigenvalues of H, μ is the chemical potential, $\boldsymbol{M}_{\tau\alpha}$ is the magnetisation field, $\rho_{\tau\alpha}$ is the charge field, κ is a constant, and ε_{app} is an externally applied strain that shifts the zero of the potential.

The model is solved by minimising the free energy with respect to $\boldsymbol{M}$, ρ and ε self-consistently. For $\varepsilon_{app} = 0$, this leads to the phase diagram shown in Fig. 2.20(a). On cooling from the high-temperature paramagnetic phase, we enter a ferromagnetic phase with the moments aligned along $\boldsymbol{a}$. This is equivalent to the AFM_a phase of $Ca_3Ru_2O_7$, where each ferromagnetic bilayer is stacked antiferromagnetically along the c-axis. On further cooling, we see a

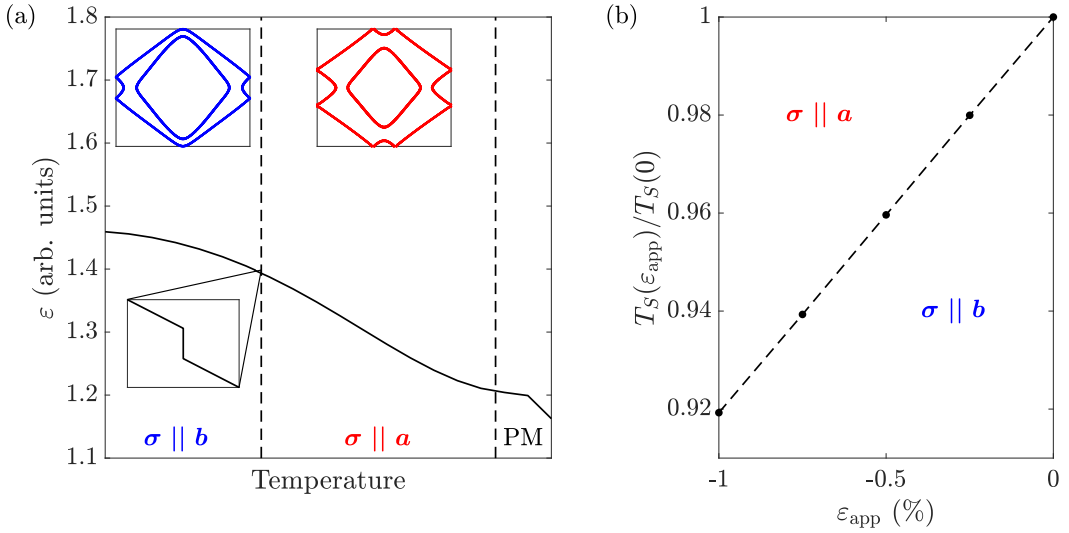

Figure 2.20: (a) Phase diagram of the strain-coupled electronic model, overlaid with the value of the strain field ε. The zoomed region shows a discontinuous jump in ε at the SRT. The insets show the Fermi surfaces calculated in the phases with moments along $\boldsymbol{a}$ (red) and $\boldsymbol{b}$ (blue). (b) The variation in the SRT temperature with applied strain ε_{app}.

gradual increase in the strain field that reduces the energy of the electronic system by enhancing the hopping. At a critical value of the hopping, a first-order transition occurs with discontinuous increases in the strain and magnetisation, at which the moments rotate to point along $\boldsymbol{b}$. The model therefore successfully reproduces the SRT (not withstanding the presence of the mediating cycloid). The model also captures some of the changes in the Fermi surface with temperature [see the insets in Fig. 2.20(a)], which arise from a continuous increase in the magnetisation and Stoner gap, but cannot reproduce the partial gapping at the SRT reported by ARPES [54, 55, 56].

We can validate the model by considering how the lattice parameters of $Ca_3Ru_2O_7$ change with temperature, and linking this to changes in the rotations and tilts of the octahedra. From Fig. 2.8(b), we know that c decreases on cooling through the SRT while a and b increase. The compression along $\boldsymbol{c}$ should lead to an increase in the tilt angle to allow for closer packing of the layers, while the in-plane expansion should lead to a reduction in the rotation angle. From the orbital-overlap argument above, we expect both of these effects to strengthen the hopping on cooling, in agreement with the prediction

of the model. We can therefore understand the temperature-induced SRT in $Ca_3Ru_2O_7$ as being driven by spontaneous lattice strains that arise from feedback with the electronic system and that modulate the hopping.

As well as internal strains, the model can account for externally applied strains. Figure 2.20(b) shows the variation in the SRT temperature with ε_{app}. We see a linear dependence, with negative ε_{app} reducing the hopping and suppressing the SRT, bearing a strong resemblance to the experimental phase diagrams in Fig. 2.17. Again, we can connect ε_{app} to the strain applied in our experiments by considering the changes in lattice parameters. Due to the Poisson ratios, the compression along $\boldsymbol{a}$ or $\boldsymbol{b}$ in our experiments leads to an expansion along $\boldsymbol{c}$, reducing the tilting and therefore hopping. At the same time, the compression along one in-plane direction leads to an expansion along the other, offsetting any change to the rotation angle and explaining why the phase boundaries move the same way for stress applied along $\boldsymbol{a}$ or $\boldsymbol{b}$. Finally, we can account for the faster variation in transition temperature for stress along $\boldsymbol{a}$ than $\boldsymbol{b}$ by appreciating that the former will couple more strongly to the tilts, which are reduced for a compression along $\boldsymbol{a}$ but not along the tilt-axis $\boldsymbol{b}$.

2.4 Conclusion

In this chapter, I have shed new light on the complex SRT in $Ca_3Ru_2O_7$. Rather than a direct transition between the collinear AFM_a and AFM_b phases as previously assumed, I have shown that the reorientation proceeds via an intermediate incommensurate state consisting of a long-range cycloidal modulation of the spins. Detailed scattering studies revealed that, over only a few Kelvin, the envelope of the cycloid evolves smoothly to mediate the SRT. On the basis of symmetry analysis, we can understand this behaviour to arise from the competition between easy-axis anisotropies that promote the collinear phases, and a uniform DMI that is unlocked by the polar lattice symmetry. Measurements under field directly connect the cycloidal order to incommensurate peaks previously attributed to a "metamagnetic texture" [57], offering

a simpler interpretation involving a phase-modulation of the cycloid. We can also make sense of incommensurate structures seen under chemical doping as being variations of the cycloidal order. This unifies previously disparate magnetic behaviours of $Ca_3Ru_2O_7$, attributing them to a common origin and revealing a highly rich phase diagram.

Much of the interest in the SRT of $Ca_3Ru_2O_7$ is based on its possible application in spintronic devices, which requires that it can be controlled by external stimuli. I have shown that strong spin-lattice coupling enables such control with applied anisotropic strain. We utilised commercially-available piezoelectric strain cells [77], integrated into neutron and resonant x-ray scattering facilities, to simultaneously measure the response of the crystal and magnetic structures to uniaxial stress. This offered a detailed understanding of the structure-property relations, and demonstrated a linear dependence of the SRT temperature on applied strain. On the basis of this insight, our collaborators developed a theoretical model in which the variation of the transition temperature is explained by strain-driven changes to the octahedral rotations and tilts that alter the electronic hopping. As well as reproducing our strain data, the model gives an insight into the temperature-induced SRT, which is found to be driven by spontaneous internal strains that arise self-consistently from feedback with the electronic system.

Chapter 3

Probing electron-phonon coupling with resonant inelastic x-ray scattering

The coupling between electrons and phonons is central to a wide range of material properties, and techniques that can measure the strength of this coupling are highly sought-after. Recently, RIXS has received interest as a direct, momentum-resolved probe of electron-phonon coupling (EPC), but a comprehensive theoretical understanding of phonon generation in RIXS is still under development. In this chapter, I present C K-edge RIXS measurements of phonon excitations in graphite, chosen as a simple test material. These high-resolution measurements reveal detailed structure in the multi-phonon features that directly encodes the momentum-dependence of the EPC strength, and which cannot be described by the currently available theoretical models. I describe a Green's-function approach developed by our collaborators to reproduce this structure, revealing contrasting trends of the EPC through the Brillouin zone for electrons close to, and away from, the Fermi level.

3.1 Introduction

EPC is a foundational concept in condensed matter physics, and is responsible for a diverse array of phenomena. A familiar example is the scattering of conduction electrons by thermal lattice vibrations, which gives rise to the linear dependence of resistivity on temperature in simple metals [88]. EPC

can also stabilise collective phases in quantum materials, such as the modulation of electrons in charge density waves [89], or by acting as the glue that binds Cooper pairs in conventional superconductors [90]. In these cases, it is the coupling of phonons to electrons *near* the Fermi surface that is important. There are also a range of out-of-equilibrium situations where the behaviour is determined by the coupling of phonons to electrons *away* from the Fermi surface. Technologically relevant examples include high-temperature heat transport [91], high-field electrical transport [92], phonon-assisted optical transitions [93], and photovoltaics [94].

Given the ubiquity of EPC, it is unsurprising that a number of experimental techniques have been developed to measure its strength. These techniques broadly fall into two categories: those that probe EPC via the lattice degrees of freedom, such as neutron scattering [95], IXS [96], and Raman spectroscopy [97]; and those that measure the electronic band structure, such as angle-resolved photoemission spectroscopy (ARPES) [98]. Each of these techniques has their own strengths and weaknesses. In ARPES, EPC gives rise to kinks in the electron dispersion, and a quantitative determination of the coupling strength requires an estimation of the bare dispersion. ARPES also gives EPC strengths integrated over the phonon momentum. IXS and neutron scattering can resolve the phonon momentum throughout the Brillouin zone, but along with Raman spectroscopy (which gives only zone-centre values) they rely on the broadening of spectral features to determine the EPC. This results in increasing uncertainty with larger coupling strength. Additionally, all of these techniques are unable to access the momentum-resolved coupling of phonons to excited electronic states.

Recently, RIXS has emerged as a new momentum-resolved probe of EPC. The first experimental observation of phonon excitations with RIXS was achieved by Yavas *et al.* in 2010 [99], followed shortly after by a theoretical treatment from Ament *et al.* that showed that the intensity of the phonon peaks is directly related to the EPC strength [100]. Over the fol-

lowing decade, improvements in energy resolution enabled RIXS measurements of EPC on a growing number of topical materials, including cuprates [101, 102, 103, 104, 105, 106, 107], titanates [108, 109, 110], and iridates [111], as well as iridate/titanate heterostructures [112]. It is notable that all of these studies used soft x-rays tuned to the Ti/Cu L or O K absorption edges, which results in a relatively long core-hole lifetime. As I will discuss in the following section, this is because a long lifetime is needed for significant phonon generation in the intermediate RIXS state. The downside of these soft x-ray edges is that the accessible region of reciprocal space is kinematically restricted. Alongside the experimental work, a theoretical understanding of how phonons contribute to the RIXS cross section has steadily advanced [113, 114, 115, 116], although many important issues remain unexplored.

In the following section, I qualitatively describe how phonons are generated in the RIXS process, before briefly covering the main theoretical models used to determine the EPC strength from RIXS spectra. The remainder of the chapter will be dedicated to a C K-edge RIXS study of EPC in graphite, conducted in collaboration with groups from Max Planck Institute for the Structure and Dynamics of Matter, the Diamond Light Source, and Brookhaven National Laboratory. This work demonstrates how, by varying the incident energy, RIXS can access the momentum-resolved EPC for a range of excited electronic states. Our collaborators developed a new theoretical model to account for previously overlooked aspects of phonon generation in RIXS, allowing us to constrain the EPC throughout the Brillouin zone and circumvent the restricted momentum transfer at the C K edge. Our results raise important issues that must be considered in future RIXS studies of EPC.

3.2 Phonon generation in the resonant inelastic x-ray scattering process

To ground our discussion of the theoretical treatments in the next section, we first need to understand how phonons are generated in RIXS. Figure 3.1

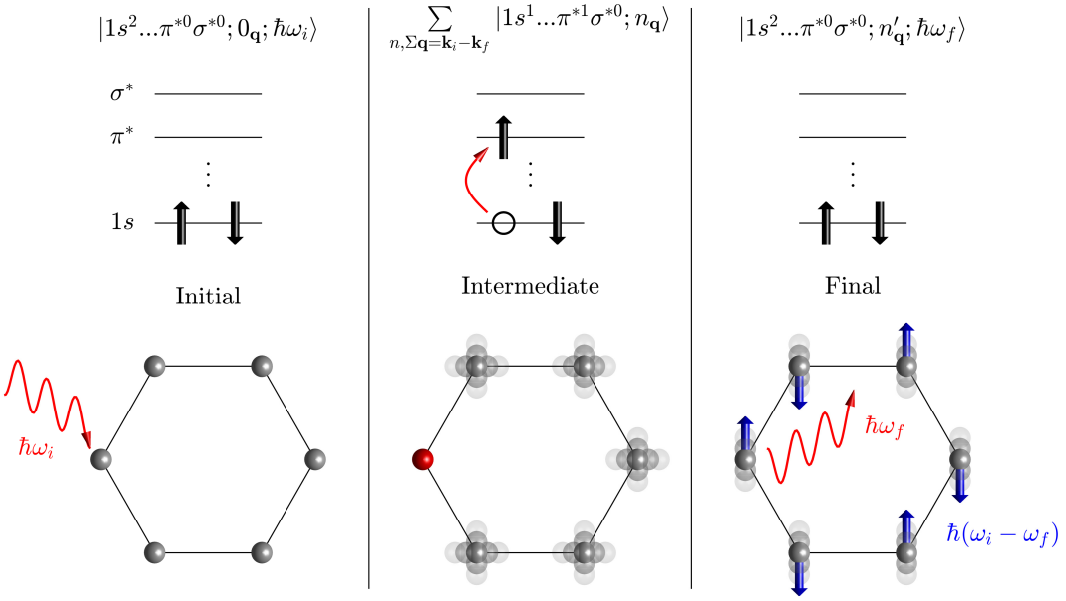

Figure 3.1: Cartoon of phonon generation in the RIXS process at the C K edge of graphite. The process is broken down into three states – initial, intermediate, and final – for each of which is shown a schematic wavefunction (top), electronic orbital structure (middle), and real-space representation of the crystal (bottom). Only the $1s$, σ^* and π^* orbitals are shown for clarity. The incident (final) photon energy is denoted by $\omega_{i(f)}$, and $n_{\boldsymbol{q}}$ denotes the number of phonon modes of wavevector $\boldsymbol{q}$. The zone-centre TO mode is depicted in the real-space representation of the final state [117].

shows a cartoon of the RIXS process at the C K edge. In the initial state, an x-ray photon is incident on a graphite ion in its electronic ground state, and there are no phonons present. Depending on the energy, ω_i, of the incident photon, an electron is excited from the $1s$ to the π^* or σ^* orbitals, where it experiences a partially screened potential from the resulting core hole. The altered charge density in the intermediate state then perturbs the positions of the surrounding ions. This local deformation of the lattice can be seen as a sum of phonon modes $n_{\boldsymbol{q}}$. Finally, the excited electron relaxes to fill the core hole through the emission of a photon of energy ω_f, leaving $n'_{\boldsymbol{q}}$ well-defined phonons of total energy $\omega_i - \omega_f$ in the final state.

A few important facts are apparent from this description. Firstly, as lattice deformation is a relatively slow process compared to electronic transitions, a long intermediate-state lifetime is required for significant phonon generation.

Secondly, the charge density in the intermediate state, and therefore which phonon modes are excited, will depend on which orbital the core electron is excited into. Thirdly, as the core hole is not necessarily fully screened in the intermediate state, it can also contribute to phonon generation, such that the phonons present in the final state reflect the EPC of both the excited electron and core hole [114]. Finally, while the final state contains a few well-defined phonon quasiparticles, the intermediate state contains a superposition of a large number of different phonon modes of varying momenta. These features will be important for our interpretation of the experimental data later in this chapter.

3.2.1 Existing theoretical models

The theoretical model employed in most experimental work on phonons in RIXS to date was developed by Ament *et al* [100]. A major factor in its popularity is its simplicity: it considers a single Einstein (i.e. non-dispersive) phonon mode coupled to an isolated electronic state, producing an analytical expression for the RIXS cross section. Here, I will briefly outline the main features of the model, and refer the reader to Ref. [100] for more detail.

We start with the basic Holstein Hamiltonian describing the isolated electronic state and Einstein phonon, with a linear coupling between them

$$H = \epsilon d^\dagger d + \omega b^\dagger b + G d^\dagger d \left(b^\dagger + b\right), \tag{3.1}$$

where $d^\dagger$ (d) creates (annihilates) an electron of energy ϵ, $b^\dagger$ (b) creates (annihilates) a phonon of energy ω, and G is the EPC strength. This Hamiltonian can be diagonalised by the Lang-Firsov canonical transformation

$$\bar{H} = e^S H e^{-S} = \omega b^\dagger b - \frac{G^2}{\omega}, \tag{3.2}$$

where $S = (G/\omega) d^\dagger d (b^\dagger - b)$. We are therefore left with a simple diagonal bosonic Hamiltonian, $\bar{H}$, with eigenstates $|n\rangle$ and energies $E_n = n\omega - (G^2/\omega)$ corresponding to n phonon excitations.

We know from Sec. 1.2.3 that the RIXS amplitude is given by the Kramers-Heisenberg equation

$$A = \sum_n \frac{\langle f|\mathcal{D}|n\rangle \langle n|\mathcal{D}|i\rangle}{\omega_i - E_n + i\Gamma}, \tag{3.3}$$

for initial state $|i\rangle$ with zero energy, intermediate states $|n\rangle$ with energies E_n and lifetimes $1/\Gamma$ (which are taken to be equal), and final state $|f\rangle$. As we only have a single isolated electronic level, we can ignore any dependence of the dipole operators $\mathcal{D}$ on position, momentum or polarisation, leaving them to simply create and then destroy an electron-hole pair: $\mathcal{D} = d^\dagger h + dh^\dagger$. Applying the canonical transformation to $\mathcal{D}$, and assuming no phonons in the initial state and n_f in the final state, gives

$$\begin{aligned} A_f &= \sum_n \frac{\langle n_f|e^{-S}|n\rangle \langle n|e^{S}|0\rangle}{\omega_i - n\omega + (G^2/\omega) + i\Gamma} \\ &= \sum_n \frac{B_{\max(n_f,n),\min(n_f,n)}(g) B_{n,0}(g)}{\omega_i + \omega(g-n) + i\Gamma}, \end{aligned} \tag{3.4}$$

where the dimensionless coupling constant $g = (G/\omega)^2$ and the Frank-Condon factors $B_{m,n}(g) = (-1)^m \sqrt{e^{-g} m! n!} \sum_{l=0}^{n} \frac{(-g)^l g^{(m-n)/2}}{(n-l)!l!(m-n+l)!}$. Eq. (3.4) describes a series of peaks in the RIXS spectrum at integer multiples n_f of the phonon energy ω and with decreasing amplitudes A_f, each representing the excitation of n_f phonons, as shown in Fig. 3.2(a).

Provided that the intermediate-state lifetime is known, Eq. (3.4) can be used to extract the EPC strength G from a RIXS spectrum. As the absolute RIXS intensity cannot generally be determined, this is usually achieved by calculating the relative intensities of successive phonon peaks. Where a low resolution or short intermediate-state lifetime prevents the accurate measurement of the multi-phonon peaks, an alternative method proposed by Rossi *et al.* can be used [104]. Here, the intensity of the one-phonon peak is tracked on detuning the incident x-ray energy ω_i from the resonance (here taken as $\omega_i = 0$). As shown in Fig. 3.2(b), the rate of fall-off of intensity with detuning changes as a function of EPC strength, and so can be used to determine G

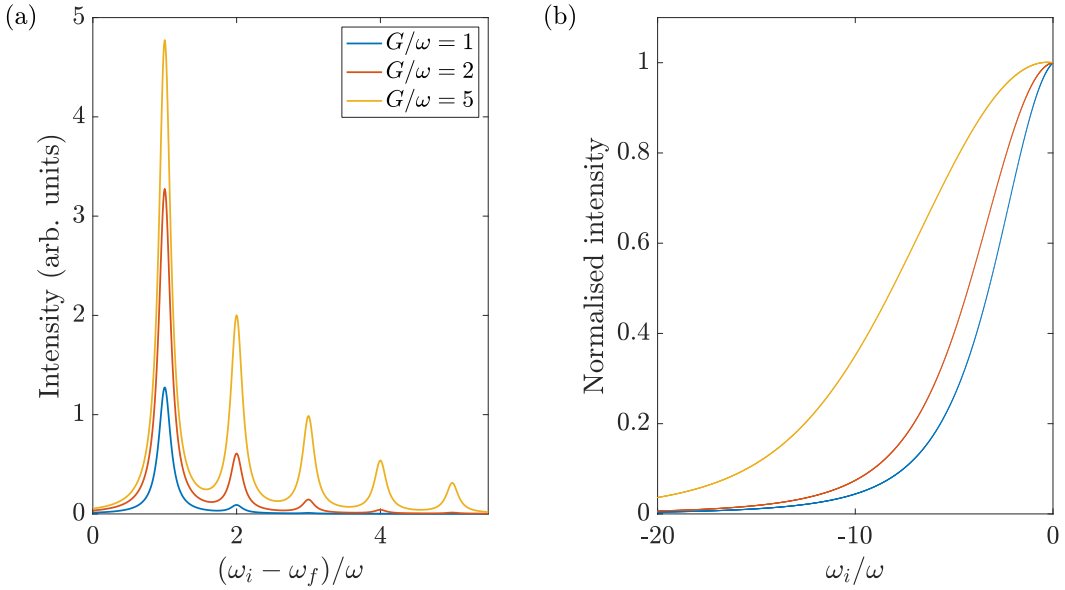

Figure 3.2: (a) RIXS spectra calculated with the Ament model for $\Gamma/\omega = 5$ at a range of EPC strengths. Each phonon peak has a Lorentzian lineshape with full width at half maximum $\omega/10$. (b) Intensity of the one-phonon peak as a function of detuning below the resonance, normalised to the intensity at zero detuning. The colours correspond to those in (a).

through comparison with Eq. (3.4).

The Ament model provides a simple analytical expression for the cross section that allows the EPC to be easily extracted from experimental data, resulting in its use in many studies to date [108, 109, 112, 104, 111, 105, 110, 106, 107, 118]. Its simplicity is a double-edged sword, however, and it must be ensured that the approximations involved are appropriate for the experimental situation at hand. Its validity is questionable, for example, when more than one phonon mode has appreciable coupling, when the phonon mode of interest has a significant dispersion, or when the excited electron in the intermediate RIXS state is mobile. In an attempt to generalise the Ament model, Geondzhian and Gilmore have recently extended it to include a second phonon mode, and allowed the excited-state potential energy surface to vary from that of the ground state, while still retaining exact analytical solutions [115]. The first of these extensions will be employed in Chapter 4.

The notable exception to the use of the Ament model in the literature is for the quasi-1D cuprates, whose electronic structures are not well approximated

as a single localised level. For these systems, exact diagonalisation calculations on small clusters have been employed [101, 102, 103]. These calculations capture the specific features of the system under study, but are obviously not generalisable like the Ament model. Due to computational restrictions on the size of the Hilbert space, they are also limited to low-dimensional systems and phonon modes with simple (and known) displacement patterns. As with the Ament model, the cluster calculations cannot treat dispersive phonons or EPC strengths. To address this issue, Devereaux *et al.* instead used a diagrammatic approach to calculate the cross section in an eight-band model of the cuprates [113]. This approach allowed them to account for electronic itinerancy, phonon dispersion, a momentum-dependent EPC strength, and matrix element effects, giving a detailed prediction of which phonon modes will have significant RIXS intensity at which momenta. Due to their complexity, however, the calculations were limited to single-phonon processes.

3.3 Electron-phonon coupling in graphite

This section presents a RIXS study of the EPC in graphite, chosen as a simple model system. The measurements demonstrate the power of RIXS to probe the coupling of phonons to distinct electronic states: the π^* state near the Fermi level, and the σ^* state well above it. At the resonances associated with these two states, we find qualitatively different multi-phonon excitations in our RIXS spectra, showing a stark difference in the phonon momenta to which they couple. This behaviour cannot be adequately described by the current theoretical approaches, prompting the development of a new model using Green's functions to account for multiple dispersive phonons in both the intermediate and final RIXS states. The model accurately reproduces our experimental spectra at both resonances, revealing distinct momentum-dependences of the EPC for the two electronic states.

The work presented in this section has been published as C. D. Dashwood *et al.*, Phys. Rev. X **11**, 041052 (2021) [119]. The RIXS measurements were

performed by me, James Vale, Alex Pakpour-Tabrizi, Chris Howard, Quentin Faure and Larissa Veiga, with Andrew Walters and Abhishek Nag as local contacts. Data analysis was performed by me and Andrey Geondzhian, and overseen by Mark Dean and Des McMorrow. The Green's-function–based theoretical model was developed by Andrey Geondzhian and Keith Gilmore.

3.3.1 Experimental details

Our RIXS measurements were performed at beamline I21 of the Diamond Light Source. A natural graphite single crystal was mounted such that the scattering plane is $(h, 0, l)$, and cleaved in vacuum. We chose an energy resolution of 47 meV (determined from scattering from amorphous carbon tape mounted next to the sample) to ensure sufficient throughput. All RIXS spectra were taken with linear horizontal (π) incident x-ray polarisation, at a temperature of 20 K, and with a counting time of 20 min. X-ray absorption spectra (XAS) in total electron yield were obtained by measuring the sample drain current. Data for energies around the π^* resonance were taken with grazing-incident x-rays ($\theta = 20°$) while data around the σ^* resonance were taken with normal-incident x-rays ($\theta = 90°$) in order to maximise the intensity of the phonon features. At the soft x-ray energies of the C K edge, the momentum transfer is confined to a small in-plane region of < 0.1 r.l.u. around the zone centre. We used a fixed scattering angle of $2\Theta = 154°$, resulting in the momentum transfer varying slightly with incident energy. Around the π^* resonance the momentum transfer $\boldsymbol{q} = (0.0802 \pm 0.0004, 0, 0.164 \pm 0.001)$, while around the σ^* resonance $\boldsymbol{q} = (0.0220 \pm 0.0002, 0, 0.300 \pm 0.002)$. All data have been corrected for incident flux and self-absorption, the latter of which introduces minimal changes to the normalised spectra that do not affect our analysis or conclusions.

Graphite is a favourable material for this study for several reasons. It has two well-defined excitations to the low-energy π^* and high-energy σ^* states at the C K edge, both of which couple most strongly to optical phonons with energies above 0.15 eV that are well resolved by our 47 meV-resolution measurements. There are no other low-energy excitations, such as magnons,

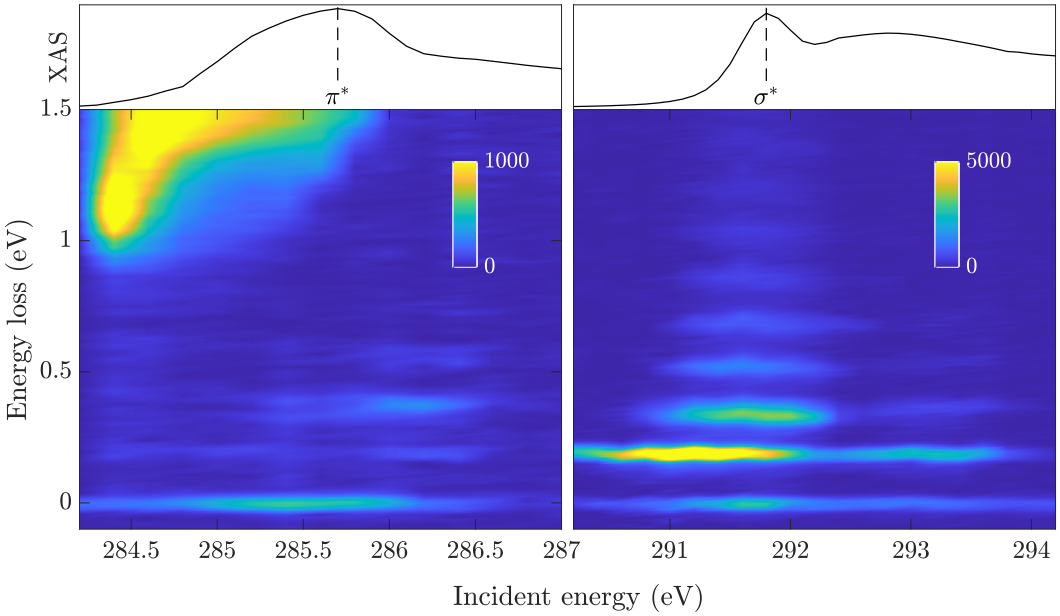

Figure 3.3: RIXS maps around the π^* and σ^* resonances, with the XAS above for reference (the dashed vertical lines in the XAS mark the peaks of the resonances at 285.6 eV and 298.1 eV respectively). Both maps show a series of phonon features above the elastic line, with the contrasting resonance behaviour most apparent for the two-phonon feature between 0.3 eV to 0.4 eV. The intense feature above ∼1 eV in the π^* map arises from electronic transitions.

that could obscure the phonon harmonics. Graphite also has a relatively simple electronic and crystal structure, facilitating calculations, and the EPC close to the Fermi level is well studied [120, 121, 118] allowing us to validate our results for the π^* states.

3.3.2 Resonant inelastic x-ray scattering measurements

Our measurements are summarised in two RIXS maps around the π^* (285.6 eV) and σ^* (291.8 eV) resonances, shown in Fig. 3.3. Above the elastic line at zero energy loss, both maps show a series of features of decreasing intensity that are reminiscent of the harmonic progression of phonon excitations predicted by the Ament model [see Fig. 3.2(a)]. These features are more intense in the σ^* map, and in both the first feature above the elastic line appears to resonate at a slightly lower incident energy than those above it.

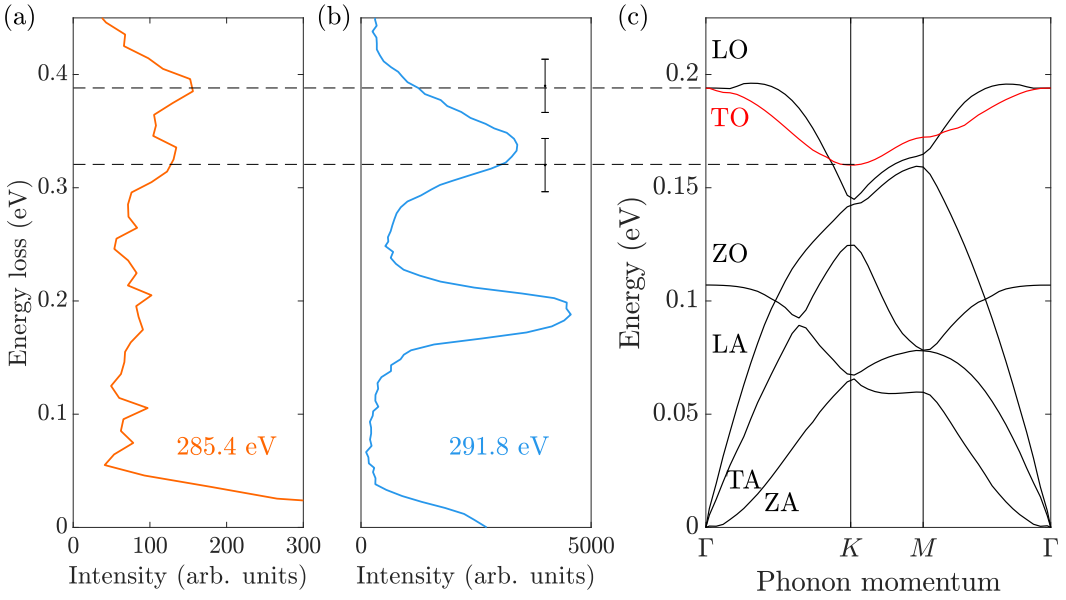

Figure 3.4: Experimental RIXS spectra at (a) 285.4 eV and (b) 291.8 eV, alongside (c) the phonon dispersion of graphite from Ref. [117] scaled to half the energy range of (a) and (b). The horizontal dashed lines mark (twice) the energies of the TO mode at Γ and K, and the vertical error bars show the instrumental energy resolution.

We can assign the phonon modes contributing to the RIXS maps based on the known phonon dispersion of graphite, shown in Fig. 3.4(c). The energy loss of the first peak, at ∼0.19 eV in both maps, allows it to be attributed to the degenerate zone-centre transverse and longitudinal optical (TO and LO) phonon modes [117] whose displacement pattern is shown in the final state in Fig. 3.1. In the purely local picture advanced by the Ament model, successive peaks would then correspond to higher harmonics of this first peak spaced at equal energy intervals. The next feature is not at double the fundamental energy, however, and shows a markedly different structure between the two maps. At the π^* resonance there is an additional peak split off below the second harmonic, while at the σ^* resonance a single broader peak is visible.

The differences in the two-phonon features can be seen more clearly in Fig. 3.4(a) and (b), which show individual spectra near the π^* and σ^* resonances respectively. These are plotted alongside the phonon band structure in Fig. 3.4(c), scaled such such that the phonon energies line up with twice the energy loss of the RIXS spectra. From this comparison, it is clear that the

two peaks in the split feature of the π^* spectrum occur at twice the energies of transverse optical (TO) phonons at Γ and K, while the broad asymmetric feature of the σ^* spectrum spans twice the bandwidth of the TO mode. Taking into account the 47 meV experimental energy resolution, it appears that contributions from the lower-energy acoustic (ZA, TA, and LA) and out-of-plane optical (ZO) modes are negligible, while the longitudinal optical (LO) mode can only have significant contributions when it is nearly degenerate with the TO mode. We therefore focus only on the TO mode going forward.

Our preceding analysis suggests that phonons of different momenta are excited at each of the resonances. Although not identified in any previous RIXS studies, contributions to the multi-phonon features from phonons at multiple momenta can be generally expected. To conserve momentum, a single-phonon excitation can include only a mode at the experimental momentum transfer in the final state. The final states of a multi-phonon feature, however, can conceivably consist of phonons at any point in the Brillouin zone, so long as their momenta sum to the experimental momentum transfer. This is consistent with our analysis, where the two-phonon feature of an approximately zone-centre spectrum has contributions from phonons at $+K$ and $-K$.

Although allowed by momentum conservation, we still do not understand why phonons of different momenta couple to the π^* and σ^* states. To answer this, we need to recall from Sec. 3.2 that the composition of the intermediate electronic state in the RIXS process determines which phonon modes are excited. In this case, both resonances excite electrons from the same $1s$ state, so the core hole cannot explain the difference between the spectra. We instead focus on the band structure of the excited electron, shown in Fig. 3.5(a). For electrons excited into the low-energy π^* states, the steepness of the bands confines them to a small region around the Dirac points at K. These states can only interact with phonons of momenta close to Γ, which scatter electrons within a single Dirac cone, or K, which scatter electrons between different Dirac cones. By contrast, the high-energy σ^* bands are flatter and electrons

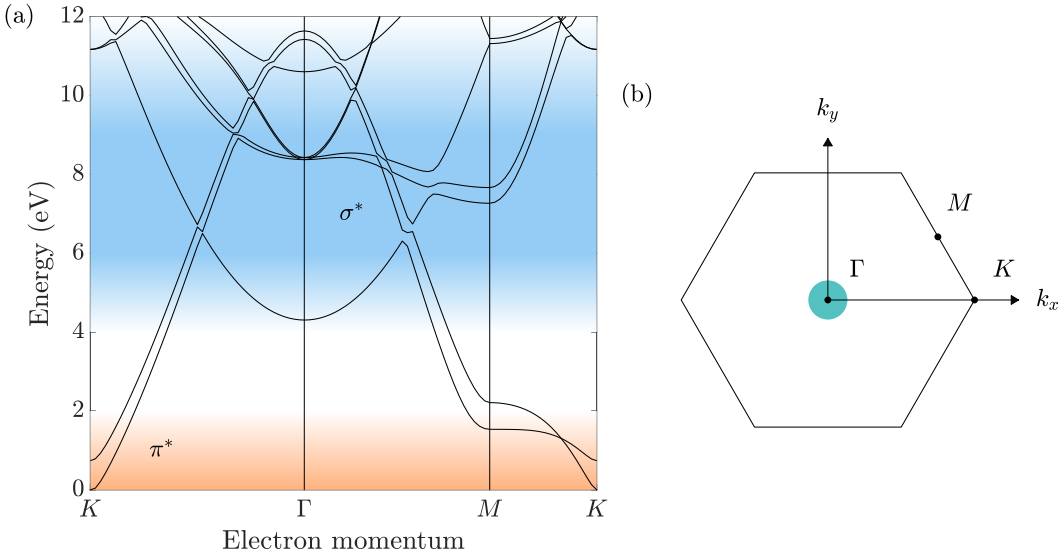

Figure 3.5: (a) Electronic band structure of graphite from Ref. [122], with the low-energy π^* bands shaded in orange and the high-energy σ^* bands in blue. (b) The 2D-projected Brillouin zone of graphite, with the momenta accessible in our RIXS measurement indicated by the turquoise circle, and high symmetry positions Γ, K, and M marked.

excited into them can span the Brillouin zone, suggesting interactions with a wide range of phonon momenta. This provides an intuitive understanding of our earlier assignment of the RIXS features, where the split two-phonon feature at the π^* resonance is dominated by phonons at Γ and K, while the single broad feature at the σ^* resonance has contributions from across the TO mode dispersion.

3.3.3 A Green's function model of phonons in resonant inelastic x-ray scattering

To model our data, we clearly need to account for multiple phonons of different momenta in both the intermediate and final RIXS states. Within the exact-diagonalisation approaches discussed in Sec. 3.2.1, the explicit summation over all possible intermediate states leads to a computationally-intractable expansion of the Hilbert space for dispersive phonons. While the diagrammatic approach of Devereaux *et al.* does allow dispersive phonons [113], it similarly becomes unwieldy for anything above one-phonon processes and so cannot describe the rich behaviour we have found in the multi-phonons peaks. To

avoid these issues, our collaborators extended a Green's-function approach that they previously applied to small molecules [114] to treat the full momentum-dependence of phonons in a crystalline lattice. The benefit of this approach is that vibronic effects in the intermediate state can be accounted for implicitly, avoiding the need to sum over intermediate states.

Here, I will briefly outline the main features of the model (see Refs. [119] and [114] for a full treatment). The intermediate electronic state, including electron-electron and electron-phonon interactions, is represented by an effective quasi-particle exciton Green's function. On expanding the interacting Green's function in a time series, there are two important types of diagrams: closed-loop diagrams where a phonon gets created and then destroyed, and those where the created phonons remain and give rise to the final-state population. The former correspond to intermediate-state phonons, which are accounted for using the cumulant representation of the Green's function. As there are generally only a few phonon harmonics visible in a RIXS spectrum, the latter type of diagram is treated explicitly. In principle, the gapless band structure of graphite [Fig. 3.5(a)] allows final states involving low-energy electronic excitations, which would be expected form a continuum in our RIXS spectra. As no such continuum is seen above the background in our data, however, the cross section of these electronic excitations (as well as higher-order excitations involving both phonons and electrons) must be vanishingly small and can be neglected.

Omitting RIXS matrix elements, which affect only the absolute magnitude, the energy- and momentum-dependent RIXS cross section can be written as

$$\sigma(\omega_i, \omega_f, \boldsymbol{q}) \propto -\sum_n |\Lambda^n(\omega_i, \boldsymbol{q})|^2 \Im D^n(\omega_i - \omega_f, \boldsymbol{q}), \tag{3.5}$$

where the sum is over the n final-state phonons. $\Lambda^n(\omega, \boldsymbol{q})$ is the complex off-diagonal part of the exciton Green's function, representing the scattering of the exciton by n phonons of total momentum $\boldsymbol{q} = \boldsymbol{k}_i - \boldsymbol{k}_f$. The presence of phonons in the final state is reflected by the many-body Green's function

$D^n(\omega, \boldsymbol{q})$, which in the limit of infinite phonon lifetime becomes $\Im D^n(\omega, \boldsymbol{q}) = -\frac{1}{\pi}\delta(\omega - \sum_j \omega_j)\delta(\boldsymbol{q} - \sum_j \boldsymbol{q}_j)$. Phonon-phonon interactions are captured by adding a small lifetime broadening to D.

Approximate expressions for Λ^n have previously been given in the limits of weak [113] and moderate [114] EPC. Here, however, both the π^* and σ^* states can be treated as localised excitons over the intermediate-state lifetime of graphite [123], allowing a closed-form expression for Λ with linear EPC. Although the cross section in Eq. (3.5) is given in the energy domain, from here on we use the time-dependent form

$$\Lambda^n(t, \boldsymbol{q}) = \frac{\Lambda^0(t)}{\sqrt{n!}} \prod_{j \ldots n} \left[iG(\boldsymbol{q}_j) \int_0^t D^{>}(\tau, \boldsymbol{q}_j) d\tau \right], \tag{3.6}$$

where Λ^0 is the diagonal part of the exciton Green's function (the same dressed propagator that appears in the cross section for XAS), $G(\boldsymbol{q})$ is the momentum-dependant EPC strength, and the greater phonon propagator in the zero-temperature limit is $D^{>}(t, \boldsymbol{q}) = -i \langle b_{\boldsymbol{q}}(t) b^{\dagger}_{\boldsymbol{q}}(0) \rangle = i\theta(t) e^{-i\omega(\boldsymbol{q})t}$ where θ is the Heaviside step function. The bracketed part of Eq. (3.6) represents the phonon contributions to the scattering diagram, with the product over n phonons conserving momentum $\boldsymbol{q} = \boldsymbol{q}_1 + \ldots + \boldsymbol{q}_n$. In the limit of localised excitons, Eq. (3.6) accounts for all types of diagrams including those with vertex corrections.

The exciton propagator dressed by the exciton-phonon interaction can be expressed as $\Lambda^0(t) = L(t)e^{C(t)}$, where L is the bare exciton Green's function and C is the cumulant function. The exciton lifetime is captured by including a damping factor $e^{-\Gamma t/2}$ in L (note that this expression contains *half* of the inverse lifetime [115]). X-ray photoelectron spectroscopy measurements give a value $\Gamma/2 = 0.1\,\mathrm{eV}$ [124], but this does not account for the presence of the excited electron in RIXS that will shorten the lifetime. We therefore chose an approximate value $\Gamma/2 = 0.15\,\mathrm{eV}$ which best reproduces our experimental spectra at both resonances.

Finally, the cumulant function to second order in the exciton-phonon in-

teraction can be written

$$C(t) = [L(t)]^{-1} \int_0^t \int_0^t L(t-\tau_1)\Sigma_{\mathrm{FM}}(\tau_1-\tau_2)L(\tau_2)d\tau_1 d\tau_2, \tag{3.7}$$

where the Fan-Migdal self-energy is $\Sigma_{\mathrm{FM}} = -i\sum_{\boldsymbol{q}} G(\boldsymbol{q})^2 L(t) D(t,\boldsymbol{q})$. Substituting the exciton and phonon Green's functions, and taking the time integrals in Eq. (3.8) analytically [125], we find

$$C(t) = \sum_{\boldsymbol{q}} \frac{G(\boldsymbol{q})^2}{\omega(\boldsymbol{q})^2 N}(e^{-i\omega(\boldsymbol{q})t} + i\omega(\boldsymbol{q})t - 1). \tag{3.8}$$

Here, the summation over $\boldsymbol{q}$ encompasses the entire Brillouin zone without restriction, as the total momentum transfer of the contributing diagrams is zero. Therefore, for any final state configuration, there are contributions to the cross section from intermediate-state phonons of all momenta. While we knew that phonons of different momenta could contribute to the multi-phonon peaks, Eq. (3.8) shows that even the intensity of the one-phonon peak depends on $G(\boldsymbol{q})$ throughout the Brillouin zone, not just at the experimental $\boldsymbol{q}$ point. The importance of this point will be demonstrated in Sec. 3.3.6.

To evaluate Eq. (3.8), we used the TO phonon dispersion calculated with density functional perturbation theory, which is in good agreement with previous IXS measurements [117]. Given the weak inter-layer coupling of graphite, the optical phonon modes of interest have a minimal dependence on the out-of-plane momentum [117] and we can safely restrict our analysis to the 2D-projected Brillouin zone. Reciprocal-space integrations were performed using a reduced set of weighted momentum points that reflect the symmetries of the graphite structure [126]. Having calculated the terms in Eq. (3.6) in the time domain, we perform a Fourier transform at a given incident photon energy and plug it into Eq. (3.5) to obtain the RIXS cross section. The only free parameter of the model is then the momentum-dependent EPC strength, $G(\boldsymbol{q})$, which is obtained by fitting the experimental RIXS spectra.

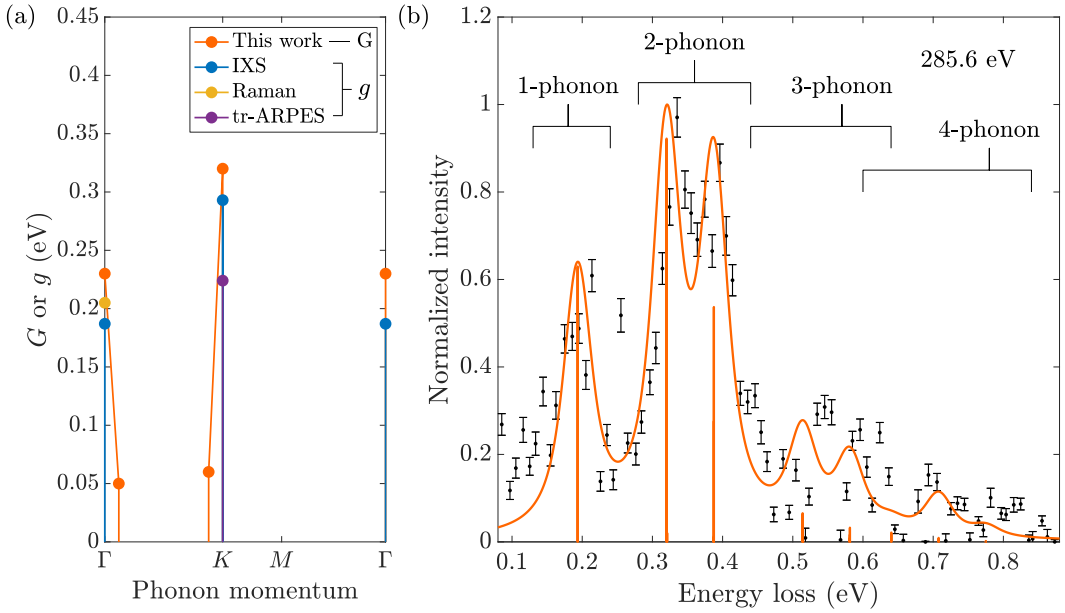

Figure 3.6: (a) Modelled momentum dependence of G at the π^* resonance (orange), compared to g determined by IXS (blue) [96], Raman spectroscopy (yellow) [97] and time-resolved ARPES (purple) [121]. (b) Normalised experimental (black points with error bars) and calculated (orange line, including experimental broadening) RIXS spectra at the π^* resonance. The contribution from each phonon generation process is indicated by the vertical orange lines, grouped above by the number of phonons.

3.3.4 Electron-phonon coupling for low-energy π^* states

We first apply our model to the π^* data. For electrons close to the Fermi level, a number of other techniques [96, 97, 121], as well as our arguments in Sec. 3.3.2, give the EPC as being significant only in small regions around the Γ and K points of the Brillouin zone. We therefore include a minimal set of momenta within our model: the Γ and K points, the experimental in-plane momentum transfer $\boldsymbol{q}_{\text{exp}} \approx (0.08, 0.00)$, and $K - \boldsymbol{q}_{\text{exp}}$. Inclusion of the latter two points effectively captures the width over which the EPC falls off away from the high-symmetry points. The intensity of the one-phonon peak depends strongly on the EPC strength at $\boldsymbol{q}_{\text{exp}}$, while the multi-phonon features are not significantly affected by the fact that $\boldsymbol{q}_{\text{exp}} \neq \Gamma$.

Figure 3.6(b) shows a fit of our model to the spectrum on resonance,

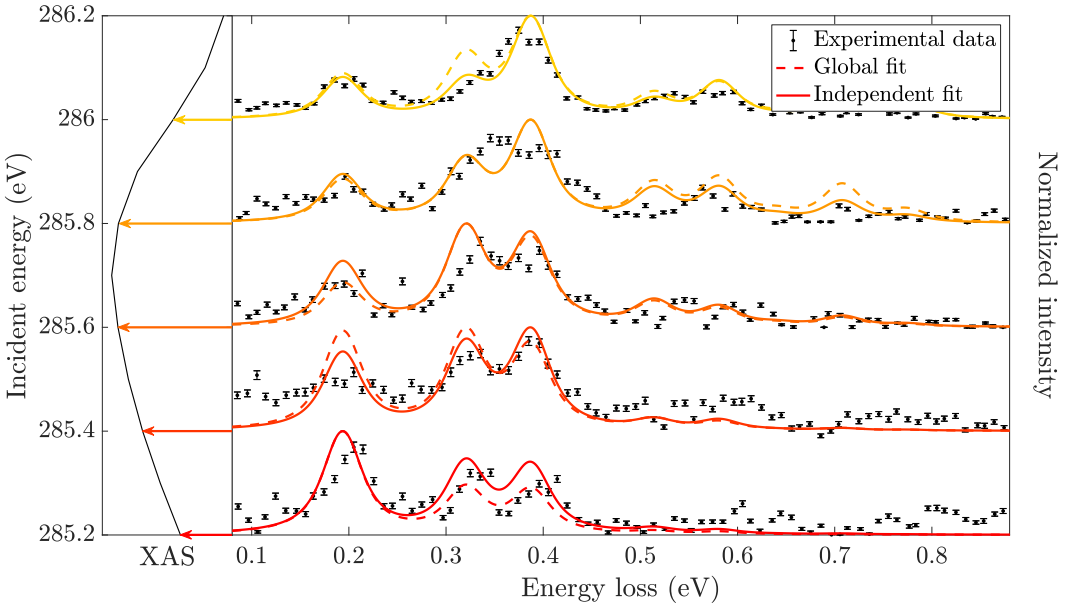

Figure 3.7: Incident-energy dependence of the experimental spectra (black points with error bars) around the π^* resonance, overlaid with spectra calculated using a global fit of EPC strengths (red to orange dashed lines) and using EPC strengths fitted to the experimental spectrum at that particular energy (red to orange solid lines).The spectra are plotted alongside the XAS, with arrows indicating the incident energies.

with the corresponding momentum dependence of $G(\boldsymbol{q})$ plotted in Fig. 3.6(a). Despite the small set of included momentum points, good agreement between the experimental and calculated spectra can be seen, including the striking splitting of the two-phonon feature. This confirms that the splitting arises due to the dominant contributions from pairs of phonons at K and Γ, indicated by the vertical lines at 0.32 eV and 0.39 eV respectively. Intensity above 0.45 eV can be accounted for by overlapping three- and four-phonon processes, which are also made up of contributions from pairs of $\pm K$-momenta phonons with additional Γ modes.

We also tested our model on detuning the incident x-ray energy away from the maximum of the XAS. For incident energies below the resonance, the composition of the intermediate RIXS state should not differ significantly from that on resonance, and we would therefore expect to be able to reproduce the experimental spectra using a fixed $G(\boldsymbol{q})$. As the incident energy is raised through the upper tail of the XAS peak, however, the composition of the

G (eV)	$\boldsymbol{q} = \Gamma$	$\boldsymbol{q} = \boldsymbol{q}_{\text{exp}}$	$\boldsymbol{q} = K - \boldsymbol{q}_{\text{exp}}$	$\boldsymbol{q} = K$
Global fit	0.23	0.05	0.06	0.32
285.2 eV	0.24	0.05	0.13	0.30
285.4 eV	0.24	0.05	0.07	0.30
285.6 eV	0.23	0.07	0.07	0.32
285.8 eV	0.20	0.05	0.05	0.28
286.0 eV	0.24	0.05	0.12	0.27

Table 3.1: $G(\boldsymbol{q})$ extracted from global and independent fits to RIXS spectra around the π^* resonance.

intermediate electronic state will change [127]. From Fig. 3.5(a) we can see that electrons excited higher into the π^* bands can move towards the M points, for instance. This in turn allows scattering by phonons of different momenta, changing the momentum-dependence of G.

These expectations are borne out by a comparison between our experimental and calculated spectra at energies through the π^* resonance, shown in Fig. 3.7. Below 285.6 eV there is good agreement between the experimental and calculated spectra, with the persistent splitting of the two-phonon feature and the changing relative intensities of the one- and two-phonon features all captured well by our model. The non-monotonic energy dependence of the intensities, including the offset of the maximum of the one-phonon peak intensity from zero-detuning [118], arises from a combination of strong EPC and long core-hole lifetime [115]. To confirm the robustness of the extracted values of the EPC strength below the resonance, two calculated spectra are shown at each energy: one using a global fit of $G(\boldsymbol{q})$, and the other using $G(\boldsymbol{q})$ fitted to each spectrum individually. The difference between the calculated spectra are comparable to the noise level of the data, and the extracted EPC strengths (see Table 3.1) all follow the same trend $G(K) > G(\Gamma) >> G(K - \boldsymbol{q}_{\text{exp}}) \geq G(\boldsymbol{q}_{\text{exp}})$. Above 285.6 eV, by contrast, neither fit is able to capture accurately the profile of the two-phonon peak, suggesting the need to incorporate additional momentum points into the parameterisation of $G(\boldsymbol{q})$.

We can now compare our results with those from other techniques. Alongside our best-fit $G(\boldsymbol{q})$, Fig. 3.6(a) also shows the EPC strengths determined

by IXS [96] and Raman spectroscopy [97], as well as a novel time-resolved ARPES technique [121]. We see reasonable agreement between all the techniques. Note, however, that we use a lower-case g for the coupling probed by these other techniques, in contrast to the capital G for the coupling probed by RIXS. This is to highlight that RIXS involves a core hole not present in the other techniques, which can contribute to phonon generation when it is poorly screened. Further work, likely involving first-principles calculations, is needed to determine the strength of hole-phonon coupling and directly relate G to g. While g is the quantity of interest for equilibrium phenomena, I note that G is directly relevant for many technologically-important out-of-equilibrium situations for which RIXS is the ideal probe.

By modelling the contributions to the multi-phonon features, we have determined the interactions between π^* electrons and TO phonons throughout the Brillouin zone, all from a single zone-centre spectrum. This method will be invaluable, as the soft x-ray edges at which phonons are enhanced (due to the long intermediate-state lifetimes), and energy resolutions are maximised, also suffer from restricted momentum transfer [see Fig. 3.5(b)]. Figure 3.6(a) shows that RIXS can provide more detail on the momentum structure of the EPC than many of the established techniques, in this case giving the distance over which G falls off away from the high symmetry points. An even more detailed parameterisation of $G(\boldsymbol{q})$ could be refined against multiple spectra at different momentum transfers.

3.3.5 Electron-phonon coupling for high-energy σ^* states

Having verified our methodology at the π^* resonance, we now come to the high-energy σ^* states. Here, our earlier analysis of both the profile of the two-phonon feature, and of the intermediate electronic state, suggests a finite and gradually varying $G(\boldsymbol{q})$ over a wide range of momenta. In order to constrain our parameter space, we therefore assume a linear dependence between the high-symmetry points Γ, K, and M. The more uniform variation of G also

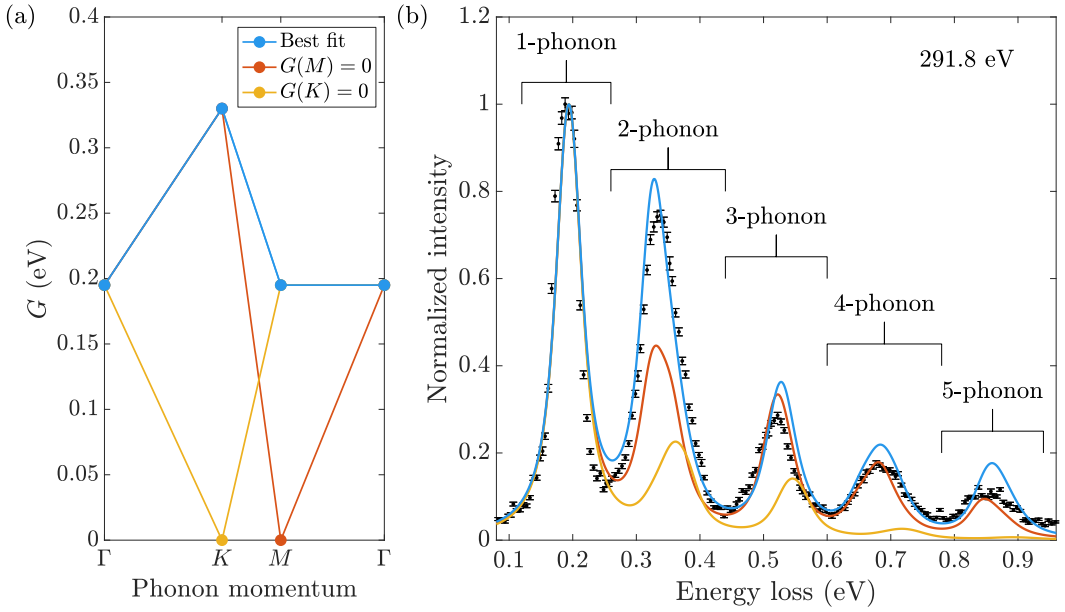

Figure 3.8: (a) Best-fit momentum dependence of G at the σ^* resonance (blue), and that with $G(M) = 0$ (orange), and $G(K) = 0$ (yellow). (b) Normalised experimental (black points with error bars) and calculated [blue, orange, and yellow lines, corresponding to those in (a)] RIXS spectra at the σ^* resonance. The contribution from each n-phonon process is labeled above.

allows us to approximate $\boldsymbol{q}_{\text{exp}} \approx \Gamma$ in our calculations.

Figure 3.8(a) shows the best-fit dispersion of the EPC, which we find to be significant at all of the high-symmetry points. The resulting spectrum on resonance is shown in Fig. 3.8(b), and again we see that a simple parameterisation of $G(\boldsymbol{q})$ is able to describe the experimental data well. Unlike the splitting seen at the π^* resonance, here our model reproduces the subtle broadening and asymmetry of the two-phonon feature, confirming that these characteristics arise from the varying contributions of pairs of opposite-momenta phonons which disperse gradually through the Brillouin zone.

In order to determine the uniqueness of our fit, we also show spectra in Fig. 3.8(b) calculated with $G(M) = 0$ and $G(K) = 0$ [note that a finite $G(\Gamma)$ is needed to reproduce the intensity of the one-phonon peak]. We can see that the calculated spectra are most sensitive to the value of $G(K)$, which strongly influences the intensities of all the multi-phonon peaks. While the value of $G(M)$ has little impact on the three-, four- and five-phonon peaks, we see

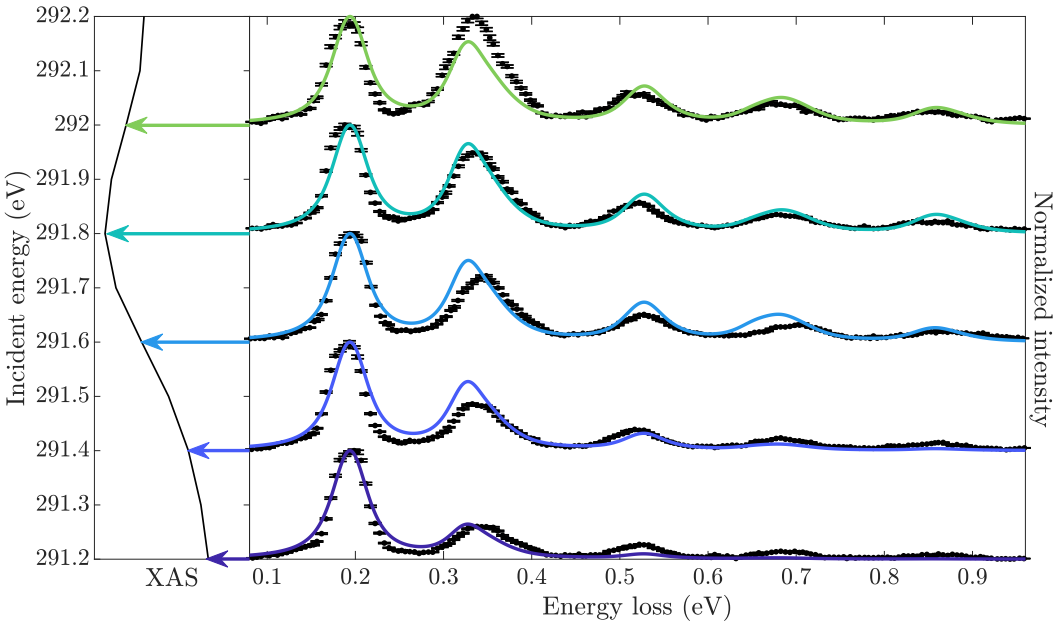

Figure 3.9: Incident-energy dependence of the experimental (black points with error bars), and calculated (blue to green lines) spectra around the σ^* resonance, plotted alongside the XAS with arrows indicating the incident energies.

that a finite value on the order of $G(\Gamma)$ is required to accurately capture the intensity and shape of the two-phonon peak.

Our best-fit $G(\boldsymbol{q})$ is also able to describe reasonably well the changing intensities of the features on detuning below 291.8 eV, as shown in Fig. 3.9. As for the π^* data, we expect agreement between the model and experiment to degrade above the resonance due to changes in the intermediate electronic state. The comparison is further complicated by the presence of an additional σ_2^* resonance above the σ_1^* peak that we have focussed on (see Fig. 3.3). This additional resonance arises from zero-point vibrations [127] that are not included in our modelling.

3.3.6 Comparison to previous resonant inelastic x-ray scattering study on graphite

Our results at the σ^* resonance highlight some important issues that have been previously overlooked in RIXS studies of EPC. Unlike at the π^* resonance where the stark splitting of the two-phonon feature clearly indicates a

deviation from the Ament model, at first glance our σ^* data could be seen to agree with the prediction for a dispersionless phonon. Indeed, the Ament model has previously been used to analyse spectra that show similarly subtle broadening and asymmetry of the multi-phonon features [101, 111], and shifts in their energies that have been potentially mistaken for anharmonic effects [111]. Even when its effects on the spectra are subtle, however, the dispersion of the phonons can have a large impact on the EPC strengths determined from RIXS measurements. In this section, I will compare our results to those of a previous RIXS study of graphite to highlight the importance of the phonon dispersion and mode mixing in the intermediate state.

Feng *et al.* previously presented K-edge RIXS measurements around the σ^* resonance of graphite with 70 meV energy resolution [118]. They did notice the broadening and unequal spacing of the multi-phonon peaks, which they correctly identified as being due to contributions from phonons of different momenta. They interpreted their data with reference to Raman spectroscopy results, however, implicitly assuming a coupling to electrons near the Fermi level. This led them to consider two modes, one at the Γ point and one at the K point, neglecting the other momenta at which we now know the EPC to be significant for σ^* electrons. To extract the EPC strengths they applied the Ament model independently for each mode, summing the two series of harmonics to fit their spectra. Rather than a single dispersive TO mode, this approach treats the phonons at Γ and K as separate dispersionless modes, and does not account for mixing between them in the intermediate RIXS state (i.e. no intermediate states containing both modes are allowed). In Sec. 3.3.3 we showed that this mode mixing affects the intensity of *all* the phonon features in a RIXS spectrum, including the one-phonon peak.

Figure 3.10(a) compares our best-fit $G(\boldsymbol{q})$ at the σ^* resonance to that obtained by Feng *et al.* From the resulting normalised spectra in Fig. 3.10(b), we see that the couplings determined by Feng *et al.* give a poor fit to all of the multi-phonon peaks. To isolate the effects of mode mixing, let us briefly

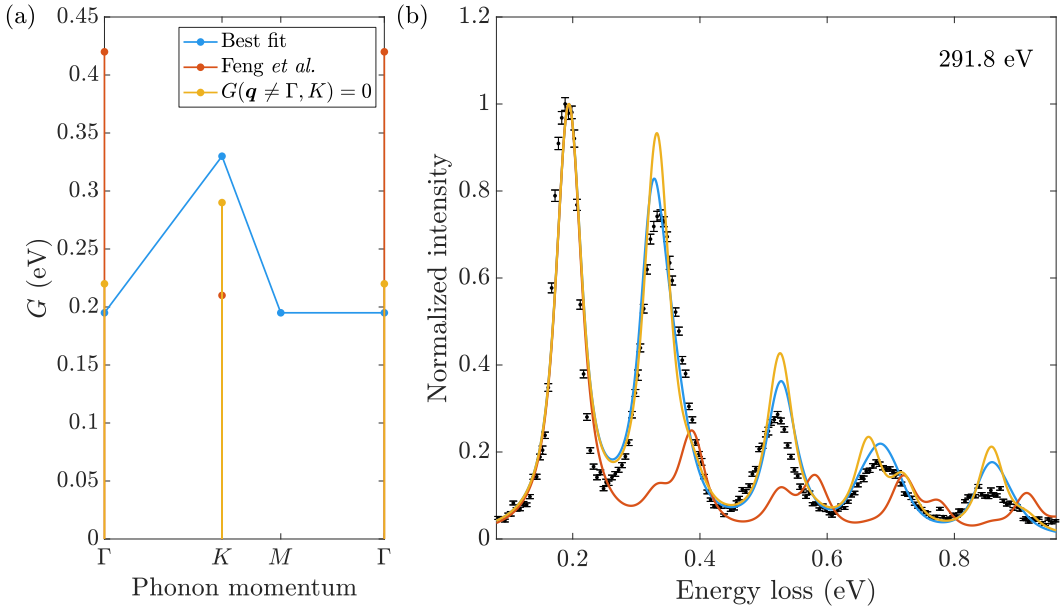

Figure 3.10: (a) Our best-fit $G(\boldsymbol{q})$ for σ^* electrons (blue), compared to that obtained by Feng *et al.* [118] (orange) and our best-fit with G constrained to be finite only at $\boldsymbol{q} = \Gamma$ and K (yellow). (b) Comparison of calculated RIXS spectra at the σ^* resonance, with colours corresponding to those in (a) and the experimental spectrum shown as black points with error bars. All spectra are calculated with $\gamma/2 = 0.15\,\text{eV}$.

set aside what we know about the momentum dependence of G away from the Fermi level and follow Feng *et al.* by fitting our σ^* spectrum with contributions from only Γ and K. While the calculated spectrum does not agree with the experimental data as well as our best fit, especially in the high-order peaks which become split [see Fig. 3.10(b)], we see that the values of M_Γ and M_K approach those of our linearly-varying model [see Fig. 3.10(a)]. Our constrained model yields a ratio $G(\Gamma)/G(K) = 0.79$, compared to $G(\Gamma)/G(K) = 2.1$ obtained by Feng *et al.* (note that $G(\Gamma)/G(K)$ is insensitive to the different intermediate-state lifetimes used, as in the Ament model the relative peak intensities depend on the ratio of G to lifetime). We therefore see that, even for the relatively flat TO mode studied here, accounting for intermediate-state mixing strongly affects the values of $G(\boldsymbol{q})$ extracted from experimental data.

3.4 Conclusion

In this chapter, I have shown that RIXS is a powerful probe of EPC for electrons both close to, and away from, the Fermi level. I presented high-resolution C K-edge measurements of graphite, which reveal that the momentum dependence of the EPC strength can be highly distinct in these two regimes: for low-energy π^* states $G(\boldsymbol{q})$ is concentrated in small regions around the Γ and K points, while for high-energy σ^* states it is significant across the Brillouin zone. This opens up a new range of out-of-equilibrium situations involving EPC, for example in optoelectronics, to which RIXS can be applied.

Our data show how the multi-phonon features in a RIXS spectrum can have contributions from modes away from the experimental momentum transfer, challenging the validity of the commonly used Ament model [100] that assumes dispersionless phonons. I presented an improved model developed by our collaborators based on Green's functions, which accounts for the full phonon and EPC dispersion, as well as mode mixing in the intermediate RIXS state, with minimal computational cost. This model successfully reproduced the multi-phonon features at both the π^* and σ^* resonances, allowing us to constrain $G(\boldsymbol{q})$ throughout the Brillouin zone from a single zone-centre spectrum. A comparison to previous RIXS measurements of graphite highlighted the importance of phonon dispersion and mode mixing in extracting accurate EPC strengths from experimental spectra. The availability of theoretical methods to treat these effects will become more pressing as RIXS is used to probe phonons in more complex and topical materials, such as Sr_2IrO_4 in Chapter 4.

Chapter 4

Electron-phonon coupling in a $5d$ spin-orbit Mott insulator

Sr_2IrO_4 was the first known example of a "spin-orbit Mott insulator", in which a SOC-induced band splitting enables a moderate Coulomb repulsion to localise the Ir 5d electrons. The entangled spin-orbital wavefunctions can be treated as $J_{eff} = 1/2$ pseudospins, with exchange interactions that are highly sensitive to the lattice geometry. In this chapter, I present a comprehensive survey of the low-energy excitations in Sr_2IrO_4 and the interactions between them. Firstly, the phonon band structure is determined by a combined non-resonant IXS and density functional theory study. These results are then used to inform the analysis of an O K-edge RIXS study of the phonons and magnon, both of which are found to be strongly coupled to the electronic degrees of freedom.

4.1 Introduction

Sr_2IrO_4 is the $5d$ equivalent of the $n = 1$ Ruddlesden-Popper ruthenate Sr_2RuO_4. While the greater spatial extent of the $5d$ orbitals would be expected to enhance itinerancy, this is counteracted by the increased SOC in the heavier Ir ion. SOC splits the crystal field t_{2g} levels into $J_{\text{eff}} = 1/2$ and $3/2$ states, the latter of which is filled by four of the five electrons, leaving a single $J_{\text{eff}} = 1/2$ hole. The width of the half-filled $J_{\text{eff}} = 1/2$ band is small enough that moderate electronic correlations can open a charge gap [128, 129], earning Sr_2IrO_4 the title of spin-orbit Mott insulator (see Sec. 1.1.1 for more detail).

In this chapter, I explore the consequences of SOC on the low-energy ex-

citations in Sr_2IrO_4. Using inelastic x-ray scattering alongside first-principles and model calculations, I determine the momentum dependence of the lattice and magnetic dynamics, and their respective couplings to electronic excitations. The first part of the chapter presents a non-resonant IXS study of the phonon band structure in parent and electron-doped Sr_2IrO_4. In both compounds, good agreement is found with non-magnetic density functional theory (DFT) calculations, with no anomalies due to magnetic or charge ordering visible. These measurements serve as a benchmark for an O K-edge RIXS study, which makes up the remainder of the chapter. The RIXS measurements resolve both phonon and magnon excitations with unprecedented detail, the former allowing a determination of the EPC for the t_{2g} and e_g electronic states, and the latter showing a deviation from the predictions of linear spin-wave theory due to coupling to a spin-orbit exciton mode.

4.1.1 Spin-lattice coupling

The crystal structure of Sr_2IrO_4, shown in Fig. 4.1(a), consists of monolayers of corner-sharing IrO_6 octahedra separated by sheets of Sr ions. The symmetry is reduced from the K_2NiF_4-type $I4/mmm$ (139) space group by a 12° staggered rotation of the octahedra around the c axis, leading to $I4_1/acd$ (142) [130]. Small differences in the tetragonal distortions of the octahedra that further reduce the symmetry to orthorhombic $I4_1/a$ (88) have recently been found [131, 132, 133], but these are insignificant for our analysis and the tetragonal $I4_1/acd$ space group (with $a = b \approx 5.5\,\text{Å}$ and $c \approx 25.8\,\text{Å}$) will be used throughout this chapter.

On cooling below $T_N \approx 240\,\text{K}$, Sr_2IrO_4 develops long-range antiferromagnetic order. As shown in Fig. 4.1(b), the $J_{\text{eff}} = 1/2$ pseudospins are arranged in an approximately antiferromagnetic pattern in each Ir–O plane (note that the tetragonal symmetry results in two equivalent domains with the spins mostly along $\boldsymbol{a}$ or $\boldsymbol{b}$ respectively) [129]. A slight canting of the pseudospins induces a net ferromagnetic moment in each plane, which are stacked in a $\downarrow\downarrow\uparrow\uparrow$ pattern along the c axis. Boseggia *et al.* found that the canting angle closely matches

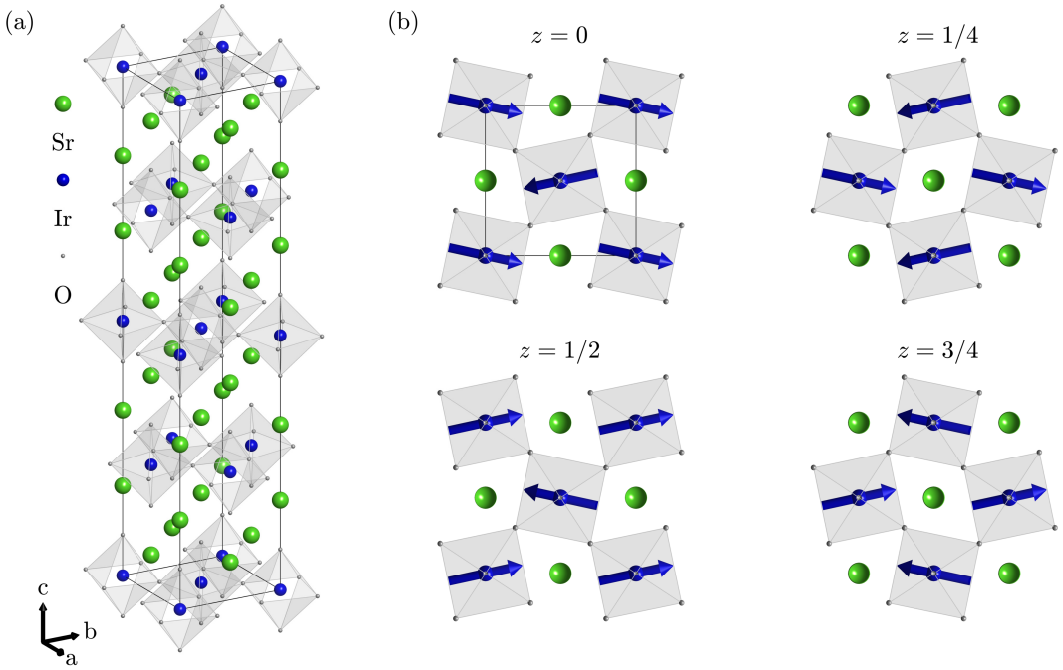

Figure 4.1: (a) Crystal structure of Sr_2IrO_4, showing monolayers of IrO_6 octahedra separated by Sr ions. (b) Canted antiferromagnetic structure of Sr_2IrO_4 in each of the four IrO planes of the unit cell. The canting induces a net ferromagnetic moment in each plane, which are stacked in a $\downarrow\downarrow\uparrow\uparrow$ pattern along the $\boldsymbol{c}$ direction.

that of the octahedral rotations [134], as had been predicted by Jackeli and Khaliullin on the basis of pseudospin-lattice coupling due to the strong SOC in Sr_2IrO_4 [12] (see the discussion in Sec. 1.1.2). They showed that the orbital component of the pseudospins results in exchange interactions that are highly sensitive to lattice geometry. For unrotated octahedra (180° Ir–O–Ir bond) the dominant term in the magnetic Hamiltonian is an isotropic Heisenberg exchange

$$H \supset \sum_{i,j} J_{ij} \boldsymbol{S}_i \cdot \boldsymbol{S}_j, \tag{4.1}$$

with J much larger for in-plane than out-of-plane nearest neighbours. The addition of octahedral rotations generates anisotropic terms

$$H \supset \sum_{i,j} J_z S_i^z S_j^z + \boldsymbol{D} \cdot \boldsymbol{S}_i \times \boldsymbol{S}_j, \tag{4.2}$$

where the XY anisotropy (first term) confines the pseudospins to the $\boldsymbol{a}$ –

b plane, and the DMI (second term) induces the canting. Finally, recent theoretical [135] and experimental [136] work has shown that a pseudo–Jahn-Teller effect generates in-plane anisotropies

$$H \supset \sum_{i,j} \Gamma_1 \cos(2\alpha)(S_i^x S_j^y + S_i^y S_j^x) - \Gamma_2 \sin(2\alpha)(S_i^x S_j^x - S_i^y S_j^y), \qquad (4.3)$$

with α the angle of the staggered moment direction (45° at equilibrium). These terms lead to an in-plane magnon gap, and small orthorhombic distortions below T_N. The dynamical consequences of pseudospin-lattice coupling have been seen in Raman measurements above T_N, where pseudospin fluctuations give rise to Fano anomalies in the phonon lineshapes [137].

4.1.2 Comparison to the cuprates

Much of the interest in Sr_2IrO_4 has been driven by its similarities with the $3d$ Mott insulator, and parent of the cuprate high-temperature superconductors, La_2CuO_4 [130, 138, 139, 134]. La_2CuO_4 hosts $S = 1/2$ moments in an antiferromagnetic arrangement with isotropic Heisenberg interactions [140], much like the $J_{\text{eff}} = 1/2$ pseudospins in Sr_2IrO_4 (notwithstanding the other anisotropic interactions discussed above). Destroying the long-range magnetic order in La_2CuO_4 through hole doping leads to superconductivity, raising the prospect of similar behaviour in Sr_2IrO_4. Indeed, electron doping the bulk of Sr_2IrO_4 leads to the suppression of long-range antiferromagnetic order [141], while surface doping has been shown to produce Fermi arcs [142] and a low-temperature gap with d-wave symmetry [143]. To date, however, superconductivity has not been found in Sr_2IrO_4.

Superconductivity is not the only ordered phase in the doped cuprates. Charge-density wave (CDW) order has long been proposed to be an intrinsic instability of doped Mott insulators [144, 145] and is pervasive across the cuprate families, where it is often accompanied by spin-density wave (SDW) order and appears to compete with superconductivity [65, 146]. Despite reports of SDW order [147] in doped Sr_2IrO_4, and a dynamic CDW-like instability in

its bilayer cousin $Sr_3Ir_2O_7$ [148, 149], as yet there has been no evidence for a CDW in doped Sr_2IrO_4.

4.2 Inelastic x-ray scattering study of the lattice dynamics

Spin-lattice coupling and the presence of CDW order can be inferred from momentum-resolved measurements of the lattice dynamics. The former manifests as changes in the phonon dispersion and linewidth on crossing T_N [137], while the latter causes a softening of phonon modes around the CDW wavevector [150, 151, 152]. Non-resonant IXS is an ideal probe for these effects, offering $\sim$1 meV energy resolution and $\sim$0.01 r.l.u. momentum resolution across a large volume of reciprocal space [153]. In this section, I report the results of IXS measurements on parent and electron-doped Sr_2IrO_4. In the parent compound, we find that our IXS spectra are well reproduced by a non-magnetic DFT calculation, with no broadening or frequency shifts apparent through T_N. We observe minimal changes to the phonons on doping, with the dispersions again well-reproduced by DFT, and no anomalies apparent at the equivalent cuprate CDW wavevector. Despite not providing evidence of new physics, these results serve as a reference for studies of the EPC later in the chapter.

The work presented in this section has been published as C. D. Dashwood *et al.*, Phys. Rev. B **100**, 085131 (2019) [154]. The parent and doped Sr_2IrO_4 single crystals were grown and characterised by Alberto de la Torre, Gang Cao and Robin Perry. The IXS measurements were performed by me, Hu Miao, James Vale and Mark Dean, with Daisuke Ishikawa and Alfred Baron as local contacts. The DFT calculations were performed by Danil Prishchenko and Vladimir Mazurenko. The data analysis and calculation of phonon properties from the DFT force-constant matrices was performed by me, and overseen by Mark Dean and Des McMorrow.

4.2.1 Experimental details

Single crystals of Sr_2IrO_4 and $Sr_{2-x}La_xIrO_4$ with $x \approx 0.1$ (i.e. 5% La-doped) were flux grown and characterised by energy-dispersive x-ray spectroscopy, resistivity and susceptibility measurements as described in a previous publication [155]. The crystalline quality of the samples was checked during the IXS measurements, with mosaics of around 0.02° for the parent compound and 0.05° for the doped.

IXS measurements were performed at beamline BL43LXU of the SPring-8 synchrotron in Japan [23]. The incident energy was set to 21.75 keV, and the $(11, 11, 11)$ reflection of Si was used as both a monochromator and analyser giving an energy resolution of 1.5 meV. A 4×6 analyser array allowed the simultaneous measurement of multiple momentum transfers, so that a large area of the Brillouin zone [shown in Fig. 4.2(a)] could be surveyed despite the long counting times necessitated by the high energy and momentum resolutions. A consequence of the analyser geometry is that the out-of-plane momentum transfer l varies across the array, as indicated by the colour of the points in Fig. 4.2(a). The layered nature of Sr_2IrO_4 means that its lattice dynamics depend only weakly on l, so we set the analyser slits to $40\times$ 80 mm to improve the in-plane momentum resolution while relaxing the out-of-plane resolution. The momentum resolutions are reported below for each set of measurements.

The parent compound was measured in transmission with the $[1, 1, 0]$ and $[0, 0, 1]$ reciprocal directions in the scattering plane, allowing access to purely in-plane momentum transfers in order to maximise the intensity of modes that involve modulation of the Ir–O–Ir superexchange bond. The vertical columns of the analyser array traced out adjacent trajectories along approximately $[-1, 1, 0]$ from the $(4, 5, 0)$ magnetic position [open circles in Fig. 4.2(a)]. As well as avoiding regions near the $(4, 4, 0)$ and $(4, 6, 0)$ Bragg peaks at which the IXS spectra would be dominated by strong elastic contributions, this is also the direction along which the dynamic CDW is expected in $Sr_3Ir_2O_7$ [149]. Other $\boldsymbol{q}$ points where one might expect the presence of phonon anomalies are

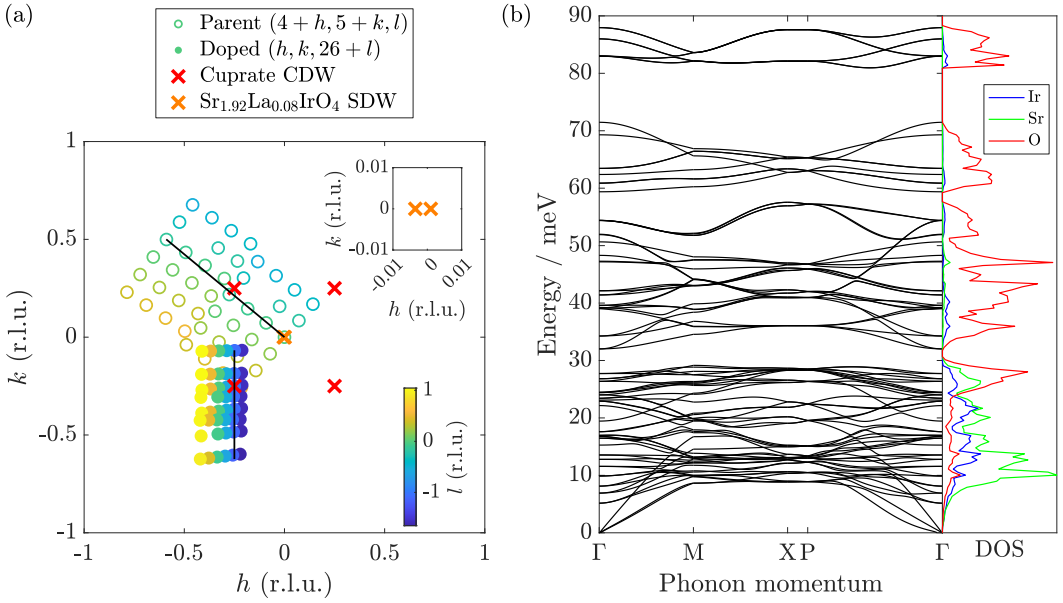

Figure 4.2: (a) Reciprocal-space map showing the measured $\boldsymbol{q}$ points for the parent [relative to $(4, 5, 0)$, empty circles] and doped [relative to $(0, 0, 26)$, filled circles] samples. The points have been projected onto the h–k plane, with l values indicated by colour. The red crosses show the equivalent in-plane wavevector of the cuprate CDW [152] and orange crosses those of the purported SDW in doped Sr_2IrO_4 [147] (shown magnified in the inset). The black lines indicate the momenta for which spectra are shown in Fig. 4.3 and 4.5. (b) Phonon band structure (black lines) and projected DOS for Ir (blue), Sr (green) and O (red) from DFT (LDA with a $2 \times 2 \times 1$ supercell). The high-symmetry points of the $I4_1/acd$ space group are $\Gamma = (0, 0, 0)$, $M = (0.5, 0, 0)$, $X = (0.5, 0.5, 0)$, and $P = (0.5, 0.5, 0.5)$.

at the intersections of the phonon and magnon dispersions. Unfortunately, the large gap and high velocity puts the spin-waves at energies above those of the phonon modes with significant IXS intensity [141]. The atomic displacements of modes with significant IXS intensity were calculated using DFT (see below) for a range of other $\boldsymbol{q}$ points, but none could be found with larger modulation of the Ir–O–Ir bond that we would expect to be more strongly influenced by magnetism.

The strongest coupling to CDW order is expected for high-energy in-plane optical phonon modes, and indeed much of the early work on the cuprates focussed on these modes [156, 157, 151, 158, 159]. These have vanishingly small IXS intensities, however, precluding detailed measurements of any softening.

In $La_{1.875}Ba_{0.125}CuO_4$, a large coupling to the CDW was also found for low-energy modes with large c-axis displacements [152], which are enhanced by having a large out-of-plane momentum transfer. For the doped Sr_2IrO_4 sample we therefore used a reflection geometry with the $[1, 0, 0]$ and $[0, 0, 1]$ directions in the scattering plane, so that we could measure $\boldsymbol{q}$ points in the $(0, 0, 26)$ Brillouin zone [filled circles in Fig. 4.2(a)]. A vertical column of the analyser array then followed the $[0, -1, 0]$ direction through the equivalent cuprate CDW wavevector [red crosses in Fig. 4.2(a)].

DFT calculations were performed using the plane-wave basis projector augmented wave method [160] as implemented in the Vienna *ab-initio* Simulation Package [161]. The exchange-correlation functional was treated in the Local Density Approximation (LDA) [162], with unit cell relaxations carried out over an $8 \times 8 \times 2$ reciprocal lattice mesh. The force constants were calculated over a $4 \times 4 \times 2$ mesh using a $2 \times 2 \times 1$ supercell. The phonon frequencies and eigenvectors were then obtained using the PHONOPY package [163] with an $11 \times 11 \times 11$ mesh for the Debye-Waller factor, and these were used to calculate the dynamic structure factor $S(\boldsymbol{q}, \omega)$. The resulting phonon band structure and projected density of states (DOS) is shown in Fig. 4.2(b). As expected, the modes involving motion of mostly the heavier Ir and Sr ions lie at lower energies, while the motion of lighter O ions dominates above 30 meV.

The LDA calculation does not take into account the effects SOC, electron correlations quantified by U, or the magnetic structure, and therefore does not predict an electronic structure in agreement with the known spin-orbit Mott-insulating state of parent Sr_2IrO_4 (the metallic ground state that it predicts is in fact a better description of the doped compound). We repeated the DFT calculation including SOC+U, with $U = 3.05$ eV and $J = 0.48$ eV to reproduce the measured charge gap [164], and the non-collinear antiferromagnetic structure given by Ye *et al.* [131]. Due to the additional memory requirements of this calculation, however, the force-constant supercell had to be reduced to $1 \times 1 \times 1$. A comparison between the LDA and LDA+SOC+U calculations

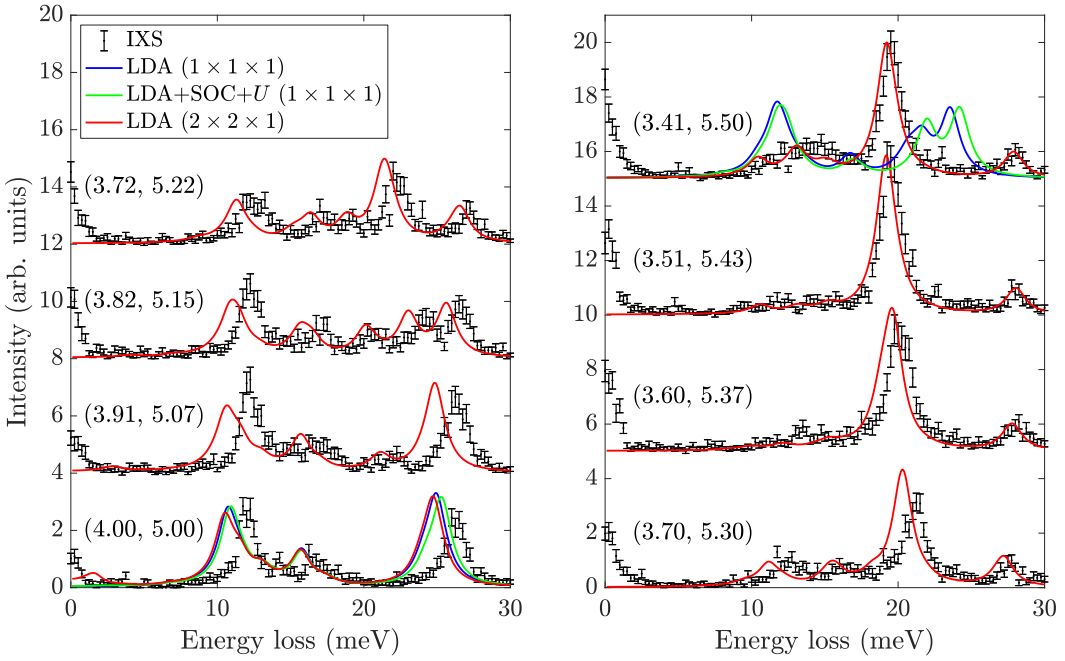

Figure 4.3: Representative IXS spectra at momenta along approximately $[-1, 1, 0]$ from the magnetic position $(4, 5, 0)$ in the parent compound at 100 K (black points), vertically shifted for clarity. These are compared to DFT calculations using the LDA with a $1 \times 1 \times 1$ supercell (blue lines), LDA+SOC+U with a $1 \times 1 \times 1$ supercell (green lines), and LDA with a $2 \times 2 \times 1$ supercell (red lines).

will be given in the next section.

4.2.2 Search for pseudospin-lattice coupling in the parent compound

Figure 4.3 shows a series of representative IXS spectra along approximately $[-1, 1, 0]$ from the magnetic position $(4, 5, 0)$ [black line in Fig. 4.2(a)] in the parent compound at 100 K. The average momentum resolutions along each direction are $\boldsymbol{\Delta q} = (0.06, 0.07, 0.13)$ r.l.u. (as $\Delta l \sim |l|$ we ignore the out-of-plane momentum from here on). The IXS spectra are overlaid with $S(\boldsymbol{q}, \omega)$ calculated with the LDA on a $2 \times 2 \times 1$ supercell. At all momenta, the calculation reproduces the relative intensities of the modes reasonably well, with a consistent underestimate of the frequencies improving away from $(4, 5)$. The calculation allows us to identify the atomic motion associated with each peak of the IXS spectra. As expected from the in-plane momentum transfer, the

modes mostly involve atomic motions in the $\boldsymbol{a} - \boldsymbol{b}$ plane. At $(4, 5)$, the intense mode with an LDA energy of 10.5 meV has large displacements of Sr with smaller Ir and O motion, while the mode at 24.7 meV has dominant in-plane O motion along with smaller out-of-plane Sr oscillations. At $(3.41, 5.50)$, the mode at 19.2 meV has roughly equal in-plane displacements of all atoms. While there is unlikely to be any detectable influence from magnetism on the low-energy mode with dominant Sr motion, the higher energy mode involves significant changes to the angle of the Ir–O–Ir superexchange bond. There are no apparent discrepancies between the experiment and calculation for the high energy mode that are not also present for the low energy mode, however.

Also shown at $(4, 5)$ and $(3.41, 5.50)$ is $S(\boldsymbol{q}, \omega)$ calculated with the LDA and LDA+SOC+U on a $1 \times 1 \times 1$ supercell. At the commensurate position, the atomic displacements can be well described within a single unit cell such that the calculations are minimally dependent on supercell size. As can be seen in Fig. 4.3, the calculated spectra at $(4, 5)$ differ by only a $\sim$0.5 meV shift in the mode energies (well below our energy resolution) and very small changes in intensities. Again at $(3.41, 5.50)$ there is little difference between the LDA and LDA+SOC+U calculations on the minimal supercell, but these differ strongly from the experimental data and LDA calculation on the $2 \times 2 \times 1$ supercell. This comparison validates our prioritisation of supercell size over the addition of SOC+U in our calculations.

To search for any changes caused by long-range magnetic ordering, we repeated the above measurements at 260 K $> T_N$. To reliably compare spectra at different temperatures, we must remove the effect of the Bose factor by calculating the imaginary part of the dynamic susceptibility [152]

$$\chi''(\boldsymbol{q}, \omega) = S(\boldsymbol{q}, \omega) \left(1 - e^{-\omega/(k_B T)}\right) \tag{4.4}$$

after subtraction of the elastic line. Figure 4.4 shows χ'' calculated from the IXS data and DFT calculations at 100 K and 260 K for two representative momentum transfers. The overall intensity is lower at 260 K compared to 100 K

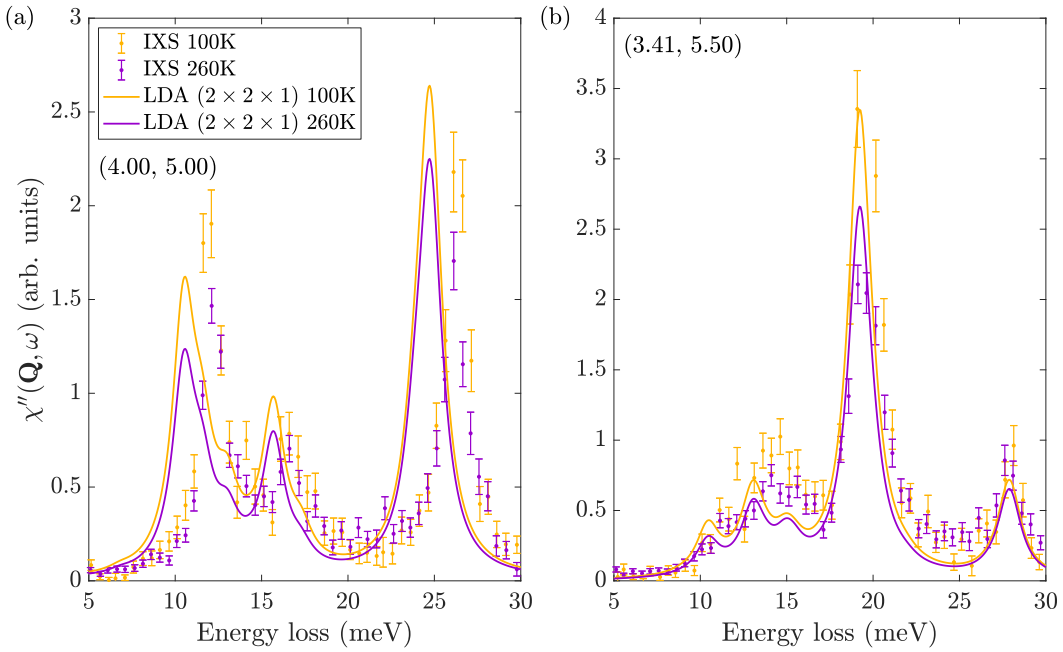

Figure 4.4: Bose-factor corrected IXS spectra in the parent compound (points) and $\chi''(\boldsymbol{q},\omega)$ calculated using the LDA on a $2\times2\times1$ supercell (lines) at 100 K (orange) and 260 K (purple) for momentum transfers of (a) $(4,5)$ and (b) $(3.41,5.50)$.

due to the reduced Debye-Waller factor, and the ∼0.5 meV hardening of the modes in the experimental spectra can be attributed to reduced anharmonic phonon-phonon interactions on cooling. There is no evidence for changes in the energies or linewidths of the modes through T_N that would be indicative of a coupling to spin fluctuations, in either these spectra or those at the other momentum transfers shown in Fig. 4.2(a). This is in contrast to previous Raman spectroscopy results, which found an asymmetric broadening of a magnitude similar to our energy resolution for the A_{1g} mode [137], although this particular mode has vanishing IXS intensity at the $\boldsymbol{q}$ points measured here. It remains an open question why the modes that we measure do not show such a strong coupling to magnetic order, despite the large modulation of the superexchange bond that they involve.

4.2.3 Search for charge order in the doped compound

CDW order in the cuprates strongly influences the lattice dynamics, resulting in anomalies in the IXS spectra around the CDW wavevector. IXS mea-

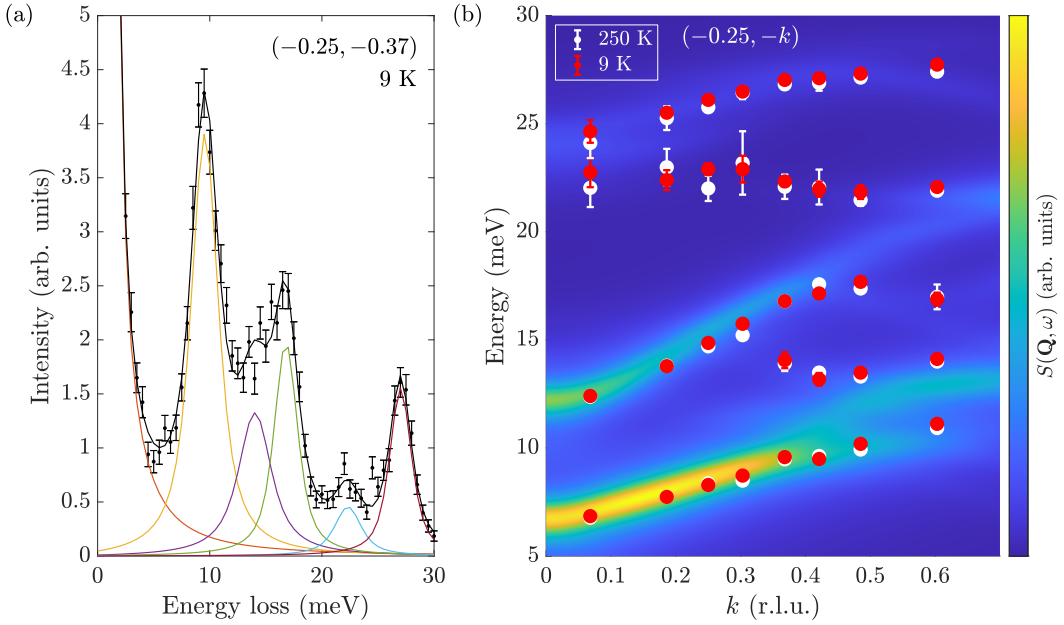

Figure 4.5: (a) Representative IXS spectrum at momentum transfer $(-0.25, -0.37)$ and temperature 9 K (black points) fitted with a sum (black line) of damped harmonic oscillator lineshapes (coloured lines). (b) Extracted phonon dispersions at 250 K (white points) and 9 K (red points), overlaid on a colourmap of $S(\boldsymbol{q}, \omega)$ calculated using the LDA on a $2 \times 2 \times 1$ supercell for the patent compound.

surements on $La_{2-x}Ba_xCuO_4$ with $x \approx 0.1$ revealed that precursor CDW fluctuations are responsible for a broadening and softening of the phonons [165, 156, 157, 151, 158, 159, 166, 152]. On the onset of long-range CDW order the softening is still present, while there is a sharp reduction in the phonon linewidths. To investigate whether CDW order is present in electron-doped Sr_2IrO_4 in analogy with the hole-doped cuprates, we performed IXS measurements on $Sr_{2-x}La_xIrO_4$ with $x \approx 0.1$. We measured along the $[0, -1, 0]$ direction though the equivalent cuprate CDW wavevector $(0.25, 0.25, 26)$, with an average momentum resolution of $(0.04, 0.04, 0.36)$ r.l.u. (again, as $\Delta l \sim |l|$ we ignore the out-of-plane momentum from here on).

In order to extract the phonon dispersions, the IXS spectra were fitted to a sum of damped harmonic oscillator lineshapes χ''_j weighted by the Bose

factor and convoluted with a Voigt resolution function R

$$S(\boldsymbol{q},\omega) = \sum_j \frac{\chi''_j(\boldsymbol{q},\omega)}{1 - e^{-\omega/(k_B T)}} * R(\omega) \tag{4.5}$$

plus an additional Voigt function for the quasi-elastic peak. An example of a fitted spectrum is shown in Fig. 4.5(a), with the number of modes guided by the DFT calculation. The resulting dispersions at 250 K and 9 K are plotted in Fig. 4.5(b) over a colourmap of $S(\boldsymbol{q},\omega)$ from the same LDA calculation on a $2 \times 2 \times 2$ supercell as for the parent compound. This non-magnetic DFT calculation actually provides a better description of the metallic ground state of the doped sample, in which long-range magnetic order is destroyed by the free carriers [141], and so as expected there is good agreement between the fitted and calculated dispersions. The calculations allow us to identify the atomic motions associated with each mode, which at these wavevectors involve significant out-of-plane displacements for all three elements. Crucially, the fitted dispersions are identical (within one standard deviation) at both temperatures, with no anomalies present at the cuprate CDW wavevector. Similarly, no anomalies are visible at any other $\boldsymbol{q}$ point measured for this sample [see Fig. 4.2(a)].

A further signature of static CDW order in the cuprates appears in the intensity of the quasi-elastic peak at zero energy loss in the IXS spectra. In the underdoped cuprate $YBa_2Cu_3O_{6.6}$, for instance, Le Tacon *et al.* saw a sudden increase in the intensity of this peak in a narrow momentum range around the CDW wavevector, and over a broad temperature range around the CDW transition temperature [167]. At both 9 K and 250 K, however, the fitted integrated intensity of the quasi-elastic peak in our IXS spectra varies smoothly with $\boldsymbol{q}$.

While we have failed to find any evidence of phonon anomalies, it should be emphasised that our results do not preclude the presence of a coupling between phonons and CDW/SDW order at other doping levels (the purported

SDW in $Sr_{2-x}La_xIrO_4$ is only seen in samples with x close to 0.4 [147]), or at wavevectors away from those measured here.

4.3 Resonant inelastic x-ray scattering study of the low-energy excitations

Our IXS measurements, detailed above, provided no evidence of coupling between lattice excitations and magnetic or charge order in Sr_2IrO_4. IXS cannot access electronic or magnetic excitations, however, for which the fingerprints of electron-lattice coupling may be more apparent. We saw in Chapter 3 that RIXS is a powerful probe of EPC, and in this section we wield this power to explore the coupling of phonons to t_{2g} and e_g electrons in Sr_2IrO_4. We choose to use x-rays tuned to the O K edge, as the long core-hole lifetime at this edge results in strong phonon excitations. The other benefit is that O K-edge RIXS can access magnetic excitations due to hybridisation between the O $2p$ and Ir $5d$ orbitals [168], allowing us to simultaneously investigate the magnetic excitations. At both the t_{2g} and e_g resonances we fit the phonon features in our spectra with a two-mode extension of the Ament model [115], finding strong EPC of a similar magnitude to that in the cuprates [101, 102, 103, 104, 105, 106, 107]. Our high-resolution measurements also allow us to refine the magnon dispersion, revealing interactions with a spin-orbit exciton mode that cannot be described by conventional linear spin-wave theory.

The Sr_2IrO_4 single crystal used in these measurements was grown and characterised by Alberto de la Torre, Gang Cao and Robin Perry. The RIXS measurements were performed by me, James Vale, Eugenio Paris, Larissa Veiga, Thorsten Schmitt and Des McMorrow, with Abhishek Nag and Kejin Zhou as local contacts. The data analysis was performed by me, and overseen by Thorsten Schmitt and Des McMorrow.

4.3.1 Experimental details

Our RIXS measurements were performed at beamline I21 of the Diamond Light Source. Sr_2IrO_4 single crystals were mounted on copper sample holders with silver epoxy and cleaved in-vacuum, with samples from different batches used for the t_{2g} (Sec. 4.3.3 and 4.3.5) and e_g (Sec. 4.3.4) measurements. The energy resolution at the O K edge was determined to be 0.028 eV by scattering from amorphous carbon tape. All RIXS spectra were taken with linear horizontal incident x-ray polarisation, at a temperature of 15 K (21 K) and with counting times of 40 min (60 min) for the t_{2g} (e_g) data. The in-plane momentum transfer was varied by changing the sample angle θ while keeping the scattering angle fixed at $2\Theta = 154°$. At these energies the in-plane momentum transfer is kinematically limited to $\sqrt{h^2 + k^2} \lessapprox 0.4$ r.l.u. for the chosen scattering geometry. As with the IXS measurements, the varying out-of-plane momentum can be neglected due to the quasi-2D nature of Sr_2IrO_4. X-ray absorption spectra in total electron yield were obtained by measuring the sample drain current. All data have been corrected for incident flux and self-absorption using standard methods [169, 111, 119].

4.3.2 Resonant inelastic x-ray scattering measurements

The XAS around the O K-edge for incident x-rays polarised in (π) and normal to (σ) the scattering plane are shown in Fig. 4.6(a). Below the main edge at 534 eV, a number of polarisation-dependent pre-edge features can be seen, arising from hybridisation between different combinations of the O $2p$ and Ir $5d$ orbitals. The features between 529 and 531 eV involve the Ir t_{2g} orbitals, xy and yz/zx (split by tetragonal distortions of the IrO_6 octahedra [133]), which couple to the apical (A) and in-plane (P) O orbitals. The higher-energy features between 531 and 533 eV involve hybridisation between the O $2p$ and Ir e_g states [111]. In order to maximise the intensity of the inelastic features we fix the incident polarisation to horizontal (π) for the RIXS measurements.

Figure 4.6(b) shows a RIXS map with incident energies around the two

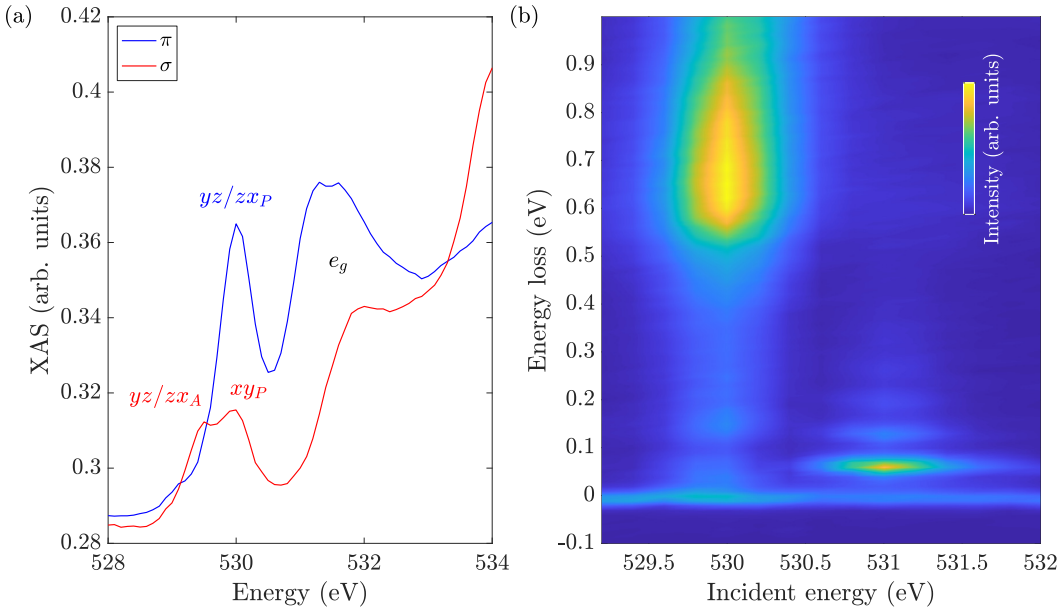

Figure 4.6: (a) XAS around the O K edge, taken with grazing-incidence x-rays of linear horizontal (π, blue line) and vertical (σ, red line) polarisation. The pre-edge features arising from hybridisation between O $2p$ (apical, A, and in-plane, P) and Ir t_{2g} (xy, yz and zx) or e_g orbitals are labelled. (b) RIXS map around the O K edge, taken with π incident polarisation at an in-plane momentum transfer of $(0.25, 0.25)$ and temperature of 21 K.

pre-edge features. At the t_{2g} resonance (530 eV) a strong electronic excitation can be seen above 0.5 eV energy loss, arising from transitions between the $J_{\text{eff}} = 3/2$ and 1/2 states [168, 170]. Below this are a number of magnetic and lattice excitations. At the e_g resonance (531 eV) the electronic and magnetic excitations are suppressed, as expected, and a phonon mode with fundamental frequency of ∼0.06 eV is enhanced. I will first treat the EPC at the t_{2g} and e_g resonances in turn, before analysing the magnon and its relation to the higher-energy electronic excitations.

4.3.3 Electron-phonon coupling at the t_{2g} resonance

The momentum dependence of the spectra at the t_{2g} resonance along two different directions in the Brillouin zone is shown in Fig. 4.7. Our high-resolution data reveal a number of distinct features in the region below 0.4 eV, which we identify through comparison with previous O K-edge and Ir L_3-edge RIXS studies. The peak that disperses out from the elastic line to 0.16 eV at

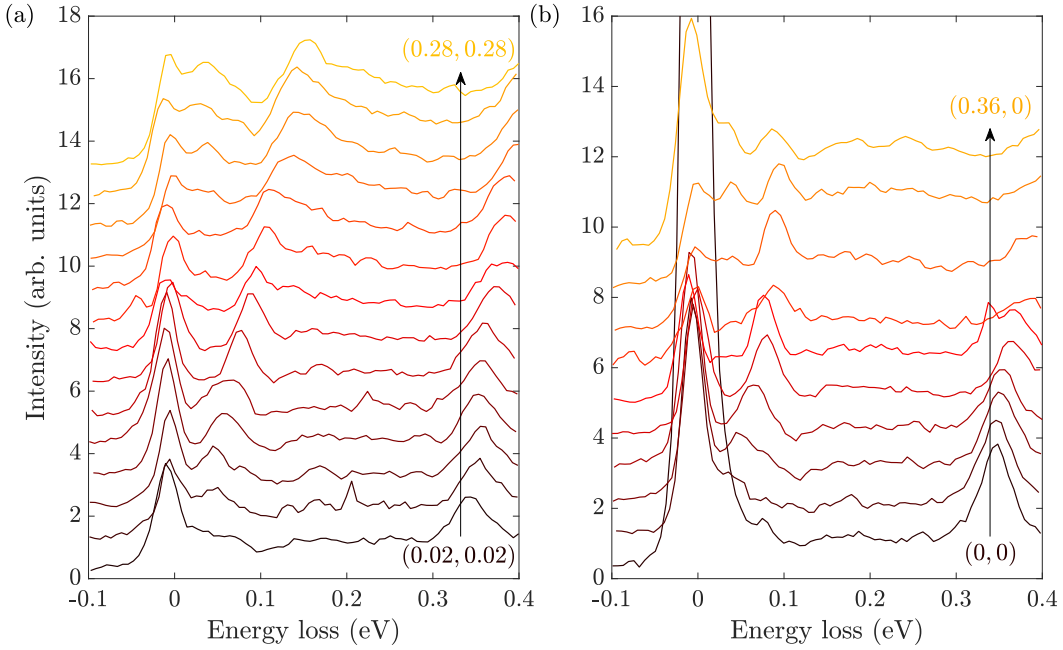

Figure 4.7: RIXS spectra at the t_{2g} resonance (530 eV) along (a) (h, h) and (b) $(h, 0)$, vertically offset for clarity. The magnon can be seen dispersing out from the elastic line, with low-energy phonon harmonics visible below it at the highest momenta. The dispersive feature above 0.3 eV is an exciton [168].

$(0.28, 0.28)$, and to 0.09 eV at $(0.36, 0)$, broadly matches the known dispersion of the magnon [139, 141, 168] (see Sec. 4.3.5). Above the magnon is a broad continuum of excitations, which can be attributed to multi-magnon excitations that are known to be enhanced at the O K edge [168]. A second dispersive mode can be seen above 0.3 eV, which has previously been identified as an exciton formed by bound electron-hole pairs across the charge gap [168, 170]. The final features, which only become apparent away from the zone centre, lie below the magnon in the energy range occupied by phonons [154].

From Chapter 3, we know that phonon excitations in RIXS appear as a series of harmonic peaks of decreasing intensity, and at the highest momenta along (h, h) there indeed appears to be multiple peaks between the elastic line and magnon. As an initial attempt, I fit these peaks with the simple model by Ament *et al.* that consists of a single non-dispersing mode coupled linearly to an isolated electronic level [100] (see Sec. 3.2.1). The fit to the spectrum at $(0.28, 0.28)$ its shown in Fig. 4.8(a), using an inverse core-hole lifetime of

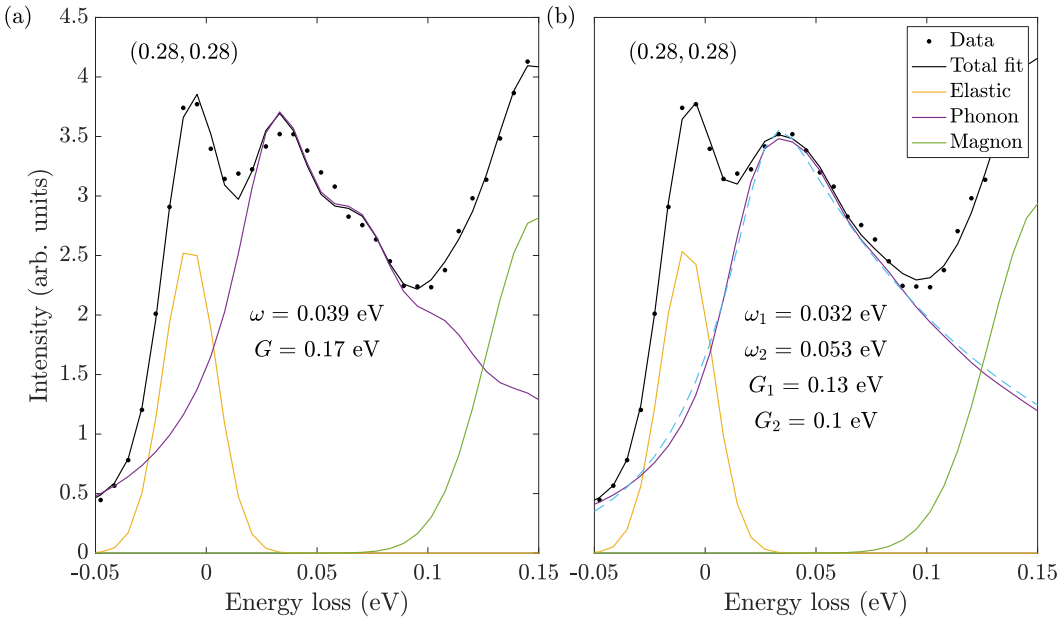

Figure 4.8: Representative fits (black lines) of the low-energy region of the RIXS spectrum at $(0.28, 0.28)$ (points) with (a) the single-mode Ament model [100] and (b) a two-mode model [115]. As well as the phonon contribution (purple lines), the fits consist of a resolution-limited Gaussian elastic peak (yellow lines) and Gaussian magnon peak (green lines). The dashed blue line in (b) is a resolution-convolved back-to-back exponential function used to approximate the phonon contribution when fitting the magnon dispersion (see Sec. 4.3.5).

0.12 eV [115] and yielding a fundamental phonon energy of 0.039 eV and an EPC strength of 0.17 eV. While these magnitudes are reasonable, the fit is not unique and the fitted parameters vary erratically between the different momentum transfers. Closely inspecting the fit, it can be seen that there is some missing intensity between the elastic line and first harmonic, as well as between the first and second harmonics. This suggests the presence of a second, overlapping series of phonon peaks.

To test this hypothesis, I attempted a second fit using an extension of the Ament model by Geondzhian and Gilmore that includes a second mode and allows for mixed excitations of both modes [115]. The resulting fit is shown in Fig. 4.8(b). The two-mode model fills in the missing intensity and provides good agreement with the experimental data. As the individual phonon peaks are not resolved, however, the possibility that the improved fit is simply a con-

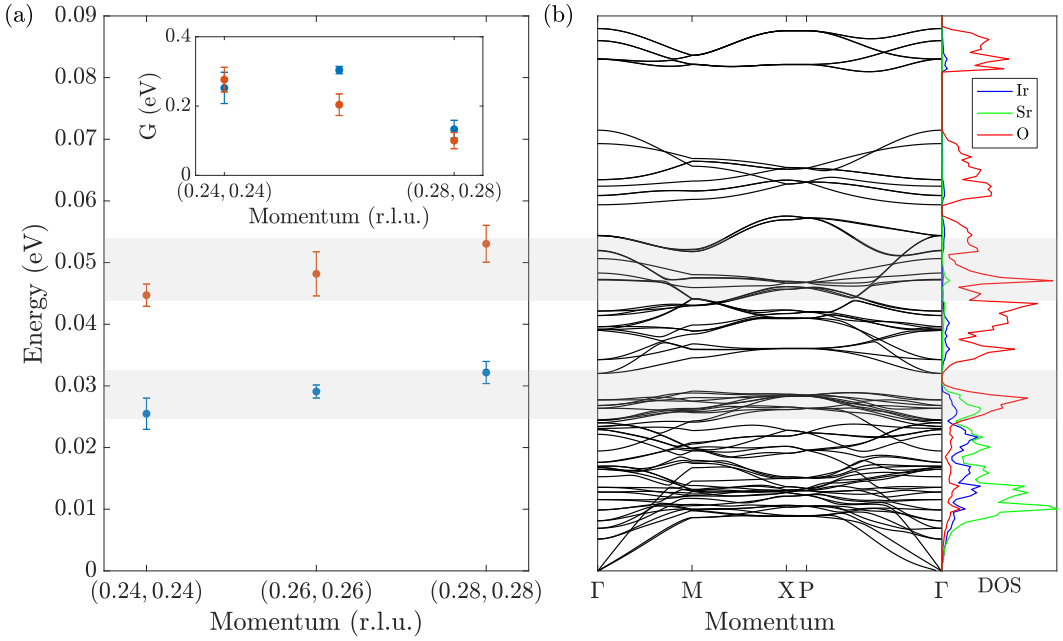

Figure 4.9: (a) Phonon energies from two-mode fits such as that in Fig. 4.8(b). The inset shows the fitted EPC strengths G. (b) Phonon band structure (black lines) and projected phonon density of states (DOS) for Ir (blue), Sr (green) and O (red) from DFT (LDA with a $2 \times 2 \times 1$ supercell, see Sec. 4.2.1).

sequence of over-parameterisation should be investigated. Figure 4.9(a) shows the fitted energies of the two modes at the few momenta where harmonics are visible. Unlike for the one-mode fit, the values do not vary dramatically as a function of momentum. We can also compare the fitted energies to the IXS-validated DFT band structure from Sec. 4.2.1, shown in Fig. 4.9. We see reasonable agreement with modes involving mostly O displacements as expected for measurements at the O K edge. While this gives further reassurance of the reliability of the two-mode fit, we cannot rule out the presence of additional unresolved modes in the spectra. The kinematic limitations on accessible momenta, and the presence of the magnon which obscures the higher harmonics, are unavoidable at the O K edge, but future measurements with higher energy resolution and polarisation analysis of the scattered beam would help to constrain the fitting.

The EPC strengths, shown in the inset of Fig. 4.9(a), are found to be $\sim$0.2 eV for both modes in this region of reciprocal space. As the intensity of

the phonon features in RIXS is a monotonic function of the EPC [100, 115], we expect the EPC of both modes to fall towards the zone centre where the peaks are suppressed. The values of G found here are of a similar magnitude to those previously determined by RIXS on various cuprates [101, 102, 103, 104, 105, 106, 107] and other iridates [112, 111]. While the role of EPC in the high-temperature superconductivity of the cuprates is still under debate, this observation adds a further similarity between the two material families. Our analysis improves on previous studies where multiple phonon modes are visible [104, 111, 105, 118] by accounting for mixing between the modes [115]. In common with these other studies, however, we do not account for the dispersion of the phonon energies or EPC strengths, which we learnt in Chapter 3 can have a sizeable impact on the extracted values of G [119]. In this case, the complex electronic and phononic structures of Sr_2IrO_4 make the Green's-function model of Chapter 3 too computationally expensive for practical use. This limits our results to order-of-magnitude estimates for G.

4.3.4 Electron-phonon coupling at the e_g resonance

We saw in Sec. 4.3.2 that there are no magnetic excitations at the e_g resonance, so we do not have to worry about them obscuring the phonon peaks. This allows a determination of the EPC over an extended region of the Brillouin zone. The momentum dependence of the RIXS spectra at the e_g resonance is shown in Fig. 4.10. The most apparent feature is a series of phonon harmonics of fundamental energy $\sim$0.7 eV, with minimal dispersion but whose intensity increases away from the zone centre. As the same O states are involved at the e_g and t_{2g} resonances, the difference in excited phonon modes reflects the difference in EPC for the Ir orbitals. At the highest momenta in Fig. 4.10 we can see multiple harmonics, which should allow a robust fitting.

As with the t_{2g} spectra, I initially attempted a fit with the single-mode Ament model. Figure 4.11(a) shows a representative fit at $(0.4, 0)$, which satisfactorily captures the prominent harmonics with a fundamental phonon energy of 0.068 eV. Again, however, there appears to be some missing intensity

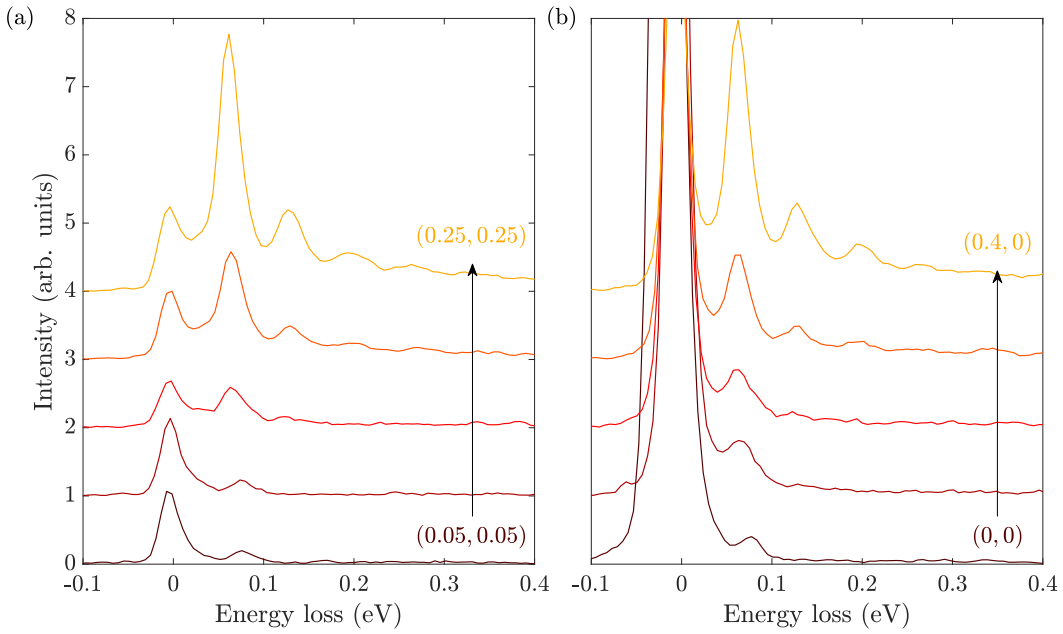

Figure 4.10: RIXS spectra at the e_g resonance (531 eV) along (a) (h, h) and (b) $(h, 0)$, vertically offset for clarity. Compared to the t_{2g} resonance, the electronic and magnetic excitations are suppressed and a different phonon mode is enhanced.

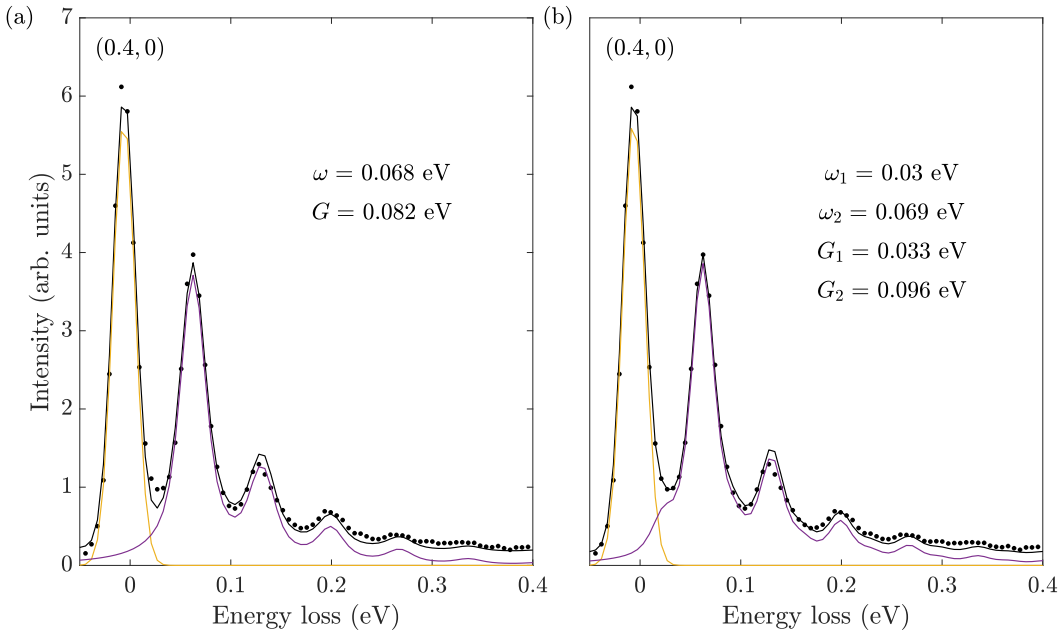

Figure 4.11: Representative fits (black lines) of the RIXS spectrum at $(0.4, 0)$ (points) with (a) the single-mode Ament model [100] and (b) a two-mode model [115]. As well as the phonon contribution (purple lines), the fits consist of a resolution-limited Gaussian elastic peak (yellow lines).

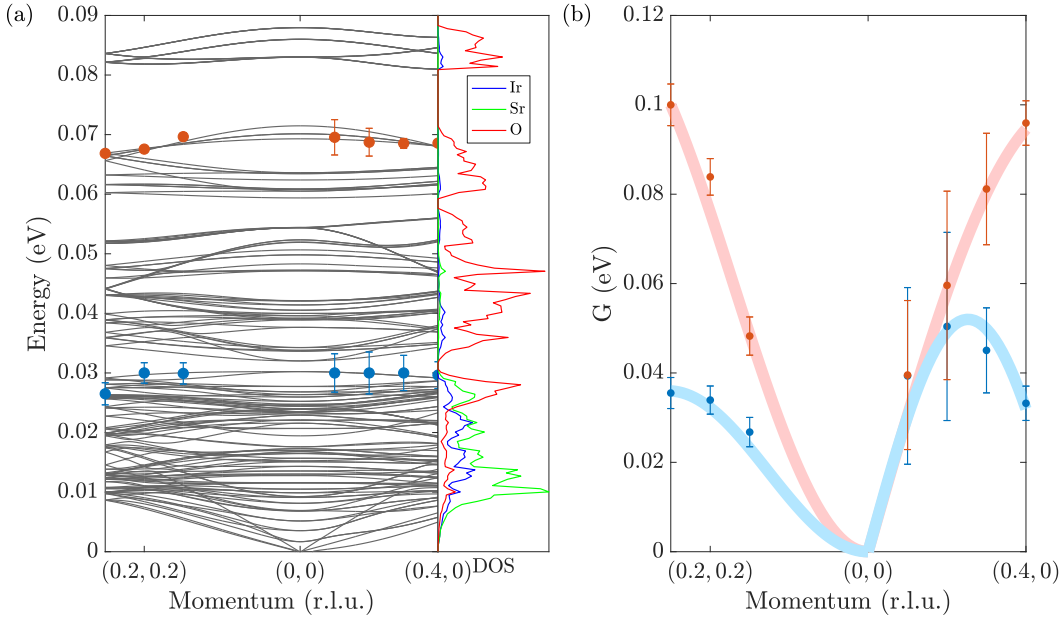

Figure 4.12: (a) Fitted phonon energies (orange and blue points) overlaid on the phonon band structure from DFT (LDA with a $2 \times 2 \times 1$ supercell, grey lines). The energies match well with specific phonon modes, which the DOS on the right shows to have dominant O motion. (b) EPC strengths from two-mode fits such as that in Fig. 4.11(b). Solid lines are guides to the eye. The phonon intensity near the zone centre is too low to allow accurate fitting.

between the elastic line and first harmonic, which suggests that the two-mode model may be required. In Fig. 4.11(b) it can be seen that a two-mode fit nicely fills in this intensity, as well as a small peak between the third and fourth harmonics at 0.23 eV energy loss that arises from a mixed excitation of the two modes. The only feature of the data that is not well captured by the fit is a slight broadening of the high harmonics, which we know to be due to the dispersion of the phonon [119].

The fitted phonon energies are shown in Fig. 4.12(a), overlaid on the DFT band structure. Although it should be remembered that the DFT energies are slightly shifted compared to our IXS data (see Fig. 4.3), the fitted dispersions match well to DFT modes. The higher-energy mode matches one involving elongations of the IrO_6 octahedra along the c axis, while the lower-energy mode, which appears to be the same as that excited at the t_{2g} resonance, matches one consisting of tilts of the IrO_6 octahedra. The extracted EPC

strengths are shown in Fig. 4.12(b). As with the t_{2g} data, the fact that the phonon intensity near the zone centre is too low to allow reliable fitting tells us that the EPC strengths are small in this region. The EPC of the higher-energy mode increases along both $(h, 0)$ and (h, h), roughly following a sinusoidal dependence and reaching $\sim$0.1 eV at the maximum momenta. The EPC of the lower-energy mode follows a similar dependence along (h, h), reaching $\sim$0.04 eV at $(0.25, 0.25)$. Along $(h, 0)$, however, it initially rises before appearing to dip towards $(0.5, 0)$. These mirror the trends calculated for O modes in the cuprates [171], where the different momentum-dependences arise from the differing symmetry of the phonon modes. Our results therefore add another point of similarity between Sr_2IrO_4 and the cuprates.

4.3.5 Magnetic excitations

Turning back to the t_{2g} data, we now analyse the magnetic excitations in greater detail. We first have to remove the contributions from the phonons, whose higher harmonics overlap with the dispersing magnon (see Sec. 4.3.3). To account for the spectral weight without computationally-demanding calculation of the full cross section, I approximate the sum of all the phonon harmonics with a back-to-back exponential function convoluted with a Gaussian resolution function [172]

$$\frac{\alpha\beta}{2(\alpha+\beta)}\left[\exp\left(\frac{\alpha[\alpha\Delta\omega^2+2(\omega-\omega_0)]}{2}\right)\operatorname{erfc}\left(\frac{\alpha\Delta\omega^2+[\omega-\omega_0]}{\Delta\omega\sqrt{2}}\right)+\right.$$
$$\left.\exp\left(\frac{\beta[\beta\Delta\omega^2-2(\omega-\omega_0)]}{2}\right)\operatorname{erfc}\left(\frac{\beta\Delta\omega^2-[\omega-\omega_0]}{\Delta\omega\sqrt{2}}\right)\right], \quad (4.6)$$

where α (β) is the exponential rise (decay) scale, $\Delta\omega$ is the energy resolution, and ω_0 is the energy loss of the peak. A comparison of this lineshape to that of the two-mode model at $(0.28, 0.28)$ is shown in Fig. 4.8(b), where good agreement can be seen in the region of interest. To constrain the fitting at other momentum transfers where the phonons are less prominent, the values of α and β were fixed to the values determined at $(0.28, 0.28)$ while the overall intensity and ω_0 were allowed to vary.

Thankfully the phonons are suppressed near the zone centre where the single-magnon peak is at lower energies, allowing a robust fitting at all momentum transfers. For the magnon, I use a damped harmonic oscillator lineshape including the Bose factor [173]

$$\frac{\omega}{1-e^{-\omega/(k_BT)}}\frac{4\omega_0\gamma}{\left(\omega^2-\omega_0^2\right)^2+(2\omega\gamma)^2}, \tag{4.7}$$

where γ is the damping factor, and the magnon frequency is given by $\sqrt{\omega_0^2-\gamma^2}$ (the imaginary part of the pole of the dynamic susceptibility). This lineshape can describe both propagating and over-damped modes depending on the ratio of γ to ω_0, although in undoped Sr_2IrO_4 the damping should be minimal [141]. Note that this lineshape is motivated by the assumption that the RIXS cross section is proportional to the dynamic structure factor $S(\boldsymbol{q},\omega)$ [174].

Above the single magnon are multi-magnon excitations that are known to be enhanced at the O K edge [168], and which are likely to be dominated by bi-magnons. Many studies fit the bi-magnons with a broad peak centred at twice the single-magnon energy [139, 141, 168, 170], but this is not well physically motivated. In $\boldsymbol{q}$–E space, the bi-magnon continuum should instead be bounded from below by the single-magnon dispersion, with a momentum-dependent separation that depends on the single-magnon gap [175]. The bi-magnon cross section will be simulated below, but for now I approximate it with a resolution-convolved arctangent step function that onsets above the magnon peak. Apart from the resolution-limited Gaussian elastic line, the only other feature below 0.4 eV energy loss is the electron-hole exciton, which is fitted with a simple Gaussian.

Representative fits to the spectra at $(0.24, 0.24)$ and $(0.28, 0)$ involving all of the above lineshapes are shown in Fig. 4.13. While there are some discrepancies around the phonon peak and multi-magnon excitations, the single magnon that we are focussed on here is fitted with a well defined energy. Figure 4.14 shows the fitted magnon dispersion, compared to the dispersions

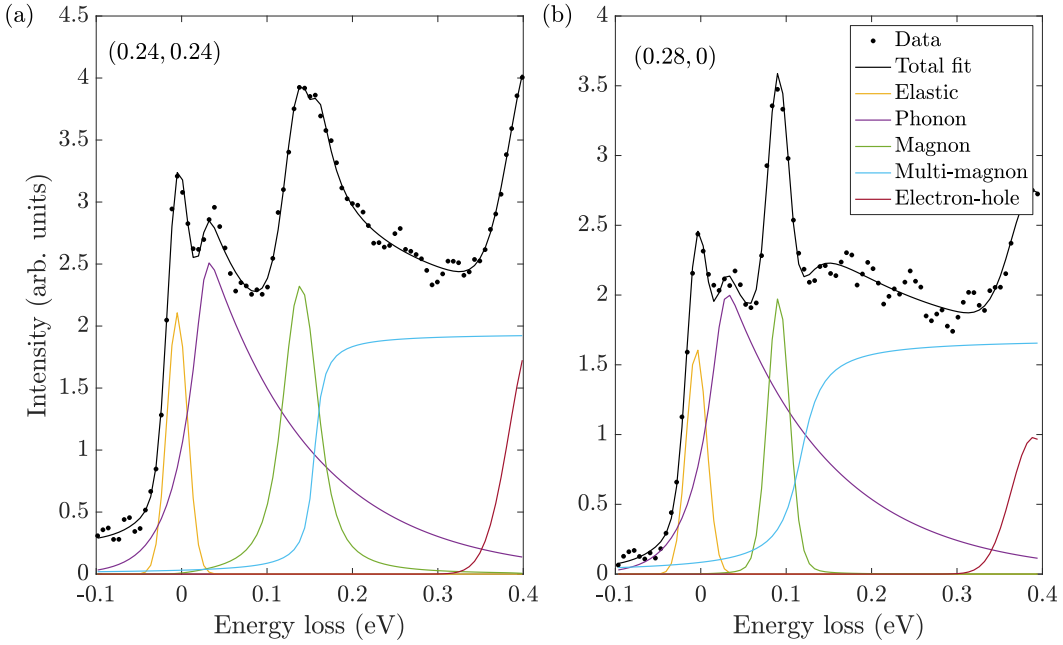

Figure 4.13: Fits (black lines) to the RIXS spectra (points) at the t_{2g} resonance at momentum transfers of (a) $(0.24, 0.24)$ and (b) $(0.28, 0)$. The elastic line is fitted with a resolution-limited Gaussian (yellow lines), the phonon harmonics with a resolution-convolved back-to-back exponential [purple lines, see Fig. 4.8(b)], the magnon with a damped harmonic oscillator lineshape (green lines), the onset of multi-magnon excitations with an arctangent step function (blue lines) and the exciton with a Gaussian (red lines).

determined in previous O K-edge [168] and Ru L_3-edge [176, 141, 177] RIXS studies. The overall trends are in good agreement, with the dispersion extending from a minimum at the zone centre up to $\sim$0.2 eV at $(0.5, 0.5)$ and $\sim$0.1 eV at $(0.5, 0)$. The consistently higher energies in our study arise from our definition of the damped harmonic oscillator lineshape in Eq. (4.7), with the inclusion of the Bose factor and the energy defined by $\sqrt{\omega_0^2 - \gamma^2}$, compared to simple Gaussian, Lorentzian or Voigt lineshapes used in the other studies, with the energy defined by the peak centre. The plot highlights the kinematic restriction at the O K edge compared to the Ir L_3 edge at which the entire Brillouin zone can be accessed. Note that in many studies on Sr_2IrO_4 a larger, rotated Brillouin zone (corresponding to a smaller unit cell with no octahedral rotations and $a = b \approx 3.9$ Å) is used for easy comparison with previous work on the cuprates. The momenta referenced to this cell in conventional units of

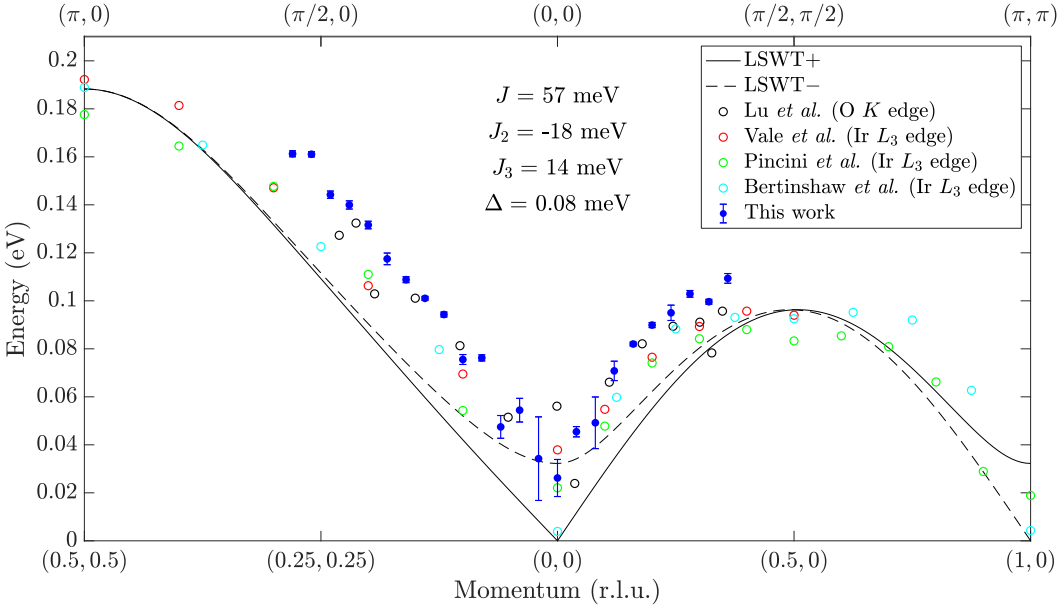

Figure 4.14: Comparison between our magnon dispersion (blue points) and those from previous O K-edge (Lu *et al.* [168], black circles) and Ir L_3-edge (Vale *et al.* [176], red circles, Pincini *et al.* [141], green circles, and Bertinshaw *et al.* [177], cyan circles) studies. The black solid and dashed lines show the LSWT dispersions from a 2DAH model with up to third-neighbour couplings, using the exchange parameters shown (from Vale *et al.* [176]). The top axis shows the reciprocal-space points referenced to a reduced cell with $a = b \approx 3.9$ Å in units of $1/a$.

$1/a$ are shown along the top axis of Fig. 4.14.

Having determined the magnon dispersion, it can now be fitted to the effective magnetic Hamiltonian introduced in Sec. 4.1.1 in order to determine the exchange parameters. The DMI ($\boldsymbol{D}$) and anisotropies due to spin-lattice coupling (Γ_1 and Γ_2) are orders of magnitude smaller than the other terms and cannot be uniquely determined from our data, so will be neglected going forward. In many previous studies, the remaining terms are recast into a two-dimensional anisotropic Heisenberg (2DAH) Hamiltonian [176, 141]

$$H = J \sum_{\langle i,j \rangle} S_i^x S_j^x + S_i^y S_j^y + (1-\Delta) S_i^z S_j^z + J_2 \sum_{\langle\langle i,j \rangle\rangle} \boldsymbol{S}_i \cdot \boldsymbol{S}_j + J_3 \sum_{\langle\langle\langle i,j \rangle\rangle\rangle} \boldsymbol{S}_i \cdot \boldsymbol{S}_j, \quad (4.8)$$

with effective nearest neighbour exchange $J = J_1/(1-\Delta)$, next-nearest and next-next nearest neighbour exchange J_2 and J_3, and in-plane anisotropy

$0 \leq \Delta \leq 1$. Linear spin-wave theory (LSWT) predicts two modes from this Hamiltonian, with dispersions [141]

$$\omega_{\pm}(q_x, q_y) = \sqrt{A(q_x, q_y)^2 - B_{\pm}(q_x, q_y)^2}, \tag{4.9}$$

where

$$A(q_x, q_y) = 2\left[J - J_2 - J_3 + J_2\cos(q_x)\cos(q_y)\right] + J_3\left[\cos(2q_x) + \cos(2q_y)\right] + \frac{J\Delta}{2} \tag{4.10}$$

and

$$B_{\pm}(q_x, q_y) = J\left[\cos(q_x) + \cos(q_y)\right] \pm \frac{J\Delta}{2}. \tag{4.11}$$

A finite anisotropy $\Delta > 0$ results in the two modes being gapped alternately at $(0, 0)$ and $(1, 0)$ [or $(0, 0)$ and (π, π) in the reduced-cell notation], as shown in Fig. 4.14 using the exchange parameters from Vale *et al.* [176]. Notwithstanding the systematic energy scaling between out study and the others, the LSWT dispersion describes the trend of the data reasonably well (note that the un-gapped mode has vanishing intensity at the zone centre and cannot be resolved from the elastic line).

The one feature present in all three Ir L_3-edge studies that is not captured by LSWT is a dip in the dispersion at $(0.5, 0)$ [or $(\pi/2, \pi/2)$] [176, 141, 177]. While the dip consists of only a few outlying points in each dataset, their presence over multiple studies suggests that they are more than random error. The presence of the dip is only commented on in one previous study [177], where the authors suggest that it can be modelled by the inclusion of further-neighbour interactions. Following this suggestion, I add fourth-neighbour interactions to the 2DAH model

$$H \supset J_4 \sum_{\langle\langle\langle\langle i,j\rangle\rangle\rangle\rangle} \boldsymbol{S}_i \cdot \boldsymbol{S}_j, \tag{4.12}$$

which results in LSWT dispersions

$$\omega_{\pm}(q_x, q_y) = \sqrt{A(q_x, q_y)^2 - B_{\pm}(q_x, q_y)^2}, \tag{4.13}$$

with

$$A(q_x, q_y) = 2\left[J - J_2 - J_3 + 2J_4 + J_2\cos(q_x)\cos(q_y)\right] + J_3\left[\cos(2q_x) + \cos(2q_y)\right] + \frac{J\Delta}{2} \tag{4.14}$$

and

$$B_{\pm}(q_x, q_y) = J\left[\cos(q_x) + \cos(q_y)\right] + 2J_4\left[\cos(q_x)\cos(2q_y) + \cos(2q_x)\cos(q_y)\right] \pm \frac{J\Delta}{2}. \tag{4.15}$$

A global fit of this dispersion to all the datasets shown in Fig. 4.14 produces the dispersion shown in Fig. 4.15 along with the best-fit exchange parameters. The addition of fourth-neighbour interactions does indeed reproduce the dip at $(0.5, 0)$, but introduces a further dip around $(0.25, 0.25)$ that is not present in the experimental data. Of course, the dispersion in this region could be refined by the addition of *further*-neighbour interactions, but at this point one has to question the physical motivation of such strong long-range interactions. Recent theoretical calculations by Zhang and Pavarini, involving DFT, dynamical mean-field theory and many-body perturbation theory, propose instead that all exchange interactions beyond nearest neighbour should be <1 meV [178].

An alternative explanation of the shape of the dispersion is provided by theoretical calculations performed by Mohapatra and Singh [179]. Instead of constructing an effective magnetic Hamiltonian, they begin with a three-band Hubbard model for the t_{2g} bands, including up to third-neighbour hopping (with mixed-orbital hopping due to octahedral tilts and rotations), tetragonal crystal field, intra- and inter-orbital Coulomb interaction, Hund's coupling and SOC terms. From this Hubbard Hamiltonian, they self-consistently determine

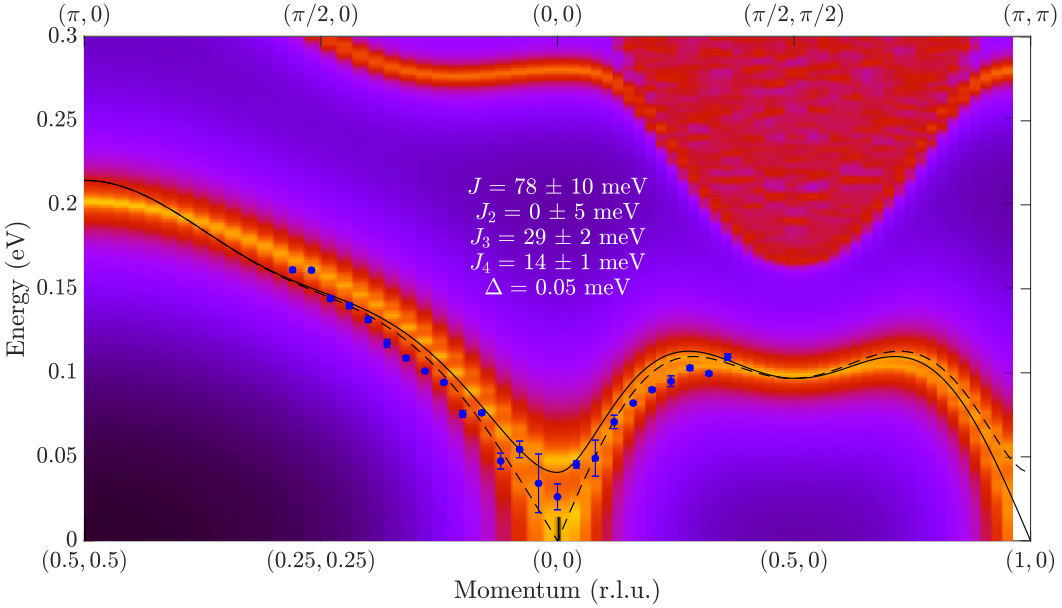

Figure 4.15: Our magnon dispersion (blue points) overlaid on a colourmap of the spectral function from Mohapatra and Singh [179] with intensity on a log scale. LSWT (black solid and dashed lines) is able to reproduce the dip at $(0.5, 0)$ [or $(\pi/2, \pi/2)$ in reduced-cell notation] by adding a fourth-neighbour Heisenberg exchange J_4, but this degrades the agreement around $(0.25, 0.25)$.

the magnetic order and calculate a generalised fluctuation propagator that includes spin, orbital, and coupled spin-orbital fluctuations. As well as magnons, this approach can therefore simultaneously describe the electron-hole and spin-orbit excitons, and crucially the interactions between them. The generalised spectral function is shown as a colourmap in Fig. 4.15. The two magnon modes can be seen dispersing out from the zone centre, in very good agreement with our experimental data. Crucially, the calculations reproduce the dip at $(0.5, 0)$. Above the magnon, a weak spin-orbit exciton mode (note the colourmap is on a log scale) – that arises from the small mixing of $J_{\text{eff}} = 3/2$ character into the $J_{\text{eff}} = 1/2$ states [179] – can be seen dispersing down to a minimum at $(0.5, 0)$. In the calculations, it is in fact the proximity of this mode that pushes down the magnon dispersion. This can be seen by reducing the Hund's coupling (increasing the energy of the spin-orbit exciton) or increasing SOC (reducing the intensity of the spin-orbit exciton), both of which reduce the prominence of the dip. The dip is therefore explained by interactions between the magnon and

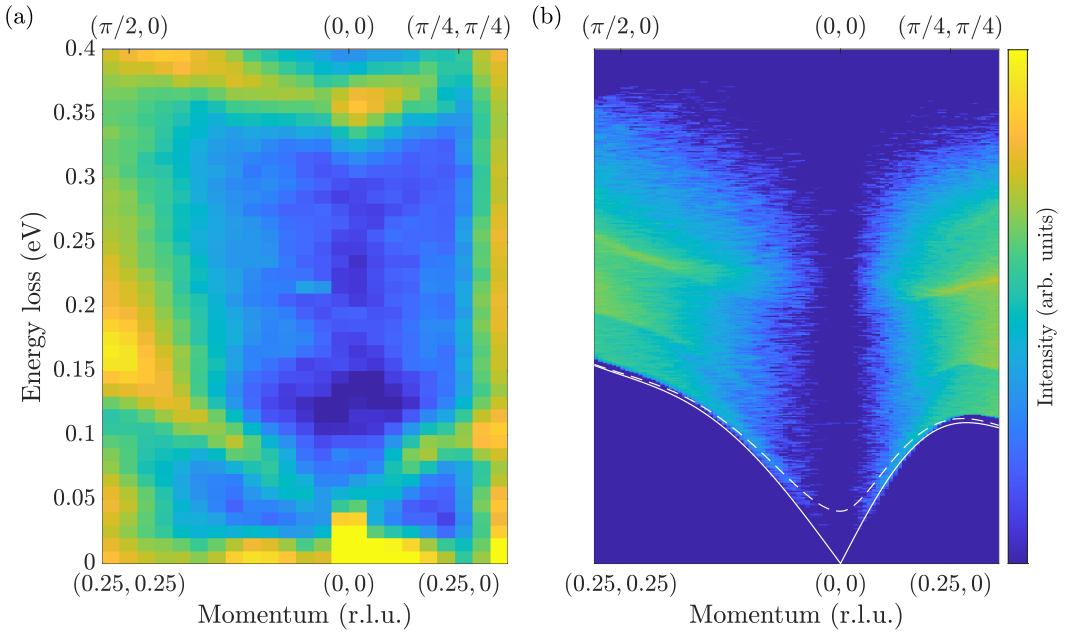

Figure 4.16: (a) RIXS intensity in $\boldsymbol{q}$–E space (colourmap with log scale). (b) Dynamic structure factor for bi-magnons calculated with 10^{11} Monte-Carlo steps using the fourth-neighbour LSWT fit from Fig. 4.15 (colourmap with log scale), overlaid with the single-magnon dispersions (white solid and dashed lines).

spin-orbit exciton, due to the strong orbital character of the former, without the need for further-neighbour exchange interactions (up to third neighbour hopping is included in the calculations, with $|t_3/t_1| = 1/4$). Without the influence of the spin-orbit exciton, the magnon dispersion is more symmetric with similar energies at $(0.5, 0.5)$ and $(0.5, 0)$, bringing the behaviour closer to that of the cuprates [140], and reconciling the observed dispersion with the calculations by Zhang and Pavarini that predict small exchange interactions beyond nearest neighbour [178].

To search for the spin-orbit exciton, I plot our RIXS data as a colourmap in Fig. 4.16(a). While there is intensity above the single magnon, its distribution is not easily identified with that of the spin-orbit exciton in Fig. 4.15. The lack of evidence for the spin-orbit exciton can be explained by two factors: its expected low intensity due to the small mixing of $J_{\text{eff}} = 1/2$ and $3/2$ states, and the aforementioned presence of multi-magnon excitations in the same region of $\boldsymbol{q}$–E space. To determine whether the intensity above the single-magnon

peak can be accounted for by bi-magnon processes, I simulated the longitudinal dynamic structure factor $S^{zz}(\boldsymbol{q},\omega)$ for bi-magnons using a Monte Carlo method previously applied to $NaOsO_3$ [175]. Each Monte-Carlo step consists of the following:

1. Generate two random $\boldsymbol{q}$ vectors, $\boldsymbol{q}_1$ and $\boldsymbol{q}_2$, in the two-dimensional Brillouin zone.

2. Calculate the combined energy of two magnons, $\omega_1 + \omega_2$, at $\boldsymbol{q}_1$ and $\boldsymbol{q}_2$ respectively, and project their total momentum $\boldsymbol{q}_1 + \boldsymbol{q}_2$ back into the first Brillouin zone.

3. Calculate the weight $W(\boldsymbol{q}_1, \boldsymbol{q}_2)$ of the bi-magnon processes at these momenta (see below), normalising by the weight of the most likely event.

4. Generate a uniformly-distributed random number $0 < R < 1$. If $W(\boldsymbol{q}_1, \boldsymbol{q}_2) < R$ then accept the event and add a single unit to $S^{zz}(\boldsymbol{q}_1 + \boldsymbol{q}_2, \omega_1 + \omega_2)$, otherwise reject the event and do nothing.

To calculate the weights I used the results of LSWT, which gives three relevant contributions, $W = W_{cc} + W_{aa} + W_{ca}$, corresponding to the creation of two magnons, the annihilation of two magnons, and mixed magnon creation and annihilation respectively. These are given in terms of Bogoliubov operators $u = \cosh\vartheta$ and $v = \sinh\vartheta$, where $\tanh(2\vartheta) = B/A$, as

$$W_{cc}(\boldsymbol{q}_1, \boldsymbol{q}_2) \propto \frac{1}{2} n(\omega_1)\left[n(\omega_2)+1\right]\left[u(\boldsymbol{q}_1)v(\boldsymbol{q}_2) - v(\boldsymbol{q}_1)u(\boldsymbol{q}_2)\right]^2, \tag{4.16}$$

$$W_{aa}(\boldsymbol{q}_1, \boldsymbol{q}_2) \propto \frac{1}{2} \left[n(\omega_1)+1\right]\left[n(\omega_2)+1\right]\left[u(\boldsymbol{q}_1)v(\boldsymbol{q}_2) - v(\boldsymbol{q}_1)u(\boldsymbol{q}_2)\right]^2, \tag{4.17}$$

$$W_{ca}(\boldsymbol{q}_1, \boldsymbol{q}_2) \propto n(\omega_1)\left[n(\omega_2)+1\right]\left[u(\boldsymbol{q}_1)u(\boldsymbol{q}_2) - v(\boldsymbol{q}_1)v(\boldsymbol{q}_2)\right]^2, \tag{4.18}$$

where the Bose factor $n(\omega) = \left[e^{\omega/(k_B T)} - 1\right]^{-1}$. Figure 4.16(b) shows the dynamic structure factor calculated with 10^{11} Monte-Carlo steps using the fourth-neighbour LSWT fit from Fig. 4.15. We now know that LSWT does not properly describe the magnetic dynamics in Sr_2IrO_4, but it gives a reasonable approximation to the single-magnon dispersion in the region of interest,

such that the kinematic constraints on bi-magnon processes should be approximately correct. We see the bi-magnon continuum onset just above the single magnon and extend up twice the highest magnon energy, as expected, with internal structure due to the further-neighbour interactions and anisotropy. With the further caveat that the RIXS intensity may not be directly proportional to the dynamic structure factor (and that the relation between them will likely depend on the momentum transfer), we can compare the results of the Monte Carlo simulation to our experimental data in Fig. 4.16(a). We see an agreement between the general trends in both, with intensity between the single magnon and electron-hole exciton maximised at the highest momenta, and weak tendrils of intensity extending towards the zone centre. Given the above caveats and our experimental resolution, this agreement supports the interpretation of the additional intensity in our RIXS data being due to bi-magnons.

4.4 Conclusion

This chapter has been focussed on the spin-orbit Mott insulator Sr_2IrO_4 and the interactions between its structural, magnetic and electronic properties, involving comprehensive studies of its low-energy excitations by resonant and non-resonant inelastic x-ray scattering. I started with an IXS study of the lattice dynamics, mapping out the phonon band structure and looking for signs of coupling to other long-range orders. In contrast with previous Raman spectroscopy measurements [137], we saw no changes to the phonons in the parent compound associated with the onset of magnetic ordering. Similarly, in the La-doped compound we saw no anomalies due to CDWs or SDWs.

Having not found any evidence of coupling between phonons and electronic or magnetic order, I then turned to RIXS to investigate the coupling to electronic and magnetic excitations. We probed two resonances in our high-resolution O K-edge RIXS measurements, associated with the Ir t_{2g} and e_g orbitals respectively. Harmonic progressions of phonon excitations could be

seen at both resonances, which I fitted using a two-mode extension of the Ament model by Geondzhian and Gilmore [115]. The t_{2g} and e_g states were both found to be strongly coupled to a $\sim$30 meV phonon mode, as well as higher-energy modes at $\sim$50 meV and $\sim$70 meV respectively, all in good agreement with O modes predicted by our DFT calculations from the IXS study. The EPC strengths we obtain are in good agreement with those determined experimentally [101, 102, 103, 104, 105, 106, 107] and theoretically [171] for the single-layer cuprates, adding another point of similarity between these two material families.

Finally, I analysed the magnon that could also be seen at the t_{2g} resonance. Disentangling the magnon from the overlapping phonon excitations presented a challenge, which was overcome by careful analysis of the lineshapes guided by theoretical considerations [173]. My fitting of the magnon yielded a dispersion in good agreement with previous studies, but uniformly shifted up in energy by $\sim$20 meV due to the different choice of lineshape. A comparison of a number of RIXS studies [176, 141, 177] revealed a previously-overlooked dip in the dispersion that is not captured in the standard LSWT solution of a 2DAH Hamiltonian with up to third-neighbour interactions. While the dip can be reproduced by adding fourth-neighbour interactions in LSWT, a more natural explanation comes from a consideration of the orbital component of the moment and coupling to a weak spin-orbit exciton mode at higher energy [179]. This shows the importance of orbital fluctuations in the moment dynamics, which are lost when moving from the Hubbard model to an effective Heisenberg spin model.

Chapter 5

Conclusions and future work

In this thesis, I have explored the consequences of electron-lattice coupling in a selection of topical 4*d and* 5*d quantum materials. This coupling takes on many forms, from a complex interplay between crystal structure, magnetism and the Fermi surface in* $Ca_3Ru_2O_7$*, to a momentum-dependent interaction between electrons and phonons in* Sr_2IrO_4*. Throughout, I have leveraged the versatility of neutron and x-ray scattering to probe both static order and elementary excitations in these materials, as well as advancing our understanding of the techniques themselves. I have also developed new sample environments that allow precise and continuous tuning of the material properties. In the following sections, I summarise the main results from each experimental chapter, highlighting any new questions that they raise and offering avenues for further investigation.*

5.1 Magneto-elastic coupling in a $4d$ polar metal

Chapter 2 concerned the SRT in the $4d$ polar metal $Ca_3Ru_2O_7$, which was found to be decidedly more complex than previously thought. Our main result was the discovery of cycloidal order in a small temperature region around the SRT, whose structure evolves to interpolate between the collinear end phases. We understood this elegant mechanism of moment reorientation on the basis of symmetry analysis, which showed how the polar lattice symmetry enables a uniform DMI that can drive the formation of the cycloid when the easy-axis anisotropies compete. We also placed this discovery in the context of

previous measurements that found incommensurate magnetism in $Ca_3Ru_2O_7$ under doping [72, 58, 59] and field [57]. In the latter case, we reinterpreted the satellite peaks previously measured with SANS as second harmonics of the fundamental cycloidal peaks, generated by a field-driven phase modulation of the cycloid. To verify this interpretation, we have also attempted to measure the second harmonic peaks in our samples at WISH, but were unable to see a signal due to the low neutron flux at such long wavelengths. A SANS measurement to verify the presence of the second harmonics in our samples is therefore required.

A major open question is whether the presence of cycloidal order at zero field is universal in all $Ca_3Ru_2O_7$ samples. While the ability to detect the first-harmonic satellites in SANS measurements at zero field is hampered by the momentum resolution, the magnetisation data of Sokolov *et al.* suggests that the incommensurate phase is squeezed to an infinitesimal temperature window below 2 T in their samples. This points to the presence of the cycloid at zero field being sample dependent. There are other signs of sample variation in the literature – for instance, T_N ranges from 56 K in many samples (including those used by Sokolov *et al.* [57]) up to 62 K in others (including our own). The most obvious culprit for this variation is slight differences in chemical composition, as it is known that the electronic and magnetic properties of $Ca_3Ru_2O_7$ are extremely sensitive to doping [72, 58, 59]. We found no evidence of impurities or deviations from the ideal stoichiometry in our samples from energy-dispersive x-ray spectroscopy or x-ray diffraction, however, although these methods have a low sensitivity to oxygen. To conclusively answer this question, a number of batches of samples with different oxygen concentrations should be investigated, using wavelength-dispersive x-ray spectroscopy to determine the chemical composition, and transport and magnetometry measurements to correlate this with the electronic and magnetic properties.

The coupling between various degrees of freedom that make the SRT in $Ca_3Ru_2O_7$ interesting also presents a considerable challenge in elucidating its

origin. In this context, our ability to control the cycloid-mediated SRT with strain revealed a key role for the lattice, and motivated the development of a microscopic theoretical model based on the tilting and rotation of the RuO_6 octahedra. Key to this success was the combination of strain tuning and scattering measurements, which gave unprecedented information on the response of the lattice to applied stress. This approach could be extended into a large research program encompassing a wide range of quantum materials. We have already made some progress in this regard, successfully using strain to tune the magnetic properties of the quasi-1D iridate $CaIrO_3$ and the CDW in overdoped $La_{2-x}Sr_xCuO_4$. While transition metal oxides are good candidates for strain tuning due to their finely balanced ground states, I believe that more spectacular effects could be discovered if strain was used to break symmetries (for instance, turning tetragonal materials orthorhombic). This idea has been employed recently in the iron-based superconductors, utilising the fact that strain is the conjugate field to nematicity [83, 84, 85, 86]. Rather than just tuning phases that exist at zero-strain, this approach could generate new phases not seen at equilibrium.

5.2 Probing electron-phonon coupling with resonant inelastic x-ray scattering

Chapter 3 was focussed on the use of RIXS to measure EPC. We chose graphite as a model system with well understood electronic and phononic structures, performing high-resolution RIXS measurements of phonon excitations at the C K edge. By tuning the incident x-ray energy we were able to probe the EPC for both low-energy π^* and high-energy σ^* electronic states, which we found to have highly distinct momentum dependences. This sets RIXS apart as a technique able to probe the EPC of excited states away from the Fermi level. There are a number of material systems to which this technique could be applied, including the new generation of perovskite photovoltaic materials whose efficiencies can be strongly impacted by EPC [94]. Another exciting

possibility would be to use RIXS in a pump-probe modality, allowing the EPC of optically excited states to be probed on ultrafast timescales.

Our work represents a significant step forward in understanding phonon excitations in RIXS, highlighting the need to account for the full phonon dispersion, and the mixing of phonons of different momenta in the intermediate state, when modelling RIXS spectra. The new Green's-function–based model developed by our collaborators allowed these effects to be included with minimal computational cost. There are still many theoretical issues that remain to be resolved, however. The intermediate π^* and σ^* states of graphite are well approximated as localised excitons, but there are many systems in which itinerancy of the excited electron must be accounted for. Initial work suggests that itinerancy can renormalise the phonon features and introduce additional modulations of their intensities as a function of momentum transfer [116]. Incorporating itinerancy into our model is an important next step. Our model also assumed that the phonon frequencies in the intermediate state are equal to those in equilibrium, which seems reasonable but requires further theoretical justification [114]. Finally, the relationship between the coupling probed by RIXS and those probed by other techniques, such as ARPES, remains to be properly quantified. This will likely require a concerted theoretical and experimental effort, involving first-principles calculations to establish the role of the core hole in RIXS and comparative measurements of the EPC in a number of materials using the different techniques.

5.3 Electron-phonon coupling in a $5d$ spin-orbit Mott insulator

Chapter 4 contained a multi-technique study of the low-energy lattice, electronic and magnetic excitations in the $5d$ spin-orbit Mott insulator Sr_2IrO_4. We first used non-resonant IXS to determine the phonon band structure of both parent and electron-doped Sr_2IrO_4, comparing the results to a non-magnetic DFT calculation. No deviations from the DFT predictions due to coupling be-

tween the phonons and magnetic or charge ordering could be seen. There are a number of possible reasons for this, including an insufficient energy resolution, and a vanishing IXS intensity for the modes that show the strongest coupling. While the latter issue could be addressed by measuring across many different Brillouin zones, this is a time-consuming task with no guarantee of success. Another approach to determine the phonon dispersion is thermal diffuse scattering, which has lower resolution and requires more advanced analysis, but allows large regions of reciprocal space to be mapped quickly [180]. This would be an interesting avenue for further exploration, especially in the search for phonon anomalies due to CDW/SDW order as it allows fast measurement over large temperature and doping ranges.

Despite not showing any anomalies, the IXS results did provide a valuable reference for subsequent O K-edge RIXS measurements. Inspired by the graphite measurements of Chapter 3, we probed the EPC at two resonances associated with the t_{2g} and e_g orbitals of Ir (accessible due to O–Ir hybridisation). We found that two different phonon modes were excited at each resonance, matching well with the DFT results. A two-mode extension of the Ament model [115] was used to extract the EPC strengths, which were found to vanish at the zone centre and rise to $\sim$0.1 eV towards the zone boundary. The main drawback of the model used here is that it does not account for the phonon or EPC dispersions, which we know from Chapter 3 can significantly alter the EPC strengths obtained. In this case, the complex electronic and phononic structures of Sr_2IrO_4 prevented the use of the Green's-function–based model. As we know from the IXS measurements that the phonons are well described by standard DFT, however, first-principles calculations of the EPC could potentially be used to constrain the parameter space and make the problem tractable.

The strong O–Ir hybridisation in Sr_2IrO_4 also enabled the magnon to be seen at the t_{2g} resonance, although the fact that it dispersed through the phonon excitations made it difficult to disentangle their spectral weights. In

this case, a determination of the magnon dispersion was achieved through careful fitting of the different lineshapes. Recent advances in instrumentation have allowed the development of polarisation-resolved RIXS [169], which will make this effort significantly easier in the future. It will allow the different excitations to be separated due to the fact that the magnon and phonons appear in different polarisation channels, and will further aid in the identification of the different phonon modes based on their symmetries.

A comparison of the extracted magnon dispersion with that from other O K-edge and Ir L-edge RIXS studies revealed the inadequacy of previous LSWT descriptions of the spin dynamics. A dip in the dispersion was instead found to be reproduced by Hubbard model calculations including both spin and orbital fluctuations, where it arose from interactions of the magnon with a higher-energy spin-orbit exciton [179]. An intriguing question posed by this realisation is whether the magnon dispersion can be brought closer to the predictions of an isotropic Heisenberg model by disrupting the spin-orbit exciton. Indeed, recent measurements on Sr_2IrO_4 thin films show that epitaxial strain increases the energy of the spin-orbit exciton, and simultaneously reduces the magnitude of second- and third-neighbour interactions needed to reproduce the magnon dispersion with LSWT [170]. While the choice of thin-film substrate allows discrete strains to be applied, a more powerful approach would be to continuously tune the exciton using the Razorbill strain cells. This would require the integration of the strain cells into an inelastic scattering beamline, such as ID20 at the European Synchrotron Radiation Facility. Much of the setup used at I16 could be directly copied across, however, and the small sample size needed for RIXS would allow high strains on the order of 1% to be achieved. If the magnon can be brought close to the isotropic Heisenberg limit, a particularly interesting route would be to combine this approach with chemical doping, which may reveal more cuprate-like physics in the iridates.

Bibliography

[1] M. Imada, A. Fujimori, and Y. Tokura, *Metal-insulator transitions*, Rev. Mod. Phys. **70**, 1039 (1998).

[2] W. Witczak-Krempa, G. Chen, Y. B. Kim, and L. Balents, *Correlated quantum phenomena in the strong spin-orbit regime*, Annu. Rev. Condens. Matter Phys. **5**, 57 (2014).

[3] M. Z. Hasan and C. L. Kane, *Colloquium: topological insulators*, Rev. Mod. Phys. **82**, 3045 (2010).

[4] B. Yan and C. Felser, *Topological materials: Weyl semimetals*, Annu. Rev. Condens. Matter Phys **8**, 337 (2017).

[5] A. Sekine and K. Nomura, *Axion electrodynamics in topological materials*, J. Appl. Phys. **129**, 141101 (2021).

[6] M. Sigrist, *Ruthenates: unconventional superconductivity and magnetic properties*, in *Concepts in electron correlation*, edited by H. A. C. and Z. V., NATO Science Series (Series II: Mathematics, Physics and Chemistry), Vol. 110, pp. 27–34, Springer, Dordrecht, 2003.

[7] J. G. Rau, E. K.-H. Lee, and H.-Y. Kee, *Spin-orbit physics giving rise to novel phases in correlated systems: Iridates and related materials*, Annu. Rev. Condens. Matter Phys **7**, 195 (2016).

[8] M. T. Hutchings, *Point-charge calculations of energy levels of magnetic ions in crystalline electric fields*, Solid State Phys. **16**, 227 (1964).

[9] E. P. Wigner, *On the matrices which reduce the Kronecker products of representations of S. R. groups*, in *The collected works of Eugene Paul Wigner*, edited by A. S. Wightman, Vol. A, pp. 608–654, Springer, Berlin, Heidelberg, 1993.

[10] D. I. Khomskii, *Transition metal compounds* (Cambridge University Press, Cambridge, 2014).

[11] D. van der Marel and G. A. Sawatzky, *Electron-electron interaction and localization in d and f transition metals*, Phys. Rev. B **37**, 10674 (1988).

[12] G. Jackeli and G. Khaliullin, *Mott insulators in the strong spin-orbit coupling limit: from Heisenberg to a quantum compass and Kitaev models*, Phys. Rev. Lett. **102**, 017205 (2009).

[13] J. Hubbard and B. H. Flowers, *Electron correlations in narrow energy bands*, Proc. Roy. Soc. London Ser. A **276**, 238 (1963).

[14] P. W. Anderson, *New approach to the theory of superexchange interactions*, Phys. Rev. **115**, 2 (1959).

[15] A. Kitaev, *Anyons in an exactly solved model and beyond*, Annals of Physics **321**, 2 (2006).

[16] A. Banerjee, C. A. Bridges, J.-Q. Yan, A. A. Aczel, L. Li, M. B. Stone, G. E. Granroth, M. D. Lumsden, Y. Yiu, J. Knolle, S. Bhattacharjee, D. L. Kovrizhin, R. Moessner, D. A. Tennant, D. G. Mandrus, and S. E. Nagler, *Proximate Kitaev quantum spin liquid behaviour in a honeycomb magnet*, Nature Mater. **15**, 733 (2016).

[17] T. Takayama, A. Kato, R. Dinnebier, J. Nuss, H. Kono, L. S. I. Veiga, G. Fabbris, D. Haskel, and H. Takagi, *Hyperhoneycomb iridate* $\beta-Li_2IrO_3$ *as a platform for Kitaev magnetism*, Phys. Rev. Lett. **114**, 077202 (2015).

[18] S. Hwan Chun, J.-W. Kim, J. Kim, H. Zheng, C. Stoumpos, C. Malliakas, J. Mitchell, K. Mehlawat, Y. Singh, Y. Choi, T. Gog, A. Al-Zein, M. Moretti Sala, M. Krisch, J. Chaloupka, G. Jackeli, G. Khaliullin, and B. J. Kim, *Direct evidence for dominant bond-directional interactions in a honeycomb lattice iridate* Na_2IrO_3, Nature Phys. **11**, 462 (2015).

[19] G. L. Squires, *Introduction to the theory of thermal neutron scattering* (Cambridge University Press, New York, 1978).

[20] A. Q. R. Baron, *Phonons in crystals using inelastic x-ray scattering*, J. Spectrosc. Soc. Japan **58**, 205 (2009).

[21] M. Altarelli, *Resonant x-ray scattering: a theoretical introduction*, in *Magnetism: A Synchrotron Radiation Approach*, edited by E. Beaurepaire, H. Bulou, F. Scheurer, and J.-P. Kappler, pp. 201–242, Springer, Berlin, Heidelberg, 2006.

[22] L. C. Chapon, P. Manuel, P. G. Radaelli, C. Benson, L. Perrott, S. Ansell, N. J. Rhodes, D. Raspino, D. Duxbury, E. Spill, and J. Norris, *Wish: the new powder and single crystal magnetic diffractometer on the second target station*, Neutron News **22**, 22 (2011).

[23] A. Q. R. Baron, *RIKEN quantum nanodynamics beamline (BL43LXU): the next generation for inelastic x-ray scattering*, SPring-8 Inf. Newsl. **15**, 14 (2010).

[24] J. P. Hill and D. F. Mcmorrow, *X-ray resonant exchange scattering: polarization dependence and correlation functions*, Acta Cryst., Sect. A **52**, 236 (1996).

[25] S. P. Collins, A. Bombardi, A. R. Marshall, J. H. Williams, G. Barlow, A. G. Day, M. R. Pearson, R. J. Woolliscroft, R. D. Walton, G. Beutier, and G. Nisbet, *Diamond beamline I16 (materials & magnetism)*, AIP Conference Proceedings **1234**, 303 (2010).

[26] K.-J. Zhou, A. Walters, M. Garcia-Fernandez, T. Rice, M. Hand, A. Nag, J. Li, S. Agrestini, P. Garland, H. Wang, S. Alcock, I. Nistea, B. Nutter, N. Rubies, G. Knap, M. Gaughran, F. Yuan, P. Chang, J. Emmins, and G. Howell, *I21: an advanced high-resolution resonant inelastic x-ray scattering beamline at Diamond Light Source*, J. Synchrotron Rad. **29**, 563 (2022).

[27] Y. Maeno, H. Hashimoto, K. Yoshida, S. Nishizaki, T. Fujita, J. G. Bednorz, and F. Lichtenberg, *Superconductivity in a layered perovskite without copper*, Nature **372**, 532 (1994).

[28] M. Braden, G. André, S. Nakatsuji, and Y. Maeno, *Crystal and magnetic structure of Ca_2RuO_4: magnetoelastic coupling and the metal-insulator transition*, Phys. Rev. B **58**, 847 (1998).

[29] S. Nakatsuji and Y. Maeno, *Quasi-two-dimensional Mott transition system $Ca_{2-x}Sr_xRuO_4$*, Phys. Rev. Lett. **84**, 2666 (2000).

[30] F. Nakamura, T. Goko, M. Ito, T. Fujita, S. Nakatsuji, H. Fukazawa, Y. Maeno, P. Alireza, D. Forsythe, and S. R. Julian, *From Mott insulator to ferromagnetic metal: a pressure study of Ca_2RuO_4*, Phys. Rev. B **65**, 220402 (2002).

[31] S. Riccò, M. Kim, A. Tamai, S. McKeown Walker, F. Y. Bruno, I. Cucchi, E. Cappelli, C. Besnard, T. K. Kim, P. Dudin, M. Hoesch, M. J. Gutmann, A. Georges, R. S. Perry, and F. Baumberger, *Insitu strain tuning of the metal-insulator-transition of Ca_2RuO_4 in angle-resolved photoemission experiments*, Nat. Commun. **9**, 4535 (2018).

[32] C. H. Mousatov, E. Berg, and S. A. Hartnoll, *Theory of the strange metal $Sr_3Ru_2O_7$*, Proc. Natl. Acad. Sci. U.S.A. **117**, 2852 (2020).

[33] C. Lester, S. Ramos, R. S. Perry, T. P. Croft, R. I. Bewley, T. Guidi, P. Manuel, D. D. Khalyavin, E. Forgan, and S. M. Hayden, *Field-tunable spin-density-wave phases in $Sr_3Ru_2O_7$*, Nat. Mater. **14**, 373 (2015).

[34] G. Cao, S. McCall, J. E. Crow, and R. P. Guertin, *Observation of a metallic antiferromagnetic phase and metal to nonmetal transition in $Ca_3Ru_2O_7$*, Phys. Rev. Lett. **78**, 1751 (1997).

[35] Y. Yoshida, S.-I. Ikeda, H. Matsuhata, N. Shirakawa, C. H. Lee, and S. Katano, *Crystal and magnetic structure of $Ca_3Ru_2O_7$*, Phys. Rev. B **72**, 054412 (2005).

[36] D. Puggioni, M. Horio, J. Chang, and J. M. Rondinelli, *Cooperative interactions govern the fermiology of the polar metal $Ca_3Ru_2O_7$*, Phys. Rev. Research **2**, 023141 (2020).

[37] T. Moriya, *Anisotropic superexchange interaction and weak ferromagnetism*, Phys. Rev. **120**, 91 (1960).

[38] I. E. Dzyaloshinskii, *A thermodynamic theory of weak ferromagnetism of antiferromagnetics*, J. Phys. Chem. Solids **4**, 241 (1958).

[39] N. A. Hill, *Why are there so few magnetic ferroelectrics?*, J. Phys. Chem. B **104**, 6694 (2000).

[40] N. A. Spaldin and M. Fiebig, *The renaissance of magnetoelectric multiferroics*, Science **309**, 391 (2005).

[41] K. Daniel, *Classifying multiferroics: mechanisms and effects*, Physics **2**, 20 (2009).

[42] J. B. Neaton, C. Ederer, U. V. Waghmare, N. A. Spaldin, and K. M. Rabe, *First-principles study of spontaneous polarization in multiferroic $BiFeO_3$*, Phys. Rev. B **71**, 014113 (2005).

[43] S.-W. Cheong and M. Mostovoy, *Multiferroics: a magnetic twist for ferroelectricity*, Nat. Mater. **6**, 13 (2007).

[44] T. Kimura, T. Goto, H. Shintani, K. Ishizaka, T. Arima, and Y. Tokura, *Magnetic control of ferroelectric polarization*, Nature **426**, 55 (2003).

[45] P. W. Anderson and E. I. Blount, *Symmetry Considerations on Martensitic Transformations: "Ferroelectric" Metals?*, Phys. Rev. Lett. **14**, 217 (1965).

[46] Y. Shi, Y. Guo, X. Wang, A. J. Princep, D. D. Khalyavin, P. Manuel, Y. Michiue, A. Sato, K. Tsuda, S. Yu, M. Arai, Y. Shirako, M. Akaogi, N. Wang, K. Yamaura, and A. T. Boothroyd, *A ferroelectric-like structural transition in a metal*, Nat. Mater. **12**, 1024 (2013).

[47] T. H. Kim, D. Puggioni, Y. Yuan, L. Xie, H. Zhou, N. Campbell, P. J. Ryan, Y. Choi, J.-W. Kim, J. R. Patzner, S. Ryu, J. P. Podkaminer, J. Irwin, Y. Ma, C. J. Fennie, M. S. Rzchowski, X. Q. Pan, V. Gopalan, J. M. Rondinelli, and C. B. Eom, *Polar metals by geometric design*, Nature **533**, 68 (2016).

[48] S. Lei, M. Gu, D. Puggioni, G. Stone, J. Peng, J. Ge, Y. Wang, B. Wang, Y. Yuan, K. Wang, Z. Mao, J. M. Rondinelli, and V. Gopalan, *Observation of quasi-two-dimensional polar domains and ferroelastic switching in a metal,* $Ca_3Ru_2O_7$, Nano Lett. **18**, 3088 (2018).

[49] F. J. Morin, *Magnetic susceptibility of* α*-*Fe_2O_3 *and* α*-*Fe_2O_3 *with added titanium*, Phys. Rev. **78**, 819 (1950).

[50] C. G. Shull, W. A. Strauser, and E. O. Wollan, *Neutron diffraction by paramagnetic and antiferromagnetic substances*, Phys. Rev. **83**, 333 (1951).

[51] N. Kikugawa, A. W. Rost, C. W. Hicks, A. J. Schofield, and A. P. Mackenzie, $Ca_3Ru_2O_7$*: density wave formation and quantum oscillations in the Hall resistivity*, J. Phys. Soc. Jpn. **79**, 024704 (2010).

[52] G. Cao, X. N. Lin, L. Balicas, S. Chikara, J. E. Crow, and P. Schlottmann, *Orbitally driven behaviour: Mott transition, quantum oscillations and colossal magnetoresistance in bilayered* $Ca_3Ru_2O_7$, New J. Phys. **6**, 159 (2004).

[53] B. Bohnenbuck, I. Zegkinoglou, J. Strempfer, C. Schüßler-Langeheine, C. S. Nelson, P. Leininger, H.-H. Wu, E. Schierle, J. C. Lang, G. Srajer, S. I. Ikeda, Y. Yoshida, K. Iwata, S. Katano, N. Kikugawa, and

B. Keimer, *Magnetic structure and orbital state of $Ca_3Ru_2O_7$ investigated by resonant x-ray diffraction*, Phys. Rev. B **77**, 224412 (2008).

[54] F. Baumberger, N. J. C. Ingle, N. Kikugawa, M. A. Hossain, W. Meevasana, R. S. Perry, K. M. Shen, D. H. Lu, A. Damascelli, A. Rost, A. P. Mackenzie, Z. Hussain, and Z.-X. Shen, *Nested Fermi Surface and electronic instability in $Ca_3Ru_2O_7$*, Phys. Rev. Lett. **96**, 107601 (2006).

[55] M. Horio, Q. Wang, V. Granata, K. P. Kramer, Y. Sassa, S. Jöhr, D. Sutter, A. Bold, L. Das, Y. Xu, R. Frison, R. Fittipaldi, T. K. Kim, C. Cacho, J. E. Rault, P. Le Fèvre, F. Bertran, N. C. Plumb, M. Shi, A. Vecchione, M. H. Fischer, and J. Chang, *Electron-driven C_2-symmetric Dirac semimetal uncovered in $Ca_3Ru_2O_7$*, npj Quantum Mater. **6**, 29 (2021).

[56] I. Marković, M. D. Watson, O. J. Clark, F. Mazzola, E. Abarca Morales, C. A. Hooley, H. Rosner, C. M. Polley, T. Balasubramanian, S. Mukherjee, N. Kikugawa, D. A. Sokolov, A. P. Mackenzie, and P. D. C. King, *Electronically driven spin-reorientation transition of the correlated polar metal $Ca_3Ru_2O_7$*, Proc. Natl. Acad. Sci. U.S.A. **117**, 15524 (2020).

[57] D. A. Sokolov, N. Kikugawa, T. Helm, H. Borrmann, U. Burkhardt, R. Cubitt, J. S. White, E. Ressouche, M. Bleuel, K. Kummer, A. P. Mackenzie, and U. K. Rößler, *Metamagnetic texture in a polar antiferromagnet*, Nat. Phys. **15**, 671 (2019).

[58] X. Ke, J. Peng, W. Tian, T. Hong, M. Zhu, and Z. Q. Mao, *Commensurate-incommensurate magnetic phase transition in the Fe-doped bilayer ruthenate $Ca_3Ru_2O_7$*, Phys. Rev. B **89**, 220407(r) (2014).

[59] M. Zhu, J. Peng, W. Tian, T. Hong, Z. Q. Mao, and X. Ke, *Tuning the competing phases of bilayer ruthenate $Ca_3Ru_2O_7$ via dilute Mn impurities and magnetic field*, Phys. Rev. B **95**, 144426 (2017).

[60] S. Lei, S. Chikara, D. Puggioni, J. Peng, M. Zhu, M. Gu, W. Zhao, Y. Wang, Y. Yuan, H. Akamatsu, M. H. W. Chan, X. Ke, Z. Mao, J. M. Rondinelli, M. Jaime, J. Singleton, F. Weickert, V. S. Zapf, and V. Gopalan, *Comprehensive magnetic phase diagrams of the polar metal* $Ca_3(Ru_{0.95}Fe_{0.05})_2O_7$, Phys. Rev. B **99**, 224411 (2019).

[61] C. D. Dashwood, L. S. I. Veiga, Q. Faure, J. G. Vale, D. G. Porter, S. P. Collins, P. Manuel, D. D. Khalyavin, F. Orlandi, R. S. Perry, R. D. Johnson, and D. F. McMorrow, *Spontaneous cycloidal order mediating a spin-reorientation transition in a polar metal*, Phys. Rev. B **102**, 180410 (2020).

[62] O. Arnold, J. C. Bilheux, J. M. Borreguero, A. Buts, S. I. Campbell, L. Chapon, M. Doucet, N. Draper, R. Ferraz Leal, M. A. Gigg, V. E. Lynch, A. Markvardsen, D. Mikkelson, R. L. Mikkelson, R. Miller, K. Palmen, P. Parker, G. Passos, T. G. Perring, P. F. Peterson, S. Ren, M. A. Reuter, A. T. Savici, J. W. Taylor, R. J. Taylor, R. Tolchenov, W. Zhou, and J. Zikovsky, *Mantid–Data analysis and visualization package for neutron scattering and* μSR *experiments*, Nucl. Instrum. Methods Phys. Res., Sect. A **764**, 156 (2014).

[63] D. G. Porter, Py16, `https://doi.org/10.5281/zenodo.3859719`.

[64] W. Bao, Z. Q. Mao, Z. Qu, and J. W. Lynn, *Spin valve effect and magnetoresistivity in single crystalline* $Ca_3Ru_2O_7$, Phys. Rev. Lett. **100**, 247203 (2008).

[65] J. M. Tranquada, B. J. Sternlieb, J. D. Axe, Y. Nakamura, and S. Uchida, *Evidence for stripe correlations of spins and holes in copper oxide superconductors*, Nature **375**, 561 (1995).

[66] Y. Ishikawa, K. Tajima, D. Bloch, and M. Roth, *Helical spin structure in manganese silicide MnSi*, Solid State Commun. **19**, 525 (1976).

[67] I. Sosnowska and A. K. Zvezdin, *Origin of the long period magnetic ordering in $BiFeO_3$*, J. Magn. Magn. Mater. **140-144**, 167 (1995).

[68] L. Chapon, MagneticX, `https://forge.epn-campus.eu/projects/magnetix`.

[69] Y. A. Izyumov and V. N. Syromyatnikov, *Phase transitions and crystal symmetry* (Springer, 1990).

[70] A. M. Kadomtseva, A. K. Zvezdin, Y. F. Popov, A. P. Pyatakov, and G. P. Vorob'ev, *Space-time parity violation and magnetoelectric interactions in antiferromagnets*, J. Exp. Theor. Phys. Lett. **79**, 571 (2004).

[71] Y. Togawa, T. Koyama, K. Takayanagi, S. Mori, Y. Kousaka, J. Akimitsu, S. Nishihara, K. Inoue, A. S. Ovchinnikov, and J. Kishine, *Chiral magnetic soliton lattice on a chiral helimagnet*, Phys. Rev. Lett. **108**, 107202 (2012).

[72] J. Peng, X. Ke, G. Wang, J. E. Ortmann, D. Fobes, T. Hong, W. Tian, X. Wu, and Z. Q. Mao, *From quasi-two-dimensional metal with ferromagnetic bilayers to Mott insulator with G-type antiferromagnetic order in $Ca_3(Ru_{1-x}Ti_x)_2O_7$*, Phys. Rev. B **87**, 085125 (2013).

[73] G. Cao, L. Balicas, Y. Xin, J. E. Crow, and C. S. Nelson, *Quantum oscillations, colossal magnetoresistance, and the magnetoelastic interaction in bilayered $Ca_3Ru_2O_7$*, Phys. Rev. B **67**, 184405 (2003).

[74] Y. Yoshida, S.-I. Ikeda, N. Shirakawa, M. Hedo, and Y. Uwatoko, *Magnetic properties of Ca_2RuO_4 under uniaxial pressures*, J. Phys. Soc. Jpn. **77**, 093702 (2008).

[75] W. J. Duncan, O. P. Welzel, D. Moroni-Klementowicz, C. Albrecht, P. G. Niklowitz, D. Gruener, M. Brando, A. Neubauer, C. Pfleiderer, N. Kikugawa, A. P. Mackenzie, and F. M. Grosche, *Quantum phase transitions in $NbFe_2$ and $Ca_3Ru_2O_7$*, Physica Status Solidi. B **247**, 544 (2010).

[76] H. Zhao, H. Zheng, J. Terzic, W. Song, Y. Ni, Y. Zhang, P. Schlottmann, and G. Cao, *Lattice flexibility in $Ca_3Ru_2O_7$: control of electrical transport via anisotropic magnetostriction*, Phys. Rev. B **104**, L121119 (2021).

[77] Razorbill Instruments, `https://razorbillinstruments.com`.

[78] C. W. Hicks, M. E. Barber, S. D. Edkins, D. O. Brodsky, and A. P. Mackenzie, *Piezoelectric-based apparatus for strain tuning*, Rev. Sci. Instrum. **85**, 065003 (2014).

[79] C. W. Hicks, D. O. Brodsky, E. A. Yelland, A. S. Gibbs, J. A. N. Bruin, M. E. Barber, S. D. Edkins, K. Nishimura, S. Yonezawa, Y. Maeno, and A. P. Mackenzie, *Strong increase of T_C of Sr_2RuO_4 under both tensile and compressive strain*, Science **344**, 283 (2014).

[80] A. Steppke, L. Zhao, M. E. Barber, T. Scaffidi, F. Jerzembeck, H. Rosner, A. S. Gibbs, Y. Maeno, S. H. Simon, A. P. Mackenzie, and C. W. Hicks, *Strong peak in T_C of Sr_2RuO_4 under uniaxial pressure*, Science **355**, eaaf9398 (2017).

[81] H.-H. Kim, S. M. Souliou, M. E. Barber, E. Lefrançois, M. Minola, M. Tortora, R. Heid, N. Nandi, R. A. Borzi, G. Garbarino, A. Bosak, J. Porras, T. Loew, M. König, P. J. W. Moll, A. P. Mackenzie, B. Keimer, C. W. Hicks, and M. Le Tacon, *Uniaxial pressure control of competing orders in a high-temperature superconductor*, Science **362**, 1040 (2018).

[82] H.-H. Kim, E. Lefrançois, K. Kummer, R. Fumagalli, N. B. Brookes, D. Betto, S. Nakata, M. Tortora, J. Porras, T. Loew, M. E. Barber, L. Braicovich, A. P. Mackenzie, C. W. Hicks, B. Keimer, M. Minola, and M. Le Tacon, *Charge density waves in $YBa_2Cu_3O_{6.67}$ probed by resonant x-ray scattering under uniaxial compression*, Phys. Rev. Lett. **126**, 037002 (2021).

[83] M. S. Ikeda, T. Worasaran, J. C. Palmstrom, J. A. W. Straquadine, P. Walmsley, and I. R. Fisher, *Symmetric and antisymmetric strain as*

continuous tuning parameters for electronic nematic order, Phys. Rev. B **98**, 245133 (2018).

[84] J. M. Bartlett, A. Steppke, S. Hosoi, H. Noad, J. Park, C. Timm, T. Shibauchi, A. P. Mackenzie, and C. W. Hicks, *Relationship between transport anisotropy and nematicity in FeSe*, Phys. Rev. X **11**, 021038 (2021).

[85] M. Ghini, M. Bristow, J. C. A. Prentice, S. Sutherland, S. Sanna, A. A. Haghighirad, and A. I. Coldea, *Strain tuning of nematicity and superconductivity in single crystals of FeSe*, Phys. Rev. B **103**, 205139 (2021).

[86] T. Worasaran, M. S. Ikeda, J. C. Palmstrom, J. A. W. Straquadine, S. A. Kivelson, and I. R. Fisher, *Nematic quantum criticality in an Fe-based superconductor revealed by strain-tuning*, Science **372**, 973 (2021).

[87] M. J. Mehl and D. A. Papaconstantopoulos, *Applications of a tight-binding total-energy method for transition and noble metals: elastic constants, vacancies, and surfaces of monatomic metals*, Phys. Rev. B **54**, 4519 (1996).

[88] O. Gunnarsson, M. Calandra, and J. E. Han, *Colloquium: saturation of electrical resistivity*, Rev. Mod. Phys. **75**, 1085 (2003).

[89] H. Fröhlich, *On the theory of superconductivity: the one-dimensional case*, Proc. R. Soc. Lond. A **223**, 296 (1954).

[90] J. Bardeen, L. N. Cooper, and J. R. Schrieffer, *Theory of superconductivity*, Phys. Rev. **108**, 1175 (1957).

[91] J. Zhou, H. D. Shin, K. Chen, B. Song, R. A. Duncan, Q. Xu, A. A. Maznev, K. A. Nelson, and G. Chen, *Direct observation of large electron-phonon interaction effect on phonon heat transport*, Nat. Commun. **11**, 6040 (2020).

[92] Z. Yao, C. L. Kane, and C. Dekker, *High-field electrical transport in single-wall carbon nanotubes*, Phys. Rev. Lett. **84**, 2941 (2000).

[93] D. Novko and M. Kralj, *Phonon-assisted processes in the ultraviolet-transient optical response of graphene*, npj 2D Mater. Appl. **3**, 48 (2019).

[94] A. D. Wright, C. Verdi, R. L. Milot, G. E. Eperon, M. A. Pérez-Osorio, H. J. Snaith, F. Giustino, M. B. Johnston, and L. M. Herz, *Electron-phonon coupling in hybrid lead halide perovskites*, Nat. Commun. **7**, 11755 (2016).

[95] L. Pintschovius, *Electron-phonon coupling effects explored by inelastic neutron scattering*, Phys. status solidi **242**, 30 (2005).

[96] S. Piscanec, M. Lazzeri, F. Mauri, A. C. Ferrari, and J. Robertson, *Kohn anomalies and electron-phonon interactions in hraphite*, Phys. Rev. Lett. **93**, 185503 (2004).

[97] A. C. Ferrari, *Raman spectroscopy of graphene and graphite: disorder, electron-phonon coupling, doping and nonadiabatic effects*, Solid State Communications **143**, 47 (2007).

[98] S.-I. Tanaka, M. Matsunami, and S.-I. Kimura, *An investigation of electron-phonon coupling via phonon dispersion measurements in graphite using angle-resolved photoelectron spectroscopy*, Sci. Rep. **3**, 3031 (2013).

[99] H. Yavaş, M. van Veenendaal, J. van den Brink, L. J. P. Ament, A. Alatas, B. M. Leu, M.-O. Apostu, N. Wizent, G. Behr, W. Sturhahn, H. Sinn, and E. E. Alp, *Observation of phonons with resonant inelastic x-ray scattering*, J. Phys. Condens. Matter **22**, 485601 (2010).

[100] L. J. P. Ament, M. van Veenendaal, and J. van den Brink, *Determining the electron-phonon coupling strength from resonant inelastic x-ray scattering at transition metal L-edges*, Europhys. Lett. **95**, 27008 (2011).

[101] W. S. Lee, S. Johnston, B. Moritz, J. Lee, M. Yi, K. J. Zhou, T. Schmitt, L. Patthey, V. Strocov, K. Kudo, Y. Koike, J. van den Brink, T. P. Devereaux, and Z. X. Shen, *Role of lattice coupling in establishing electronic and magnetic properties in quasi-one-dimensional cuprates*, Phys. Rev. Lett. **110**, 265502 (2013).

[102] J. J. Lee, B. Moritz, W. S. Lee, M. Yi, C. J. Jia, A. P. Sorini, K. Kudo, Y. Koike, K. J. Zhou, C. Monney, V. Strocov, L. Patthey, T. Schmitt, T. P. Devereaux, and Z. X. Shen, *Charge-orbital-lattice coupling effects in the dd excitation profile of one-dimensional cuprates*, Phys. Rev. B **89**, 41104 (2014).

[103] S. Johnston, C. Monney, V. Bisogni, K. Zhou, R. Kraus, G. Behr, V. N. Strocov, J. Málek, S.-L. Drechsler, J. Geck, T. Schmitt, and J. van den Brink, *Electron-lattice interactions strongly renormalize the charge-transfer energy in the spin-chain cuprate* Li_2CuO_2, Nat. Commun. **7**, 10563 (2016).

[104] M. Rossi, R. Arpaia, R. Fumagalli, M. Moretti Sala, D. Betto, K. Kummer, G. M. De Luca, J. van den Brink, M. Salluzzo, N. B. Brookes, L. Braicovich, and G. Ghiringhelli, *Experimental determination of momentum-resolved electron-phonon coupling*, Phys. Rev. Lett. **123**, 027001 (2019).

[105] L. Braicovich, M. Rossi, R. Fumagalli, Y. Peng, Y. Wang, R. Arpaia, D. Betto, G. M. De Luca, D. Di Castro, K. Kummer, M. Moretti Sala, M. Pagetti, G. Balestrino, N. B. Brookes, M. Salluzzo, S. Johnston, J. van den Brink, and G. Ghiringhelli, *Determining the electron-phonon coupling in superconducting cuprates by resonant inelastic x-ray scattering: methods and results on* $Nd_{1+x}Ba_{2-x}Cu_3O_{7-\delta}$, Phys. Rev. Research **2**, 023231 (2020).

[106] J. Li, A. Nag, J. Pelliciari, H. Robarts, A. Walters, M. Garcia-Fernandez, H. Eisaki, D. Song, H. Ding, S. Johnston, R. Comin, and K.-J. Zhou, *Multiorbital charge-density wave excitations and concomitant phonon anomalies in* $Bi_2Sr_2LaCuO_{6+\delta}$, Proc. Natl. Acad. Sci. U.S.A. **117**, 16219 (2020).

[107] Y. Y. Peng, A. A. Husain, M. Mitrano, S. X.-L. Sun, T. A. Johnson, A. V. Zakrzewski, G. J. MacDougall, A. Barbour, I. Jarrige, V. Bisogni, and P. Abbamonte, *Enhanced electron-phonon coupling for charge-density-wave formation in* $La_{1.8-x}Eu_{0.2}Sr_xCuO_{4+\delta}$, Phys. Rev. Lett. **125**, 097002 (2020).

[108] S. Moser, S. Fatale, P. Krüger, H. Berger, P. Bugnon, A. Magrez, H. Niwa, J. Miyawaki, Y. Harada, and M. Grioni, *Electron-phonon coupling in the bulk of anatase* TiO_2 *measured by resonant inelastic x-ray spectroscopy*, Phys. Rev. Lett. **115**, 96404 (2015).

[109] S. Fatale, S. Moser, J. Miyawaki, Y. Harada, and M. Grioni, *Hybridization and electron-phonon coupling in ferroelectric* $BaTiO_3$ *probed by resonant inelastic x-ray scattering*, Phys. Rev. B **94**, 195131 (2016).

[110] A. Geondzhian, A. Sambri, G. M. De Luca, R. Di Capua, E. Di Gennaro, D. Betto, M. Rossi, Y. Y. Peng, R. Fumagalli, N. B. Brookes, L. Braicovich, K. Gilmore, G. Ghiringhelli, and M. Salluzzo, *Large polarons as key quasiparticles in* $SrTiO_3$ *and* $SrTiO_3$*-based heterostructures*, Phys. Rev. Lett. **125**, 126401 (2020).

[111] J. G. Vale, C. D. Dashwood, E. Paris, L. S. I. Veiga, M. Garcia-Fernandez, A. Nag, A. Walters, K. J. Zhou, I. M. Pietsch, A. Jesche, P. Gegenwart, R. Coldea, T. Schmitt, and D. F. Mcmorrow, *High-resolution resonant inelastic x-ray scattering study of the electron-phonon coupling in honeycomb* α*-*Li_2IrO_3, Phys. Rev. B **100**, 224303 (2019).

[112] D. Meyers, K. Nakatsukasa, S. Mu, L. Hao, J. Yang, Y. Cao, G. Fabbris, H. Miao, J. Pelliciari, D. McNally, M. Dantz, E. Paris, E. Karapetrova, Y. Choi, D. Haskel, P. Shafer, E. Arenholz, T. Schmitt, T. Berlijn, S. Johnston, J. Liu, and M. P. M. Dean, *Decoupling carrier concentration and electron-phonon coupling in oxide heterostructures observed with resonant inelastic x-ray scattering*, Phys. Rev. Lett. **121**, 236802 (2018).

[113] T. P. Devereaux, A. M. Shvaika, K. Wu, K. Wohlfeld, C. J. Jia, Y. Wang, B. Moritz, L. Chaix, W.-S. Lee, Z.-X. Shen, G. Ghiringhelli, and L. Braicovich, *Directly characterizing the relative strength and momentum dependence of electron-phonon coupling using resonant inelastic x-ray scattering*, Phys. Rev. X **6**, 41019 (2016).

[114] A. Geondzhian and K. Gilmore, *Demonstration of resonant inelastic x-ray scattering as a probe of exciton-phonon coupling*, Phys. Rev. B **98**, 214305 (2018).

[115] A. Geondzhian and K. Gilmore, *Generalization of the Franck-Condon model for phonon excitations by resonant inelastic x-ray scattering*, Phys. Rev. B **101**, 214307 (2020).

[116] K. Bieniasz, S. Johnston, and M. Berciu, *Beyond the single-site approximation modeling of electron-phonon coupling effects on resonant inelastic x-ray scattering spectra*, SciPost Phys. **11**, 62 (2021).

[117] M. Mohr, J. Maultzsch, E. Dobardžić, S. Reich, I. Milošević, M. Damnjanović, A. Bosak, M. Krisch, and C. Thomsen, *Phonon dispersion of graphite by inelastic x-ray scattering*, Phys. Rev. B **76**, 035439 (2007).

[118] X. Feng, S. Sallis, Y.-C. Shao, R. Qiao, Y.-S. Liu, L. C. Kao, A. S. Tremsin, Z. Hussain, W. Yang, J. Guo, and Y.-D. Chuang, *Disparate exciton-phonon couplings for zone-center and boundary phonons in solid-state graphite*, Phys. Rev. Lett. **125**, 116401 (2020).

[119] C. D. Dashwood, A. Geondzhian, J. G. Vale, A. C. Pakpour-Tabrizi, C. A. Howard, Q. Faure, L. S. I. Veiga, D. Meyers, S. G. Chiuzbăian, A. Nicolaou, N. Jaouen, R. B. Jackman, A. Nag, M. García-Fernández, K.-J. Zhou, A. C. Walters, K. Gilmore, D. F. McMorrow, and M. P. M. Dean, *Probing electron-phonon interactions away from the Fermi level with resonant inelastic x-ray scattering*, Phys. Rev. X **11**, 041052 (2021).

[120] M. Lazzeri, C. Attaccalite, L. Wirtz, and F. Mauri, *Impact of the electron-electron correlation on phonon dispersion: failure of LDA and GGA DFT functionals in graphene and graphite*, Phys. Rev. B **78**, 081406 (2008).

[121] M. X. Na, A. K. Mills, F. Boschini, M. Michiardi, B. Nosarzewski, R. P. Day, E. Razzoli, A. Sheyerman, M. Schneider, G. Levy, S. Zhdanovich, T. P. Devereaux, A. F. Kemper, D. J. Jones, and A. Damascelli, *Direct determination of mode-projected electron-phonon coupling in the time domain*, Science **366**, 1231 (2019).

[122] A. G. Marinopoulos, L. Reining, A. Rubio, and V. Olevano, *Ab initio study of the optical absorption and wave-vector-dependent dielectric response of graphite*, Phys. Rev. B **69**, 245419 (2004).

[123] P. A. Brühwiler, A. J. Maxwell, C. Puglia, A. Nilsson, S. Andersson, and N. Mårtensson, π^* *and* σ^* *excitons in C* 1*s absorption of graphite*, Phys. Rev. Lett. **74**, 614 (1995).

[124] F. Sette, G. K. Wertheim, Y. Ma, G. Meigs, S. Modesti, and C. T. Chen, *Lifetime and screening of the C* 1*s photoemission in graphite*, Phys. Rev. B **41**, 9766 (1990).

[125] D. C. Langreth, *Singularities in the x-ray spectra of metals*, Phys. Rev. B **1**, 471 (1970).

[126] H. J. Monkhorst and J. D. Pack, *Special points for Brillouin-zone integrations*, Phys. Rev. B **13**, 5188 (1976).

[127] W. Olovsson, T. Mizoguchi, M. Magnuson, S. Kontur, O. Hellman, I. Tanaka, and C. Draxl, *Vibrational effects in x-ray absorption spectra of two-dimensional layered materials*, J. Phys. Chem. C **123**, 9688 (2019).

[128] B. J. Kim, H. Jin, S. J. Moon, J.-Y. Kim, B.-G. Park, C. S. Leem, J. Yu, T. W. Noh, C. Kim, S.-J. Oh, J.-H. Park, V. Durairaj, G. Cao, and E. Rotenberg, *Novel $J_{eff} = 1/2$ Mott state induced by relativistic spin-orbit coupling in Sr_2IrO_4*, Phys. Rev. Lett. **101**, 076402 (2008).

[129] B. J. Kim, H. Ohsumi, T. Komesu, S. Sakai, T. Morita, H. Takagi, and T. Arima, *Phase-sensitive observation of a spin-orbital Mott state in Sr_2IrO_4*, Science **323**, 1329 (2009).

[130] M. K. Crawford, M. A. Subramanian, R. L. Harlow, J. A. Fernandez-Baca, Z. R. Wang, and D. C. Johnston, *Structural and magnetic studies of Sr_2IrO_4*, Phys. Rev. B **49**, 9198 (1994).

[131] F. Ye, S. Chi, B. C. Chakoumakos, J. A. Fernandez-Baca, T. Qi, and G. Cao, *Magnetic and crystal structures of Sr_2IrO_4: a neutron diffraction study*, Phys. Rev. B **87**, 140406(r) (2013).

[132] C. Dhital, T. Hogan, Z. Yamani, C. de la Cruz, X. Chen, S. Khadka, Z. Ren, and S. D. Wilson, *Neutron scattering study of correlated phase behavior in Sr_2IrO_4*, Phys. Rev. B **87**, 144405 (2013).

[133] D. H. Torchinsky, H. Chu, L. Zhao, N. B. Perkins, Y. Sizyuk, T. Qi, G. Cao, and D. Hsieh, *Structural distortion-induced magnetoelastic locking in Sr_2IrO_4 revealed through nonlinear optical harmonic generation*, Phys. Rev. Lett. **114**, 096404 (2015).

[134] S. Boseggia, R. Springell, H. C. Walker, H. M. Rønnow, C. Rüegg, H. Okabe, M. Isobe, R. S. Perry, S. P. Collins, and D. F. McMorrow, *Robustness of basal-plane antiferromagnetic order and the $J_{eff} = 1/2$ state*

in single-layer iridate spin-orbit Mott insulators, Phys. Rev. Lett. **110**, 117207 (2013).

[135] H. Liu and G. Khaliullin, *Pseudo Jahn-Teller effect and magnetoelastic coupling in spin-orbit Mott insulators*, Phys. Rev. Lett. **122**, 057203 (2019).

[136] J. Porras, J. Bertinshaw, H. Liu, G. Khaliullin, N. H. Sung, J.-W. Kim, S. Francoual, P. Steffens, G. Deng, M. Moretti Sala, A. Efimenko, A. Said, D. Casa, X. Huang, T. Gog, J. Kim, B. Keimer, and B. J. Kim, *Pseudospin-lattice coupling in the spin-orbit Mott insulator* Sr_2IrO_4, Phys. Rev. B **99**, 085125 (2019).

[137] H. Gretarsson, N. H. Sung, M. Höppner, B. J. Kim, B. Keimer, and M. Le Tacon, *Two-magnon Raman scattering and pseudospin-lattice interactions in* Sr_2IrO_4 *and* $Sr_3Ir_2O_7$, Phys. Rev. Lett. **116**, 136401 (2016).

[138] F. Wang and T. Senthil, *Twisted Hubbard model for* Sr_2IrO_4*: magnetism and possible high temperature superconductivity*, Phys. Rev. Lett. **106**, 136402 (2011).

[139] J. Kim, D. Casa, M. H. Upton, T. Gog, Y.-J. Kim, J. F. Mitchell, M. van Veenendaal, M. Daghofer, J. van den Brink, G. Khaliullin, and B. J. Kim, *Magnetic excitation spectra of* Sr_2IrO_4 *probed by resonant inelastic x-ray scattering: establishing links to cuprate superconductors*, Phys. Rev. Lett. **108**, 177003 (2012).

[140] R. Coldea, S. M. Hayden, G. Aeppli, T. G. Perring, C. D. Frost, T. E. Mason, S.-W. Cheong, and Z. Fisk, *Spin waves and electronic interactions in* La_2CuO_4, Phys. Rev. Lett. **86**, 5377 (2001).

[141] D. Pincini, J. G. Vale, C. Donnerer, A. de la Torre, E. C. Hunter, R. Perry, M. Moretti Sala, F. Baumberger, and D. F. McMorrow, *Anisotropic exchange and spin-wave damping in pure and electron-doped* Sr_2IrO_4, Phys. Rev. B **96**, 075162 (2017).

[142] Y. K. Kim, O. Krupin, J. D. Denlinger, A. Bostwick, E. Rotenberg, Q. Zhao, J. F. Mitchell, J. W. Allen, and B. J. Kim, *Fermi arcs in a doped pseudospin-1/2 Heisenberg antiferromagnet*, Science **345**, 187 (2014).

[143] Y. K. Kim, N. H. Sung, J. D. Denlinger, and B. J. Kim, *Observation of a d-wave gap in electron-doped Sr_2IrO_4*, Nat. Phys. **12**, 37 (2016).

[144] J. Zaanen and O. Gunnarsson, *Charged magnetic domain lines and the magnetism of high-T_c oxides*, Phys. Rev. B **40**, 7391 (1989).

[145] D. Poilblanc and T. M. Rice, *Charged solitons in the Hartree-Fock approximation to the large-U Hubbard model*, Phys. Rev. B **39**, 9749 (1989).

[146] R. Comin and A. Damascelli, *Resonant x-ray scattering studies of charge order in cuprates*, Annu. Rev. Condens. Matter Phys. **7**, 369 (2016).

[147] X. Chen, J. L. Schmehr, Z. Islam, Z. Porter, E. Zoghlin, K. Finkelstein, J. P. C. Ruff, and S. D. Wilson, *Unidirectional spin density wave state in metallic $(Sr_{1-x}La_x)_2IrO_4$*, Nat. Commun. **9**, 103 (2018).

[148] H. Chu, L. Zhao, A. de la Torre, T. Hogan, S. D. Wilson, and D. Hsieh, *A charge density wave-like instability in a doped spin-orbit-assisted weak Mott insulator*, Nat. Mater. **16**, 200 (2017).

[149] W. Jin, S. Li, J. Liu, Q. Han, Z. Porter, C. Peterson, J. Schmehr, I. Boulares, K. Sun, R. Merlin, S. D. Wilson, and L. Zhao, *Polarized Raman spectroscopy study of metallic $(Sr_{1-x}La_x)_3Ir_2O_7$: a consistent picture of disorder-interrupted unidirectional charge order*, Phys. Rev. B **99**, 041109(r) (2019).

[150] F. Weber, S. Rosenkranz, J.-P. Castellan, R. Osborn, R. Hott, R. Heid, K.-P. Bohnen, T. Egami, A. H. Said, and D. Reznik, *Extended phonon collapse and the origin of the charge-density wave in $2H$-$NbSe_2$*, Phys. Rev. Lett. **107**, 107403 (2011).

[151] D. Reznik, L. Pintschovius, M. Ito, S. Iikubo, M. Sato, H. Goka, M. Fujita, K. Yamada, G. D. Gu, and J. M. Tranquada, *Electron-phonon coupling reflecting dynamic charge inhomogeneity in copper oxide superconductors*, Nature **440**, 1170 (2006).

[152] H. Miao, D. Ishikawa, R. Heid, M. Le Tacon, G. Fabbris, D. Meyers, G. D. Gu, A. Q. R. Baron, and M. P. M. Dean, *Incommensurate phonon anomaly and the nature of charge density waves in cuprates*, Phys. Rev. X **8**, 011008 (2018).

[153] A. Q. R. Baron, *High-resolution inelastic x-ray scattering I & II*, in *Synchrotron light sources and free-electron lasers: accelerator physics, instrumentation and science applications*, edited by E. J. Jaeschke, S. Khan, J. R. Schneider, and J. B. Hastings, pp. 1643–1757. See also arXiv 1504.01098, Springer International Publishing, 2016.

[154] C. D. Dashwood, H. Miao, J. G. Vale, D. Ishikawa, D. A. Prishchenko, V. V. Mazurenko, V. G. Mazurenko, R. S. Perry, G. Cao, A. de la Torre, F. Baumberger, A. Q. R. Baron, D. F. McMorrow, and M. P. M. Dean, *Momentum-resolved lattice dynamics of parent and electron-doped* Sr_2IrO_4, Phys. Rev. B **100**, 085131 (2019).

[155] A. de la Torre, S. McKeown Walker, F. Y. Bruno, S. Riccó, Z. Wang, I. Gutierrez Lezama, G. Scheerer, G. Giriat, D. Jaccard, C. Berthod, T. K. Kim, M. Hoesch, E. C. Hunter, R. S. Perry, A. Tamai, and F. Baumberger, *Collapse of the Mott gap and emergence of a nodal liquid in lightly doped* Sr_2IrO_4, Phys. Rev. Lett. **115**, 176402 (2015).

[156] R. J. McQueeney, Y. Petrov, T. Egami, M. Yethiraj, G. Shirane, and Y. Endoh, *Anomalous dispersion of LO phonons in* $La_{1.85}Sr_{0.15}CuO_4$ *at low temperatures*, Phys. Rev. Lett. **82**, 628 (1999).

[157] H. Uchiyama, A. Q. R. Baron, S. Tsutsui, Y. Tanaka, W.-Z. Hu, A. Yamamoto, S. Tajima, and Y. Endoh, *Softening of Cu-O bond stretching phonons in tetragonal* $HgBa_2CuO_{4+\delta}$, Phys. Rev. Lett. **92**, 197005 (2004).

[158] D. Reznik, T. Fukuda, D. Lamago, A. Q. R. Baron, S. Tsutsui, M. Fujita, and K. Yamada, *q-dependence of the giant bond-stretching phonon anomaly in the stripe compound* $La_{1.48}Nd_{0.4}Sr_{0.12}CuO_4$ *measured by IXS*, J. Phys. Chem. Solids **69**, 3103 (2008).

[159] J. Graf, M. d'Astuto, C. Jozwiak, D. R. Garcia, N. L. Saini, M. Krisch, K. Ikeuchi, A. Q. R. Baron, H. Eisaki, and A. Lanzara, *Bond stretching phonon softening and kinks in the angle-resolved photoemission spectra of optimally doped* $Bi_2Sr_{1.6}La_{0.4}Cu_2O_{6+\delta}$ *superconductors*, Phys. Rev. Lett. **100**, 227002 (2008).

[160] P. E. Blöchl, *Projector augmented-wave method*, Phys. Rev. B **50**, 17953 (1994).

[161] G. Kresse and J. Furthmüller, *Efficient iterative schemes for ab initio total-energy calculations using a plane-wave basis set*, Phys. Rev. B **54**, 11169 (1996).

[162] J. P. Perdew and Y. Wang, *Accurate and simple analytic representation of the electron-gas correlation energy*, Phys. Rev. B **45**, 13244 (1992).

[163] A. Togo and I. Tanaka, *First principles phonon calculations in materials science*, Scr. Mater. **108**, 1 (2015).

[164] I. V. Solovyev, V. V. Mazurenko, and A. A. Katanin, *Validity and limitations of the superexchange model for the magnetic properties of* Sr_2IrO_4 *and* Ba_2IrO_4 *mediated by the strong spin-orbit coupling*, Phys. Rev. B **92**, 235109 (2015).

[165] L. Pintschovius, N. Pyka, W. Reichardt, A. Y. Rumiantsev, N. L. Mitrofanov, A. S. Ivanov, G. Collin, and P. Bourges, *Lattice dynamical studies of HTSC materials*, Phys. C Supercond. **185-189**, 156 (1991).

[166] M. d'Astuto, G. Dhalenne, J. Graf, M. Hoesch, P. Giura, M. Krisch, P. Berthet, A. Lanzara, and A. Shukla, *Sharp optical-phonon softening near optimal doping in $La_{2-x}Ba_xCuO_{4+\delta}$ observed via inelastic x-ray scattering*, Phys. Rev. B **78**, 140511(r) (2008).

[167] M. Le Tacon, A. Bosak, S. M. Souliou, G. Dellea, T. Loew, R. Heid, K.-P. Bohnen, G. Ghiringhelli, M. Krisch, and B. Keimer, *Inelastic x-ray scattering in $YBa_2Cu_3O_{6.6}$ reveals giant phonon anomalies and elastic central peak due to charge-density-wave formation*, Nat. Phys. **10**, 52 (2014).

[168] X. Lu, P. Olalde-Velasco, Y. Huang, V. Bisogni, J. Pelliciari, S. Fatale, M. Dantz, J. G. Vale, E. C. Hunter, J. Chang, V. N. Strocov, R. S. Perry, M. Grioni, D. F. McMorrow, H. M. Rønnow, and T. Schmitt, *Dispersive magnetic and electronic excitations in iridate perovskites probed by oxygen K-edge resonant inelastic x-ray scattering*, Phys. Rev. B **97**, 041102 (2018).

[169] R. Fumagalli, L. Braicovich, M. Minola, Y. Y. Peng, K. Kummer, D. Betto, M. Rossi, E. Lefrançois, C. Morawe, M. Salluzzo, H. Suzuki, F. Yakhou, M. Le Tacon, B. Keimer, N. B. Brookes, M. M. Sala, and G. Ghiringhelli, *Polarization-resolved Cu L_3-edge resonant inelastic x-ray scattering of orbital and spin excitations in $NdBa_2Cu_3O_{7-\delta}$*, Phys. Rev. B **99**, 134517 (2019).

[170] E. Paris, Y. Tseng, E. M. Pärschke, W. Zhang, M. H. Upton, A. Efimenko, K. Rolfs, D. E. McNally, L. Maurel, M. Naamneh, M. Caputo, V. N. Strocov, Z. Wang, D. Casa, C. W. Schneider, E. Pomjakushina, K. Wohlfeld, M. Radovic, and T. Schmitt, *Strain engineering of the*

charge and spin-orbital interactions in Sr_2IrO_4, Proc. Natl. Acad. Sci. U.S.A. **117**, 24764 (2020).

[171] S. Johnston, F. Vernay, B. Moritz, Z.-X. Shen, N. Nagaosa, J. Zaanen, and T. P. Devereaux, *Systematic study of electron-phonon coupling to oxygen modes across the cuprates*, Phys. Rev. B **82**, 064513 (2010).

[172] R. B. von Dreele, J. D. Jorgensen, and C. G. Windsor, *Rietveld refinement with spallation neutron powder diffraction data*, J. Appl. Crystallogr. **15**, 581 (1982).

[173] J. Lamsal and W. Montfrooij, *Extracting paramagnon excitations from resonant inelastic x-ray scattering experiments*, Phys. Rev. B **93**, 214513 (2016).

[174] M. W. Haverkort, *Theory of resonant inelastic x-ray scattering by collective magnetic excitations*, Phys. Rev. Lett. **105**, 167404 (2010).

[175] J. G. Vale, S. Calder, C. Donnerer, D. Pincini, Y. G. Shi, Y. Tsujimoto, K. Yamaura, M. Moretti Sala, J. van den Brink, A. D. Christianson, and D. F. McMorrow, *Crossover from itinerant to localized magnetic excitations through the metal-insulator transition in $NaOsO_3$*, Phys. Rev. B **97**, 184429 (2018).

[176] J. G. Vale, S. Boseggia, H. C. Walker, R. Springell, Z. Feng, E. C. Hunter, R. S. Perry, D. Prabhakaran, A. T. Boothroyd, S. P. Collins, H. M. Rønnow, and D. F. McMorrow, *Importance of XY anisotropy in Sr_2IrO_4 revealed by magnetic critical scattering experiments*, Phys. Rev. B **92**, 020406 (2015).

[177] J. Bertinshaw, J. K. Kim, J. Porras, K. Ueda, N. H. Sung, A. Efimenko, A. Bombardi, J. Kim, B. Keimer, and B. J. Kim, *Spin-wave gap collapse in Rh-doped Sr_2IrO_4*, Phys. Rev. B **101**, 094428 (2020).

[178] G. Zhang and E. Pavarini, *Magnetic superexchange couplings in Sr_2IrO_4*, Phys. Rev. B **104**, 125116 (2021).

[179] S. Mohapatra and A. Singh, *Coupled spin-orbital fluctuations in a three orbital model for $4d$ and $5d$ oxides with electron fillings $n = 3, 4, 5$— application to $NaOsO_3$, Ca_2RuO_4 and Sr_2IrO_4*, J. Phys. Condens. Matter **33**, 345803 (2021).

[180] R. Xu and T. Chiang, *Determination of phonon dispersion relations by x-ray thermal diffuse scattering*, Z. Kristallogr. **220**, 1009 (2005).